University of Tennessee, Knoxville
TRACE: Tennessee Research and Creative Exchange

Doctoral Dissertations | Graduate School

5-2012

Liquid Jet Experiments and Simulations for a Verification and Validation Study

Lee Paul Tschaepe
ltschaep@utk.edu

Follow this and additional works at: https://trace.tennessee.edu/utk_graddiss

 Part of the Nuclear Engineering Commons

Recommended Citation

Tschaepe, Lee Paul, "Liquid Jet Experiments and Simulations for a Verification and Validation Study. " PhD diss., University of Tennessee, 2012.
https://trace.tennessee.edu/utk_graddiss/1360

This Dissertation is brought to you for free and open access by the Graduate School at TRACE: Tennessee Research and Creative Exchange. It has been accepted for inclusion in Doctoral Dissertations by an authorized administrator of TRACE: Tennessee Research and Creative Exchange. For more information, please contact trace@utk.edu.

To the Graduate Council:

I am submitting herewith a dissertation written by Lee Paul Tschaepe entitled "Liquid Jet Experiments and Simulations for a Verification and Validation Study." I have examined the final electronic copy of this dissertation for form and content and recommend that it be accepted in partial fulfillment of the requirements for the degree of Doctor of Philosophy, with a major in Nuclear Engineering.

Arthur E. Ruggles, Major Professor

We have read this dissertation and recommend its acceptance:

Lawrence H. Heilbronn, Belle R. Upadhyaya, Robert W. McAmis, Basil N. Antar

Accepted for the Council:

Carolyn R. Hodges

Vice Provost and Dean of the Graduate School

(Original signatures are on file with official student records.)

Liquid Jet Experiments and Simulations for a Verification and Validation Study

A Dissertation Presented for the
Doctorate of Philosophy
Degree
The University of Tennessee, Knoxville

Lee Paul Tschaepe
May 2012

Copyright © 2011 by Lee P. Tschaepe
All rights reserved.

ACKNOWLEDGEMENTS

I would like to acknowledge my deepest gratitude to my advisor, Dr. Arthur E. Ruggles, for his patience and guidance through the course of my academic development. Despite his willingness to entertain far-fetched ideas, he still provided a path forward which ultimately led to the completion of this dissertation. I would like to acknowledge the funder for this research, a grant from the Nuclear Engineering University Program (NEUP) under DOE. I would also like to thank my family for their constant support and encouragement in my educational pursuits. Without their encouragement I would not be where I am today.

ABSTRACT

The velocity field for two vertical parallel water jets impinging into a large stationary volume of water is mapped using ultrasonic interrogation. Thermal mapping of the vertical parallel water jets at high Reynolds numbers has been performed. The velocity data and associated statistics are related to the measurement volume and the ultrasonic Doppler measurement technique. The data are also compared to the literature for twin jets. The interaction of parallel jets is of interest to liquid metal reactor design. Liquid metal fast reactor (LMFR) coolant enters the bottom of the fuel bundles and exits through the top of the bundles. The power levels are not uniform in the bundles, leading to variation in bundle exit flow temperatures. The flow from the fuel bundles must mix thoroughly in the upper plenum of the reactor, prior to exiting through the hot leg of the reactor. Otherwise temperature variations in the hot leg flow can lead to unacceptable thermal stresses. The thermal-fluid phenomena controlling the mixing from twin jets examined here are similar to those controlling mixing of exit flows from the fuel bundles. Consequently, data from the parallel jet geometry are useful to validate Computational Fluid Dynamic (CFD) codes used for liquid metal reactor design. The water tests provide the opportunity to refine experimental technique, and to qualify the ultrasound instrument prior to deployment in liquid metal experiments. The framework for the validation of proposed LMFR CFD simulations is developed. A literature review of jet theory and the state of CFD verification and validation is performed. Following the literature review, CFD scoping studies are performed to aid the placement of instrumentation, data acquisition planning, and the design of the water test facility. The water test facility was then constructed and ultrasonic velocity measurements were performed to characterize the jet time averaged velocity field and local velocity variation statistics. Mathematical transformation between ultrasonic velocity measurements and CFD predictions are established. The ultrasonic velocity data from this project will be corroborated with optical particle tracking data later in the project. This work is funded by a research grant from the NEUP under DOE.

TABLE OF CONTENTS

LIST OF TABLES

LIST OF FIGURES

LIST OF ACRONYMS

AIAA	American Institute of Aeronautics and Astronautics
ANL	Argonne National Laboratory
ASME	American Society of Mechanical Engineers
ASTM	American Society of Testing and Materials
CFD	Computational Fluid Dynamics
CSAU	Code Scaling Applicability Uncertainty
DNS	Direct Numerical Simulation
DOE	Department of Energy
FDS	Fire Dynamics Simulation
ISO GUM	International Standardization Guide to the Expression of Uncertainty in Measurement
LES	Large Eddy Simulations
LMFR	Liquid Metal Fast Reactor
MMS	Method of Manufacture Solutions
NEA	Nuclear Energy Agency
NEUP	Nuclear Energy University Programs
NIST	National Institute of Standards and Technology
NRC	Nuclear Regulatory Commission
PIRT	Phenomenon Identification and Ranking Table
QA	Quality Assurance
RANS	Reynolds Average Navier Stokes
RE	Richardson Extrapolation
SFPE	Society of Fire Protection Engineers
SFR	Sodium Fast Reactor
TN	Tennessee
UI	University of Idaho
UTK	University of Tennessee at Knoxville
UVP	Ultrasonic Velocity Probe
V&V	Verification and Validation
WTF	Water Test Facility

LIST OF ATTACHMENTS

NEUP_TwinJet_Thermal_Data.zip

CHAPTER I

INTRODUCTION AND GENERAL INFORMATION

1.0 Summary of NEUP (Umbrella) Project

This research is supported by a Nuclear Energy University Programs (NEUP) grant, “Data Collection Methods for Validation of Advanced Multi-Resolution Fast Reactor Simulations.” The goals of this project include: The establishment of validation, verification, and benchmarking requirements needed for the advancement of increasingly complex simulation codes; the acquisition of detailed time correlated fluid dynamic and heat transfer data needed for the validation of liquid metal fast reactor (LMFR) system simulations; and the development of methods to aid in the reduction and characterization of the generated data sets. The project team includes the University of Idaho (UI), the University of Tennessee in Knoxville (UTK), and Argonne National Laboratory (ANL). The thermal fluid situation analyzed is the turbulent mixing of two parallel, side-by-side, liquid metal jets impinging vertically into a pool of identical liquid metal. The UI and UTK are tasked with the construction of two separate effects test facilities for the study of the dual jet system. A mercury twin jet facility is planned at UTK, and a sodium twin jet facility is planned for tests at UI. Sodium is a coolant that has historically been employed in LMFR systems. Reynolds Average Navier Stokes (RANS), Large Eddy Simulation (LES), and Direct

Numerical Simulation (DNS) Computational Fluid Dynamic (CFD) approaches to predict the measured data are to be undertaken at ANL.

A water test facility (WTF) was constructed at UTK to qualify the ultrasonic flow velocity instrumentation to be used in the opaque liquid metal twin jet experiments, and to refine data acquisition techniques. This dissertation is based on the water experiment. The data acquired through the water test facility (WTF) dovetails with the overarching goal of the NEUP project, validation of multiphysics simulation codes. The WTF is designed to operate at a jet Reynolds number equal to 18000, a value set in the NEUP proposal as similar to that present in sodium reactor plenum jet flows. Lessons learned from the WTF are being carried into the construction of the liquid metal twin jet facilities.

The multiphysics code COMSOL version 3.4 is employed to perform scoping CFD simulations of twin jet mixing in water and in liquid metals. The jet velocity topology, especially velocity gradients in the outer shear layer, and in the mixing region between the jets, was characterized in the COMSOL simulations. This helped to establish the scale of the WTF required for data acquisition with the ultrasonic method, which has a relatively large measurement volume and several other measurement limitations presented later. The WTF design was also informed by the review of single jet, twin jet and triple jet literature.

The ultrasonic velocity probe is one of a few velocity measurement modalities available for opaque fluids. The WTF allows this instrument to be

qualified in a transparent fluid where corroborative data acquisition methods are available, prior to its use in the opaque fluids mercury and sodium. This qualification effort exposed velocity measurement sensitivity to Graphical User Interface (GUI) settings.

UVP measurement attributes are related to flow fundamentals through the multi-phase Reynolds Transport Theorem to help bridge the measurement to the CFD prediction. It is the objective of others to perform the complete validation of the CFD. The data is archived in conjunction with this dissertation for CFD validation and it is publicly available.

In the course of this research the current state of CFD Verification and Validation (V&V) was reviewed. The outcomes of that review are presented herein for context to overarching CFD V&V activities across several disciplines. The data presented herein have quantified uncertainties following the recommendations of the ASME PTC 19.1 approach to experimental error and uncertainty quantification standard, which is recommended by the ASME CFD V&V 20 standard for validation data.

1.2 Dissertation Structure

The dissertation begins with a review of turbulence, and then progresses to turbulence modeling for jets. This is followed by review of Verification and Validation (V&V) methodologies available for CFD. Prior single jet, twin jet and triple jet experiments are reviewed to conclude the review chapter.

The water test facility is described in chapter 3, followed by an overview of the ultrasonic Doppler profiler used to collect velocity data in chapter 4. Some CFD simulations of the twin jet in water and in liquid metals are presented in Chapter 5. Those simulations were used to guide the data acquisition strategy, and to aid in the WTF design. They are presented after the facility description and instrument description to bridge between the measurements and the data, in part because the CFD predictions are field predictions, and the velocity data are field data. Both are presented in multi-color contour plots.

Chapter 6 presents the single jet data, and chapter 7 presents the twin jet data. Chapter 8 offers conclusions and future work.

1.3 Dissertation Contributions

- Performed review of existing CFD V&V approaches employed in engineering, with some emphasis on data requirements for validations (unique), with collaborators (S. Peters et al. 2011).
- Performed scoping single jet and twin jet simulations with the multiphysics code COMSOL to support experiment design, with collaborators (L. Tschaepe et al 2010).
- Created a facility capable of measuring velocity and temperature field data for multiple twin jet mixing geometries at X/D > 100. Where X is the vertical distance above the jet inlet and D is the diameter of the jet. (unique)

- Mapped a single jet velocity field using ultrasonic velocimetry.
- Mapped a dual jet velocity field using ultrasonic velocimetry.
- Related velocity measurements and the associated statistics of the ultrasound instrument to experimental volumes relevant to CFD validation. (unique)
- Data collection performed consistent with guidelines to V&V process as defined early in the NEUP project (unique).

CHAPTER 2

LITERATURE REVIEW

2.0 Turbulence Theory

Turbulence is a term used to describe fluid flows that are chaotic. The degree of turbulence in a flow is characterized to first order by the non-dimensional Reynolds number. The Reynolds number relates inertial forces to viscous forces. Generally, the higher a flow's Reynolds number the more chaotic the flow structure. Numerous investigations have attempted to describe the chaotic nature of flows. One of the most well received theories, developed by Russian mathematician Andrey Kolmogorov in 1941, described the chaotic fluctuations statistically. This theory assumes that the turbulent flow is defined by an energy spectrum E(k).

$$kinetic\ energy = \int_0^\infty E(k)dk \qquad (1)$$

where the wave number $k = 2\pi/l$ and *l* is the defined length scale. The integral of the energy spectrum over all wave numbers is found to be $(1/2)\langle v^2 \rangle$, the flow mass specific kinetic energy. The flow energy is found to impart energy to eddies of scale *l* at a rate ϵ. These eddies will continuously transfer the energy imparted to them to smaller eddies. This process will continue until the smallest eddies dissipate the energy through viscous frictions at molecular scale converting the flow energy to heat.

The length scale for a particular eddy generation and subsequent generations is $l_n = l_0 2^n$. The nth wave number is then $k_n = l_n^{-1}$. The velocity difference across a length scale is related to the energy spectrum, corresponding to the nth length scale.

$$v_n \cong E_n^{1/2} \tag{2}$$

The flow time scale (eddy turnover time) is defined as $t_n = l_n / v_n$. The energy transfer rate must be equivalent to the available kinetic energy to be transferred between subsequent generations.

$$\epsilon \equiv \frac{v_n^3}{l_n} \tag{3}$$

Substituting prior results and assumptions gives (Kraichnan 1967),

$$E(k) \cong \epsilon^{2/3} k^{-5/3} \tag{4}$$

This implies that the energy cascades from large eddies to smaller eddies until the energy is converted to heat by the smallest eddies via viscous effects. There is extensive experimental and numerical evidence to support this theory. However, a consequence of this formulation in two dimensional flows is that as the Reynolds number approaches infinity, the mean square vorticity is infinite. This is not possible for two dimensional flows. The energy dissipation in subsequent eddy generations must tend to zero in order to satisfy conservation of vorticity. Kraichnan was successfully able to generalize the Kolmogorov 1941

theory for two dimensions (Kraichnan 1967). Kraichnan determined that there are two cascades that occur: One cascade is due to the smaller eddies imparting energy to the larger eddies and the second cascade is the mean square vorticity (enstrophy). The energy cascade still follows the $k^{-5/3}$ law but in reverse (small to large). The enstrophy cascade follows a k^{-3} law.

The Kolmogorov Theory of 1941 predicts the inertial range scaling laws of high order moments. These predictions do not mesh well with measurements of moments of the fourth order and higher. The discrepancies are due to intermittency effects. At moderate to low Reynolds numbers the fluctuations of the sample will display a Gaussian distribution. The time derivative of the time dependency of the velocity fluctuations for a high Reynolds number flow does not provide a Gaussian distribution. In fact there will be intermittent burst that are separated by periods of relative quiet. This indicates that more energy is transferred to the next generation eddy than is predicted by the original Kolmogorov 1941 theory. To account for this Mandelbrot determined that the $k^{-5/3}$ formulation must be modified (Mandelbrot 1976).

$$E(k) \cong \epsilon^{2/3} k^{-5/3} (k l_0)^{-(3-D)/3} \quad (5)$$

where D is the self-similarity dimension. It is related to the number of daughter eddies needed to make up the parent.

2.1 Jet Turbulence Theory

A brief background of jet theory is provided with emphasis given to submerged jets. Figure 1 is a diagram of a simple submerged jet. The jet surface defines where the jet flow interacts with the pool. Eddies are formed in the shearing region of the jet boundary and these eddies lead to mass entrainment in the jet. The mass entrainment subsequently results in the transfer of momentum and energy across the boundary. Along the boundary, a region of finite thickness develops where there is a continuous distribution of velocity temperature and species concentration. This is the turbulent jet shear layer.

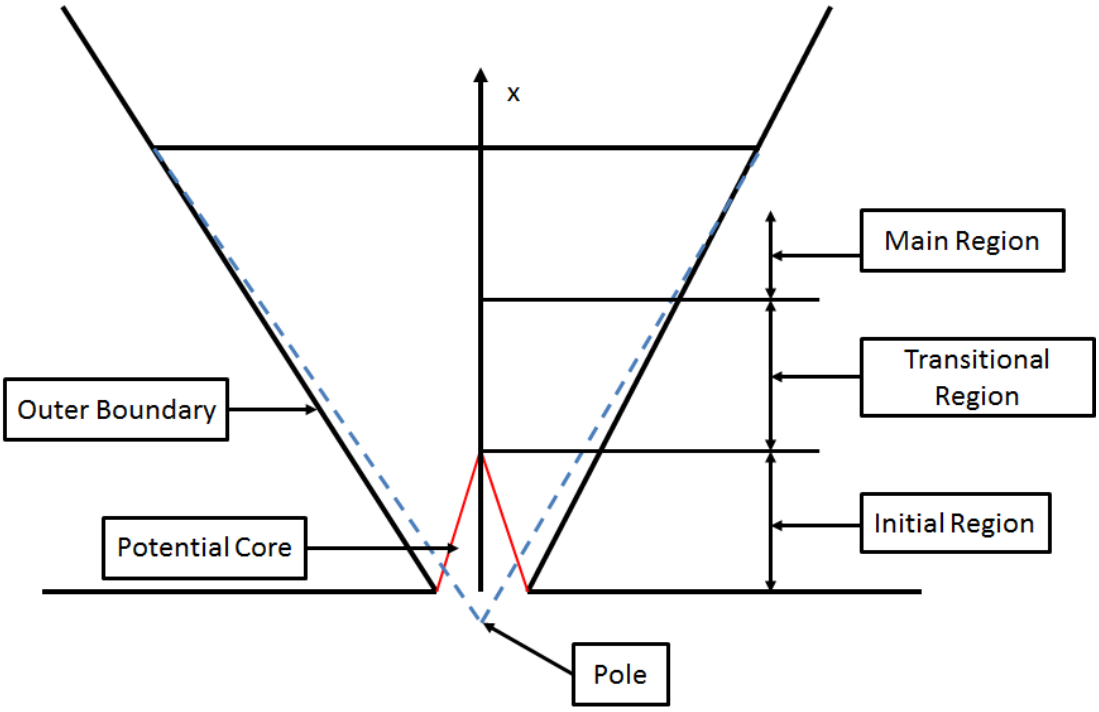

Figure 1. Jet Diagram

A submerged jet is a turbulent jet that spreads through a medium at rest. In figure 1, the outer boundary is defined at the point where the velocity with respect to the y-axis is zero. The inner boundary is defined by the potential core, where the velocity equals the discharge velocity. At the jet discharge the shear layer is of zero thickness. It will continue to grow as the jet slows and the surrounding fluid is entrained. The static pressure remains constant at each flow cross-section and relative to the external fluid. This results in a constant momentum condition at each jet cross section along the x axis, absent thermal dissipation in the energy balance.

$$J = \rho \int_{-\infty}^{\infty} u^2 dy = constant \tag{6}$$

The entrainment and constant momentum condition lead to the broadening of the jet velocity profile and reduction in the velocity magnitude with increasing distance from the origin. Trüpel's experiments on jet broadening depict these phenomena (Trüpel 1915).

As a result of the constant momentum constraint, the variation of the velocity with respect to the pole of the jet can be determined via a momentum balance. The centerline velocity of an axially-symmetric submerged jet is

$$u_m = \frac{const}{x} \tag{7}$$

The centerline velocity of a parallel plane (i.e. two dimensional) submerged jet is

$$u_m = \frac{const}{\sqrt{x}} \quad (8)$$

where *x* is the distance from the pole. Determination of the velocity profile at a cross section allows for the prediction of the velocity profile at any other cross-section. The velocity fields are universal leading to similar solutions due to the common assumptions for the momentum balance for all x positions of the jet. The temperature profile for a hot jet entering a cooler pool is similar to the velocity profile.

In fully developed turbulent flow, quantities measured are typically not constant values but a sum of the mean value plus a fluctuation about that mean. A mean value may be defined as,

$$\bar{Q} = \frac{1}{T}\int_{t_0}^{t_0+T} Q dt \quad (9)$$

This allows the fluctuation to be defined by,

$$Q' = Q - \bar{Q} \quad (10)$$

where Q is the total quantity (Tennekes and Lumley 1972).

When averaged over a period of time the fluctuations are equal to zero. The general form of the continuity and Navier-Stokes normally do not explicitly follow these temporal fluctuations. Direct Numerical Simulations (DNS) evoke turbulence directly from Navier-Stokes, but these techniques are outside the

discussion here. However, Navier-Stokes equations can be rewritten to include the time averaged influence of the fluctuations:

$$\frac{\partial \bar{u}}{\partial x} + \frac{\partial \bar{v}}{\partial y} + \frac{\partial \bar{w}}{\partial z} = 0 \tag{11}$$

$$\rho \frac{D\bar{V}}{Dt} + \rho \frac{\partial (\overline{u_i' u_j'})}{\partial x_j} = \rho g - \nabla \bar{p} + \mu \nabla^2 \bar{V} \tag{12}$$

The $\overline{u_i' u_j'}$ term in the mean momentum equation is the turbulent inertia tensor, sometimes referred to as the Reynolds stress tensor. The inclusion of the temporal fluctuations in the continuity equation does not significantly increase the complexity of the equation. However, the inclusion of these fluctuations in the momentum equations adds an additional nine terms to the turbulent inertia tensor. Turbulence mines both momentum and energy from mean flow values. With the addition of turbulent components u', v', and w' equation 6 must be revisited. Equation 6 is approximate because: Kinetic energy transitions to thermal energy, following Kolmogorov's model, and the initial jet at the inlet may have momentum dominated by $\rho \bar{u} A_{xs_{inlet}} \bar{u}$. However, as u', v', and w' are grown in the jet shear layer, the mean momentum integral in y must decline along x. The jets investigated are fully developed and have turbulence upon entry into the tank, but at length scales at entry are small relative to those initiated in the free shear layer of the jet. The inlet u', v', and w' carried forward from the inlet conduit flow likely dissipate while the new turbulence fluctuations at the jet boundary are initiated.

2.2 Free Turbulence Theories

In Prandtl's first theory on free turbulence, it is assumed that the fluctuating components of velocity in the transverse direction are proportional to the longitudinal direction (Prandtl 1925). Further, it is assumed that as an arbitrary volume of fluid translates from position $x\ to\ x \pm y$ the volume maintains its original velocity and momentum until it reaches its new destination. Upon arriving at this new location the particle must accommodate the new longitudinal velocity, specific to that layer of fluid. In Prandtl's development the length (the distance moved) is related to the turbulent fluctuation,

$$u' \approx l \left|\frac{\partial u}{\partial y}\right| \tag{13}$$

l is referred to as the mixing length. This equation leads to Prandtl's formula for turbulent shearing stress. This part of the development is identical to Prandtl's theory for turbulence in boundary layers adjacent to fixed walls.

$$\tau_{xy} = \pm\rho l^2 \frac{\partial u}{\partial y}\left|\frac{\partial u}{\partial y}\right| \tag{14}$$

In unbounded, free turbulent flows the mixing length is constant in the transverse direction of flow and varies by a constant in the direction of flow. The variation in the direction of flow is with respect to jet width. In a submerged jet the width varies with respect to the distance from the pole.

$$l = cx \tag{15}$$

where x is the coordinate in the direction of flow. This leads to Prandtl's two-dimensional equation of motion.

$$u\frac{\partial u}{\partial x} + v\frac{\partial u}{\partial y} = \pm 2c^2x^2\frac{\partial u}{\partial y}\frac{\partial^2 u}{\partial y^2} \quad (16)$$

Using Prandtl's theories, Tollmien developed similarity solutions for plane and axis-symmetric submerged jets (Abramovich 1963). The turbulence has been parameterized into the time averaged shear stress in equation 14, so these models apply only to the time averaged velocities. The development of the plane turbulent jet is provided. It was stated in equation 8 that the velocity of a plane jet varies inversely with respect to the square root of the distance from the pole. The velocity at any point in the jet is

$$u = \frac{n}{\sqrt{x}}f(\eta) \quad (17)$$

where $\eta = y/x$. With the introduction of the stream function concept, the longitudinal and transverse velocity components are recast

$$u = \frac{\partial \psi}{\partial y} \quad (18)$$

$$v = -\frac{\partial \psi}{\partial x} \quad (19)$$

Therefore the stream function is defined

$$\psi = n\sqrt{x}\int f(\eta)d\eta \quad (20)$$

$$F(\eta) = \int f(\eta) d\eta \quad (21)$$

The velocity components and stream function are rewritten.

$$\psi = n\sqrt{x}F(\eta) \quad (22)$$

$$u = \frac{n}{\sqrt{x}}F'(\eta) \quad (23)$$

$$v = \frac{n}{\sqrt{x}}\left[\eta F'(\eta) - \frac{1}{2}F(\eta)\right] \quad (24)$$

The momentum balance for an isolated control surface, at fixed x, is given by the following equation:

$$uv + \frac{\partial}{\partial x}\int_{\infty}^{y} u^2 dy + c^2x^2\left(\frac{\partial u}{\partial y}\right)^2 = 0 \quad (25)$$

Replacing u and v using in equations 23 and 24 yields

$$2c^2[F''(\eta)]^2 = F(\eta)F^2(\eta) \quad (26)$$

A change of coordinates is made, to exclude the influence of the jet structure on $F(\eta)$.

$$\varphi = \frac{\eta}{a} \quad (27)$$

where $a = \sqrt[3]{2c^2}$. Equation 27 is now rewritten

$$[F''(\varphi)]^2 = F(\varphi)F'(\varphi) \quad (28)$$

Likewise, the velocity components are rewritten.

$$u = u_m F'(\varphi) \tag{29}$$

$$v = \frac{an}{\sqrt{x}}\left[\varphi F'(\varphi) - \frac{1}{2}F(\varphi)\right] \tag{30}$$

Tollmien performed one additional transformation and was able to derive a solution velocity profile for the downstream part of the jet. The solution is validated by Förthmann's experiments shown in figure 2 (Förthmann 1934).

G. Taylor proposed a competing theory of free turbulence (Taylor 1932). Taylor's model, unlike Prandtl's, begins with the assumption that the turbulent shearing stresses are caused by vorticity transfer. Prandtl's original theory proposed that the shearing stresses are due to momentum transfer.

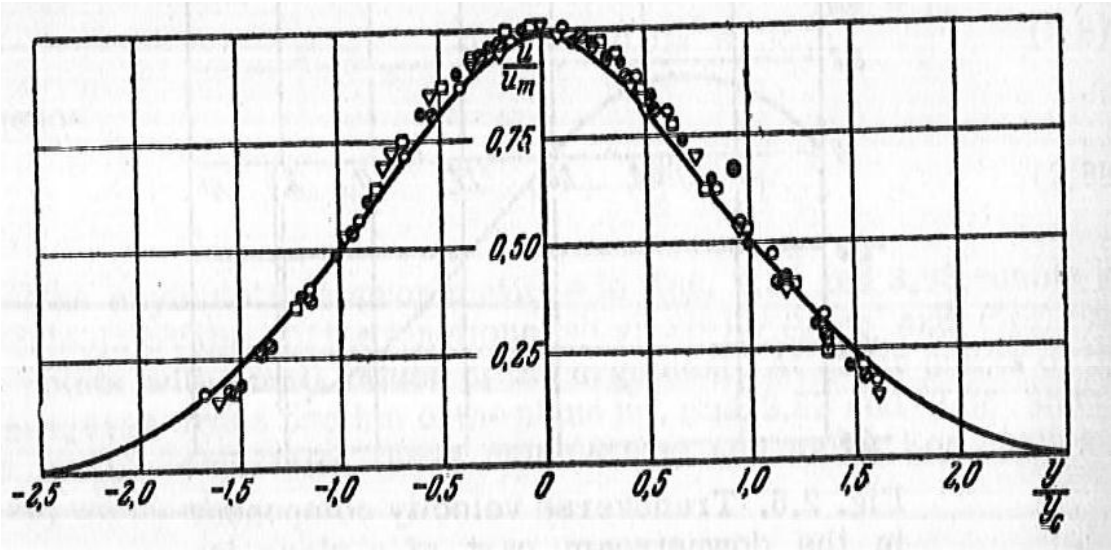

Figure 2. Forthmann's experimental measurements of downstream jet velocities plotted against Tollmien's theoretical curve. (Abramovich 1963)

Assuming the two dimensional flow depicted in figure 2, the mean vorticity is defined

$$\bar{\omega} = \frac{1}{2}\left(\frac{\partial \bar{u}}{\partial y} - \frac{\partial \bar{v}}{\partial x}\right) \tag{31}$$

where $\partial \bar{v}/\partial x$ is assumed small compared with $\partial \bar{u}/\partial y$ and is neglected. Fluid particles in a flow will have an average path length, l_T. Taylor's mixing length, l_T, is not equal to Prandtl's mixing length, l. fluid particles moving in the transverse direction have either an excess or deficiency of vorticity based on the fluid layer they departed from and the fluid layer which they arrive.

$$\Delta\bar{\omega} = l_T \frac{\partial \bar{\omega}}{\partial y} = \frac{1}{2} l_T \frac{\partial^2 u}{\partial y^2} \tag{32}$$

Assuming a stepwise change in vorticity equal to $\omega' = \Delta\bar{\omega}$

$$\omega' = \frac{1}{2}\frac{\partial u'}{\partial y} \tag{33}$$

thus

$$\frac{\partial u'}{\partial y} = l_T \frac{\partial^2 \bar{u}}{\partial y^2} \tag{34}$$

The momentum equation is recast.

$$\bar{u}\frac{\partial \bar{u}}{\partial x} + \bar{v}\frac{\partial \bar{u}}{\partial y} + \overline{v' l_T}\frac{\partial^2 \bar{u}}{\partial y^2} = 0 \tag{35}$$

Following the approach used in Prandtl's original theory, it is assumed that the velocity fluctuations in the transverse and longitudinal directions are of equivalent order.

$$\pm v' \sim u' \sim l_T \frac{\partial u}{\partial y} \tag{36}$$

Taylor's two dimensional equation of motion is

$$u\frac{\partial u}{\partial x} + v\frac{\partial u}{\partial y} = \pm 2 l_T^2 \frac{\partial u}{\partial y}\frac{\partial^2 u}{\partial y^2} \tag{37}$$

This differs from Prandtl's theory by

$$l_T = l\sqrt{2} \tag{38}$$

The equation for shearing stress via Taylor's theory

$$\tau_{xy} = \pm \frac{1}{2}\rho l_T^2 \left(\frac{\partial u}{\partial y}\right)^2 \tag{39}$$

and for Prandtl's theory

$$\tau_{xy} = \pm \frac{1}{2}\rho c^2 x^2 \left(\frac{\partial u}{\partial y}\right)^2 \tag{40}$$

Beyond the differences in justification for the two theories, they result in the same expression for the shearing stress. Taylor's development of the shearing stress differs from Prandtl's by a constant. Taylor's theory does not yield a significant difference in prediction of jet velocity profiles.

Later, Prandtl offered a new theory on free turbulence (Prandtl 1942). The approach differs from the old theory in that it is the coefficient of turbulent viscosity and not the mixing length that is constant over a specific jet cross section. It is the phenomena of flow similarity that causes the mixing length at similar points to be identical. The new theory states that the kinematic viscosity varies proportionally to the product of the mixing zone thickness and velocity difference at the boundaries of the mixing zone. Based on Prandtl's new theory, the kinematic viscosity for a submerged jet is

$$\epsilon = xbu_m \tag{41}$$

where ϵ is the kinematic viscosity. The shearing stress based on this new theory is

$$\tau_{xy} = \rho xb(u_m - u_H)\frac{du}{dy} \tag{42}$$

Görtler uses equation 42 to develop an analytic expression describing the velocity profile for the two-dimensional mixing region at the boundary between parallel jets with different velocities (Görtler 1942). The equation of motion used resembles the boundary layer equation,

$$u\frac{\partial u}{\partial x} + v\frac{\partial u}{\partial y} = \epsilon\frac{\partial^2 u}{\partial y^2} \tag{43}$$

And the following transformations lead to the equation Görtler solved,

$$\xi = \sigma \frac{y}{x} \tag{44}$$

$$\frac{u}{U} = \sigma F'(\xi) \tag{45}$$

$$U = \frac{1}{2}(u_m + u_H) \tag{46}$$

$$b = kx \tag{47}$$

$$\psi = \int u \, dy = xUF(\xi) \tag{48}$$

$$\frac{v}{U} = -\frac{\partial \psi}{\partial x} = \xi F' - F \tag{49}$$

With some manipulation of equations 42-49, the similarity solution is produced.

$$F''' + 2\sigma F F' = 0 \tag{50}$$

Görtler's theory predicts a velocity profile that is shifted away from experimental data that was obtained by Reichardt (Reichardt 1951). If the theoretical curve is shifted, Görtler's solution of Prandtl's theory is found to agree well with the experimental data. A graph of Görtler's un-shifted curve and shifted curve versus Reichardt's data at the edge of a plane jet is provided in figure 3. The theoretical velocity profile agreement improves with increased distance from the nozzle.

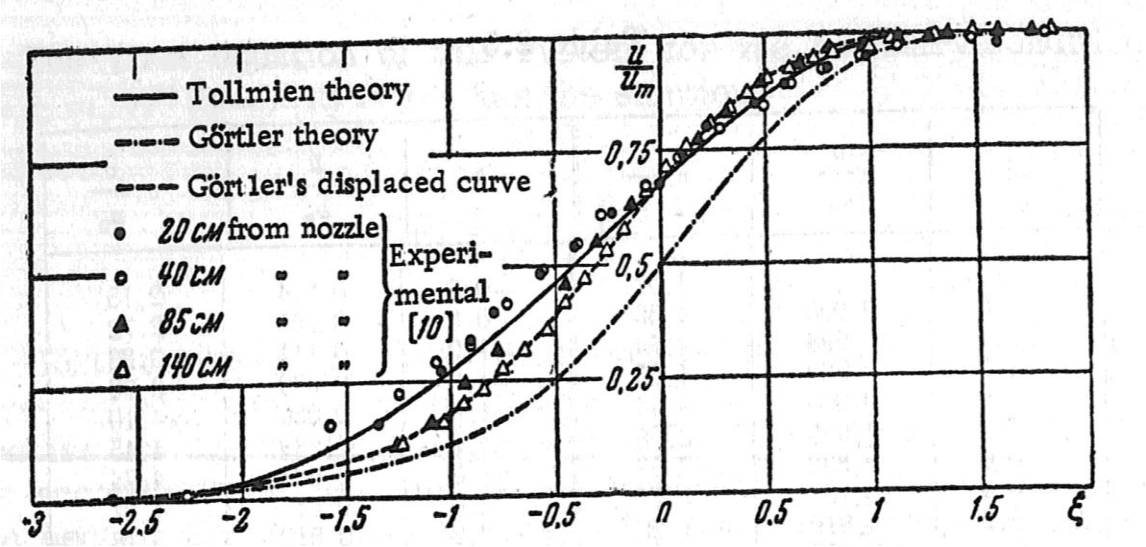

Figure 3. Görtler's theory and Reichardt's data. (Abramovich 1963)

2.3 Verification and Validation of Computational Fluid Dynamics

The focus of the NEUP project funding this research is on the acquisition of data appropriate to validation of multiphysics codes. A review of the state of the art in CFD Verification and Validation (V&V) was performed to inform the proposed effort, and outcomes of that review are presented here.

The advancement and availability of computational resources has led to the increased pervasiveness of simulations in scientific and engineering studies. Subsequently, simulations have progressed towards a more comprehensive modeling of physics. Simulations are capable of converging on outcomes that are incapable of being validated via data. Formalisms to insure that defendable, accurate and well circumscribed simulation outcomes are achieved are a

necessity. Nuclear reactor simulations must be carried forward with uncertainty and confidence intervals defined for simulation outcomes. Several V&V approaches have been established across disciplinary fields, causing confusion regarding what constitutes validation and verification and the definition of terms.

In a validation and verification effort there are two main components, experiments and simulations. Errors and uncertainties may exist within both. The challenge is developing and following a structured path for the quantification of the associated errors and uncertainties. Numerous professional and academic societies have undertaken the task of V&V standard development. These standards vary in the level of detail prescribed and offered but more basically in the definitions of terms.

The development of a uniform standard across disciplines would be beneficial to the advancement and adoption of computational fluid dynamics and multiphysics simulations. For a standard to see wide adoption across multiple disciplines and in industries it must incorporate a scalable approach to V&V. This approach will accommodate the scope of the project budget and value of the simulated object. As a result of the large number of simulation codes available, specific industries/societies also need to develop criteria that measure the level of user experience with a particular code. Human error will remain, for the foreseeable future, a large source of uncertainty in modeling activities.

A review of V&V Standards and Guidelines for computational simulation across various disciplines is presented with emphasis on common elements and discussion of differences in intent. The AIAA, ASME, NRC, NEA, NIST, and SFPE approaches to V&V were reviewed. The AIAA, ASME, and NEA standards and guidelines apply specifically to CFD. The NIST standard is focused on application to fire modeling using the Fire Dynamics Simulation (FDS) large eddy simulation CFD code as adopted by the US Nuclear Regulatory Commission. The CSAU methodology was developed for reactor system simulations of anticipated transients and hypothetical accidents. The review of these standards supplies a basis for adoption of best practices, or perhaps adoption of a menu of approaches to achieve a high quality simulation that is defendable. In addition to the standards reviewed for the V&V of simulations, the ASME PTC 19.1 standard for establishment of errors and uncertainties of experimental results is reviewed. These documents serve as a guide for the V&V approach taken for the NEUP project.

2.4 Computational V&V Methodologies

All of the methods reviewed require that the reality being simulated be well defined at the start. The ASME defines this reality as “truth” while noting that the exact truth cannot be known. All methods except the ASTM ask that the outcome to be predicted also be identified. The V&V process then establishes uncertainty and confidence intervals for the prescribed outcome. An example outcome might be peak clad temperature. The differences that exist between the methodologies

are in part due to difference in the intended purpose of the methods. The NEA and AIAA incorporate elements of phenomena identification and conceptual model selection in the V&V process. The CSAU and ASME standards presume the conceptual models and code are fixed at the beginning of the V&V process. CSAU presumes the code is mature and verified. Once it is established the conceptual models are appropriate to the reality to be simulated, the CSAU standard requires only a grid convergence test be performed prior to comparison with measured data to achieve a validated outcome.

The ASTM approach to code assessment is used in some organizations, such as the DOE and NRC, to establish if a code should be placed in a “toolbox”. Once a code is accepted to the toolbox it may be used for a certain class of evaluations. Additional V&V may be required for each specific analysis done using that tool. In some cases the DOE toolbox users must also be “qualified” to use the tool.

The definitions and tasks involved in the verification process are not ubiquitous across the investigated methodologies. Table 1 illustrates some of the differences in definitions employed in the V&V process for different methodologies. The level of detailed guidance provided for successful task completion varies between standards.

Table 1. Comparison of Approaches to V&V. (S. Peters et al 2011)

	Model Qualification	Model Verification	Model Validation
AIAA	Conceptual Model is developed through observation and analysis of physical system.	Only correctness of mathematical approach used in the computational model is examined.	The degree of accuracy of the computation model as representation of reality is determined in the validation. Determine if necessary physics is included
ASME	Does not address this.	Verifies code solves math equations. Estimates numerical accuracy of a specific calculation.	Determine errors due to all assumptions and the cumulative effect of the associated uncertainties.
ASTM	Requires a peer review of the physical models.	Code checking and tests of numerical robustness of the model.	Validation is how well the model represents test data.
NEA	Experts create PIRT to prioritize models required for simulation.	Suggest use of several methods to test code fidelity to conceptual models. Also advocate use of a QA code management approach.	Comprehensive assessment of model and data uncertainty used to define total simulation uncertainty.
CSAU	Experts create PIRT to prioritize models and data required for simulation.	Assumes a mature documented code with reliable numerical approach. Nodalization is examined converged outcomes.	Conceptual model quality evaluation includes comparison to test data. Validation compares simulation to integral test data.

Table 2 displays tasks associated with each verification methodology. The method of manufactured solutions (MMS) is a general procedure for generating exact analytic solutions capable of exercising relevant features of a code. Relevance of this approach is contested in some of the reviewed standards. Richardson Extrapolation (RE) is one method for obtaining an error estimate as a grid is refined.

ASME assumes that prior to code verification efforts, the code has been checked for coding errors. ASME states that code verification assesses code correctness and specifically involves error evaluation for a known solution. In contrast solution verification involves error estimation. The ASME "model" verification process purely compares mathematical and computational outcomes. The AIAA's model verification strategy is to identify and quantify error in the computational model and solution. Code checking is noted as a potential source of error reduction. It is implied that this task should be performed. AIAA's solution verification process is concerned with insufficient discretization convergence,

Table 2. Comparison of Methods used for Verification. (S. Peters et al 2011)

		Code Verification		Solution Verification
	Code Checking	Code-to-Code	Exact Analytic Comparison	Grid Refinement Studies
AIAA	X		X	RE
ASME	X	X	MMS	RE
ASTM	X		X	X
CSAU				X
NEA	QA	X	X	X

the lack of iterative convergence, and associated errors. Code checking is one of three main objectives in the ASTM model verification process. Analytic solutions, if attainable, should be compared to computational solutions. The last step in the ASTM model verification process is the estimation of the magnitude of residuals as a numerical accuracy indication and the reduction of the residuals as a convergence indicator.

CSAU assumes that a mature and documented code is being investigated, so coding errors are not addressed. It further assumes that what ASME calls code verification has been performed. CSAU model verification is concerned only with solution convergence and error estimation.

NEA suggests the use of all available methods to test code fidelity to models. NEA advocates use of a QA code management approach to reduce coding errors. It also states that manufactured solutions are incapable of aiding in verification of coding of complex algebraic expressions (wall heat transfer functions, reaction rates, etc.) and that often code developers are only capable of verifying these expressions. However, on a less rigorous level these models can be contrasted against derived physical models. This is the only methodology that does not assume all users of the code are equally experienced, but NEA provides no guidance as to quantifying user induced error.

Validation approaches for the four V&V methods are contrasted in table 3. AIAA recommends the building block approach for validation assessment. This

Table 3. Comparison of Methods Used for Validation. (S. Peters 2011)

	The building block approach	Sensitivity coefficient	Monte Carlo	Others
AIAA	X			
ASME		X	X	X
ASTM	X			
CSAU	X		X	X
NEA	X	X	X	

approach identifies uncertainty in experimental data, and compares this with the simulation outcome. NEA proposes a method similar to the AIAA for the validation process, with experiment data uncertainty quantified using ASME 19.1, and offers more detail regarding quantification of uncertainty contributions from the modeling side, including use of input sensitivity coefficients and Monte Carlo techniques. The ASME validation assessment also includes uncertainty from the model derived from the Monte Carlo or the Sensitivity method. The sensitivity coefficient method is used locally for input uncertainty propagation, and neglects non-linear effects.

ASTM validation, as implemented by NRC for FDS modeling, is accomplished by comparing the computation model to standard tests, full scale tests, proven benchmark tests, and documented fire experience. This approach is similar to AIAA's building block approach. As for CSAU, the Monte Carlo method and Latin Hypercube method are suggested for uncertainty propagation from inputs to outcomes.

2.5 Experimental Uncertainty

The V&V standards are focused on the code, and reference experimental data and related uncertainties. Validation data challenge the code in specific ways, depending on the type of data collected, including attributes like time resolution, spatial resolution, and uncertainty. This section reviews the standards for uncertainty, focusing on the ASME standard PTC 19.1 which is referenced by ASME V&V 20.

The ASME PTC 19.1 approach to experimental error and uncertainty quantification is presented. The ASME makes a concerted effort to align its approach with the International Organization of Standardization Guide to the Expression of Uncertainty in Measurement (ISO GUM). As part of the alignment effort, the definitions in these standards are largely consistent. PTC 19.1 does not use the terms bias or precision. Instead, the terms systematic error and systematic uncertainty, and random error and random uncertainty are used. The definitions of systematic error, systematic uncertainty, random error, and random uncertainty as defined in the PTC 19.1 follow: “Systematic error is the portion of total error that remains constant in repeated measurements of the true value throughout a test process; Systematic standard uncertainty is a value that quantifies the dispersion of a systematic error associated with the mean; Random error is the portion of total error that varies randomly in repeated measurements of the true value throughout a test process; and Random uncertainty is the limits to which a random error may be expected to reach with

some confidence.” (Test Uncertainty 2005) The objective of PTC 19.1 is to define and describe terms and methods necessary to provide estimates of the uncertainty in test parameters and methods, and the effects of those uncertainties on derived test results. The specification of a procedure for the evaluation of uncertainties in test parameters and methods, and the propagation of those uncertainties into the uncertainty of a test result is the scope of the standard.

In test uncertainty analysis five assumptions are made: (1) The test objectives are defined, (2) the test process (measurement processes, and data reduction processes) is defined, (3) the conditions of the item under test and measurement system employed for the test are controlled for the test duration, (4) the measurement system is calibrated and all appropriate calibration corrections are applied to the resulting test data, and (5) all appropriate engineering corrections are applied to the test data as part of the data reduction and/or result analysis process.

It is a fact that every measurement has associated error and as a result the true value of a measurement is unknowable. PTC 19.1 defines error as the difference between the measured value and the true value. The minimization of the difference between the measured and true value (error) requires that the random and systematic errors be minimized. The difference between random and systematic error is defined as the total uncertainty. Every single measurement of a parameter is influenced by elemental random error sources.

The elemental random error sources may change from measurement to measurement. Successive measurements of the same parameter yield a distribution of random errors. The population of measurements can be described using sampling statistics. The mean of the measurements is

$$\bar{X} = \frac{\sum_{j=1}^{N} x_j}{N} \tag{51}$$

The sample standard deviation is

$$s_x = \sqrt{\sum_{j=1}^{N} \frac{\left(x_j - \bar{x}\right)^2}{N-1}} \tag{52}$$

Using a sample mean as opposed to the true population mean results in the inclusion of error. Calculation of the random standard uncertainty

$$s_{\bar{X}} = \frac{s_X}{\sqrt{N}} \tag{53}$$

Allows for the definition of an interval in which the true population mean should lie.

In addition to the random standard uncertainty associated with each measurement there exists a systematic standard uncertainty. The elemental systematic error, $\beta_{\bar{X}_k}$, remains constant for successive measurements and it is an unknown. Evaluation of the elemental systematic error is obtained through engineering judgment, published information, or special data. The systematic standard uncertainty is $b_{\bar{X}}$. The total uncertainty of the measurement mean is

$$u_{\bar{X}} = \sqrt{b_{\bar{X}}^2 + s_{\bar{X}}^2} \tag{54}$$

The uncertainty of a measurement for a defined confidence interval is $U_{\bar{X}}$. It is assumed that the true value is contained within $\bar{X} \pm U_{\bar{X}}$.

In addition to the efforts to establish the uncertainty bounds associated with measurements taken during a test, pretest and post-test analysis should be performed. The objective of the pretest is to establish expected uncertainty levels prior to the expenditure of significant resources. Corrective action should then be taken to minimize excess uncertainties. The posttest analysis validates the quality of the test results and the adherence to testing requirements. It also provides a statistical basis for comparing test results.

There are six primary steps to calculating the total uncertainty associated with experimental measurements: (1) Definition of the measurement process, (2) listing elemental error sources, (3) calculation of the systematic and random uncertainty for each parameter, (4) propagation of the systematic and random standard deviations, (5) calculation of the total uncertainty, and (6) reporting of the results. The uncertainty analysis for each calculated result should be reported on two separate tables. The formats for these tables are provided in tables 4-5. Table 4 provides the information used in the calculation of the nominal value and uncertainty of the result. Table 5 provides a summary of the uncertainty information at the result level.

Table 4. Independent Parameters

Independent Parameters								
Symbol	**Description**	**Units**	**Nominal Value**	**Absolute Systematic Standard Uncertainty, b_xbar**	**Absolute Random Standard Uncertainty**	**Absolute Sensitivity**	**Absolute Systematic Standard Uncertainty Contribution**	**Absolute Random Standard Uncertainty Contribution**

Table 5. Calculated Result

Calculated Result							
Symbol	**Description**	**Units**	**Calculated Result, R**	**Absolute Systematic Standard Uncertainty, b_R**	**Absolute Random Standard Uncertainty**	**Absolute Combined Standard Uncertainty**	**Absolute Expanded Uncertainty**

2.6 Historical Single Jet Experiments

Early experiments examining jet flows are reviewed here in preparation for single jet flow measurements presented later in the dissertation. Single jets are well examined, so starting with the single jet geometry allows the ultrasonic velocity measurement to be qualified in a relatively well studied flow. The early experiments are often not well designed for CFD validation, and a common shortcoming is in the characterization of the jet inlet flow, an important boundary condition for CFD simulation.

Trüpel's experiments show that the further removed a jet is from its discharge point the wider the profile and slower the velocity. When the velocities are non-dimensionalizied and plotted versus their non-dimensional distance from

the jet discharge, the outcomes are found to be similar. This is shown in figure 4. These results are for round jets but also hold for other jet types, including plane parallel jets originating from long slots. This was verified by Förthmann's experiments.

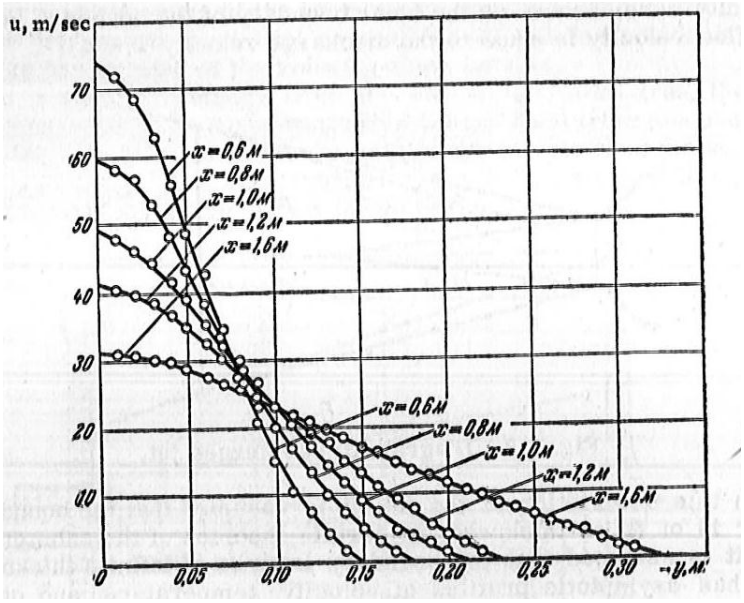

Figure 4. Trupel's Jet Spreading. (Abramovich 1963)

Tokuhiro performed efficacy studies for the use of ultrasound Doppler velocimetry for measurements of a single submerged jet in water. The experiment consisted of a submerged rectangular jet impinging vertically into a pool of water. The non-dimensional velocity and jet half radius versus axial distance was mapped with both laser Doppler velocimetry and ultrasound Doppler velocimetry. The obtained data is juxtaposed legacy data for submerged jets. Figures 5 and 6 display selected results of these efforts. The ultrasound

measurement techniques are capable of determining the general trends of the jet flow but discrepancies exist with legacy data.

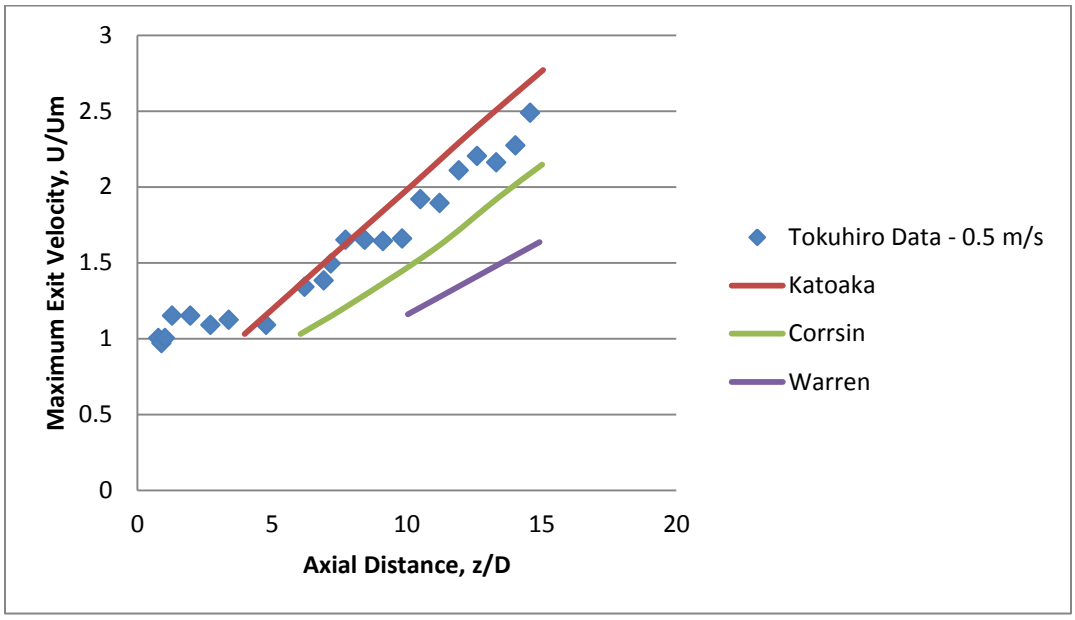

Figure 5. Decay of the Centerline Velocity versus Axial Distance. (Tokuhiro 1999)

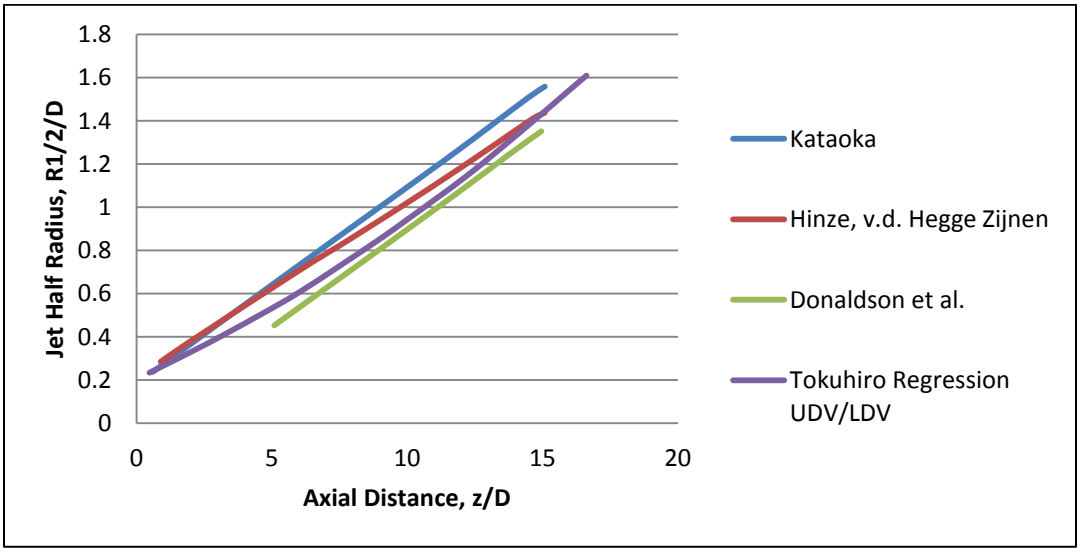

Figure 6. Jet Half Radii versus Axial Distance. (Tokuhiro 1999)

Rushton compiled an extensive history of submerged jet experiments and elaborated upon the relationships between the viscosity of the fluid and the velocity of the jet. The pertinent data are displayed in table 6. The reference numbers in this table correlate to the references citied at the end of this paper. Fossett and Prosser provide additional mixing data for small diameter jets. Rushton recommends a velocity relationship for axis-symmetric jets

$$u_r = (u_x/u_0) = 1.41 N_{Re}^{0.135} (D_0/x) \quad (55)$$

Table 6. Axial Velocities of Axis-symmetric Submerged Jets.

	Ref. No.	Temp., (Celsius)	Diameter (cm)	Velocity (cm/s)	Viscosity (Stokes)	N_{Re}	$N_{Re}^{0.135}$	u_r at x/D=30	K, calculated
Air	1	18	2.54	6200	0.151	1.05E+05	4.76	0.23	1.45
Air	2	20	10	2500	0.253	1.60E+05	5.03	0.23	1.37
Air	2	20	10	2800	0.153	1.80E+05	5.11	0.24	1.41
Air	3	20	4	5400	0.153	1.40E+05	4.96	0.23	1.39
Air	4	22	2.87	662	0.156	1.20E+04	3.56	0.17	1.43
Air	4	700	2.87	1715	10.65	4.60E+02	2.29	0.11	1.44
Air	5	18	2.54	1000	0.151	1.40E+04	3.62	0.18	1.49
Air	5	18	7.62	2050	0.151	1.00E+05	4.75	0.22	1.39
Air	2	20	10	2660	0.153	1.70E+05	5.08	0.27	1.59
Air	6	18	12.7	382	0.151	3.20E+04	4.05	0.22	1.63
Air	7	18	15.25	51	0.151	5.10E+03	3.15	0.13	1.24
Air	7	18	15.25	178	0.151	1.80E+04	3.76	0.15	1.2
Air	7	18	15.25	254	0.151	2.50E+04	3.92	0.18	1.38
Air	7	18	15.25	508	0.151	5.10E+07	4.32	0.2	1.39
Air	7	18	15.25	1270	0.151	1.30E+05	4.91	0.22	1.35
Air	7	18	15.25	3050	0.151	3.10E+05	5.48	0.22	1.21
Air	8	20	7	1000	0.153	4.60E+04	4.28	0.18	1.26
Air	9	20	7.2	450	0.153	2.10E+05	5.21	0.25	1.44
Air	10	18	15.25	2500	0.151	2.50E+05	5.36	0.25	1.4
Air	11	20	0.25	4130	0.153	6.70E+03	3.28	0.15	1.43
Air	11	20	0.25	30600	0.153	5.00E+04	4.32	0.22	1.53
Air	12	20	5	295	0.153	9.60E+03	3.46	0.18	1.56
Air	12	20	5	1200	0.153	3.90E+04	4.17	0.21	1.51
								Average =	1.41
								Calculated	K Assumed
Water	13	13	0.661	299	0.01	2.00E+04	3.8	0.18	1.41
Hydrogen	14	18	0.635	3250	1.03	2.00E+03	2.79	0.13	1.41
Air	14	18	0.635	3250	0.151	1.40E+04	3.63	0.17	1.41
Sugar in water	14	18	0.635	3250	0.13	1.60E+04	3.68	0.172	1.41
Water	14	18	0.635	3250	0.01	2.00E+05	5.18	0.24	1.41
		18	0.318	-	0.01	5.60E+03	3.2	0.15	1.41
Water	14		to			to			
		18	1.59	-	0.01	4.20E+04	4.2	0.2	1.41

[1] (Albertson 1948) [2] (Kuethe 1935)[3] (Cleve 1937)[4] (Cleeves 1947)[5] (Corrsin 1943)[6] (McElroy 1943)[7] (Nottage 1952)[8] (Predvoditelev 1936)[9] (Ruden 1933)[10] (Tuve 1944)[11] (Voorheis 1939)[12] (Zimm 1921)[13] (Binnie 1942)[14] (Donald 1959)

2.7 Dual Jets Historical Experiments

Several experiments have examined twin parallel mixing jets, and these experiments are closely related to this research. The previous experiments were in some cases intended to validate CFD predictions. However, prior twin jet experiments did not carefully control or characterize the inlet flow, and the velocity field data is not as spatially resolved as that presented later in this research.

Tanaka in 1970 and 1974 studied several entrainment mechanisms and flow parameters for parallel jets. He described three regions of the flow field for parallel jets, depicted in figure 7. The first flow field is the converging region and initiates at the jet origin and ends where the inside shear layers of the respective jets merge. The point of merging is termed the merge point. The merging of the jets is due to the entrainment rate between the jets. The entrainment results in a below ambient pressure region between the jets. The velocity is zero at the merge point, located on the plane of symmetry. The merging region exists between the merge point and the combined point. The combined point is the point of maximum velocity on the plane of symmetry. A plane of symmetry is established, centered equal distance from jet origination, for jets of similar velocities. This plane of symmetry corresponds to the x-axis in figure 7. The combined region exists beyond the combined point. In this region the two jets begin to resemble a self-similar single jet.

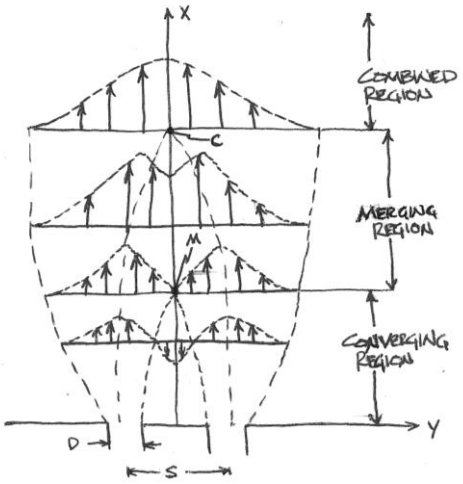

Figure 7. Velocity Profile of a Typical Dual Jet.

Anderson and Spall performed experimental and numerical investigations of turbulent plane parallel jets in air for various jet spacings. Depicted in figure 8 are results from those efforts. The graphs are the experimental and numerical simulations of the measured velocities along the plane of symmetry for jet spacing based on ratio S/D per figure 8 of 0, 9, 13, and 18.25. The numerical simulations used a k-ε turbulence model and a Reynolds stress transport model (RSM). The employed model predicts the velocity profiles along the symmetry line well. However, it is noted that when comparing a collection of historical merge and combine points with the results (experimental and computational) reported by Anderson and Spall, the results fluctuate. This collection of data is presented in figure 9. They postulate that the dispersive results are due to phenomena that are unique to each experimental facility, possibly localized to varying inlet conditions.

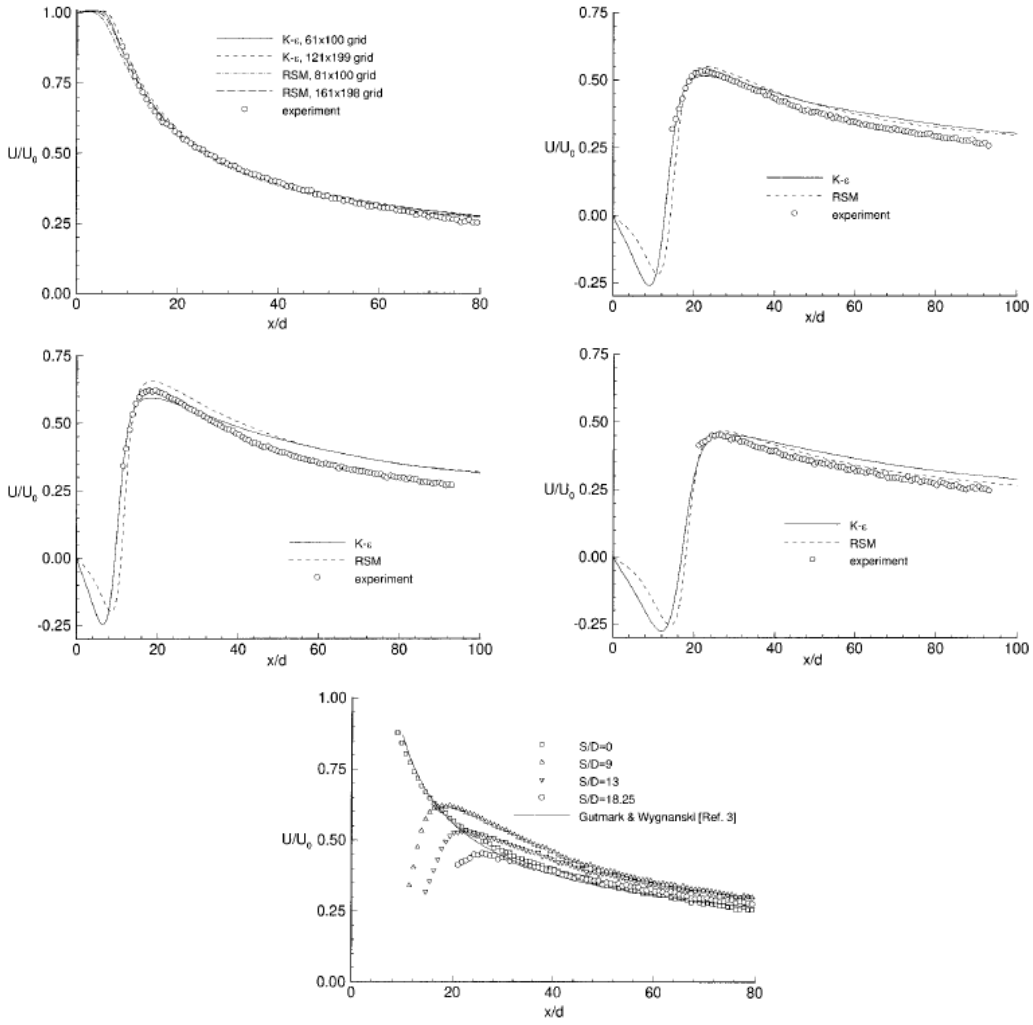

Figure 8. Anderson and Spall Centerline Velocity Profile Results. (Anderson and Spall 2001)

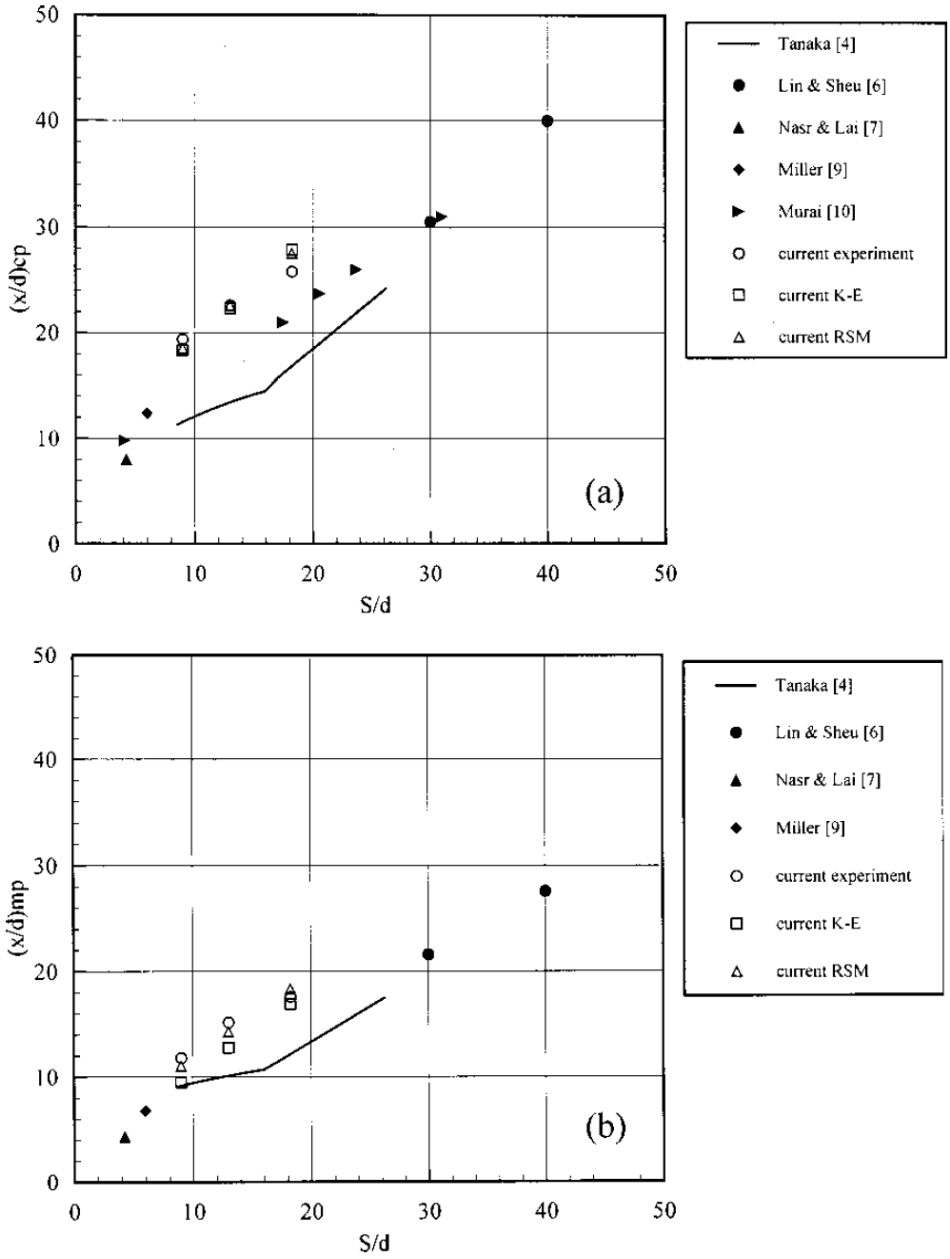

Figure 9. Anderson and Spall plus Historical Results (a) merge and (b) combine point. (Anderson and Spall 2001)

Anderson performed additional studies with plane parallel jet experiments with nozzle diameter to jet spacing larger than 0.6. The range investigated was 0.6-2.0. A periodic bluff-body-type vortex shedding phenomena was detected in this range. It appears that the fluid supply for this experiment originated from a single chamber. For parallel jets with a jet diameter to spacing less than 0.6 this phenomena is not observed. Instead, counter rotating recirculation zones develop between the jets due to lower pressure, reaching a maximum pressure at the merge point.

The objective of this project is to obtain the data necessary for the validation of CFD code for liquid metal jet mixing phenomena. Various approaches to code validation are reviewed. A literature review of jet turbulence theory and single and dual jet historical experiments are performed. These reviews provide the context for the simulations used to guide design of the experimental facilities. The simulations also provide a level of expectation for velocity gradients that will occur in the proposed test facilities. These simulations serve to provide an initial starting point for instrumentation related decisions.

CHAPTER 3

FACILITY DESCRIPTION

The purpose of the UTK WTF, shown in figure 10, is to qualify the measurement technique, and acquire data suited to CFD validation efforts. The WTF provides a tertiary data set that complements the sodium experiments

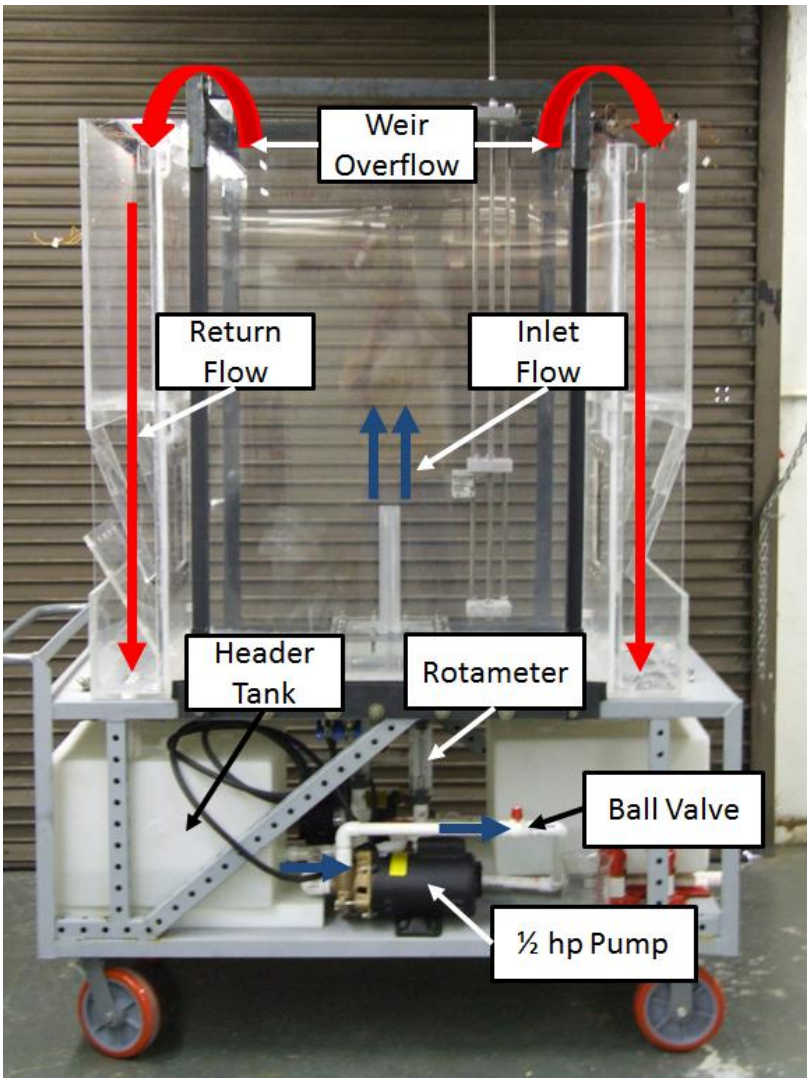

Figure 10. The UTK Water Test Facility

at the University of Idaho and the mercury experiments at the University of Tennessee. Pursuant to the objective of providing a comparable data set to the mercury and sodium experiments, the water test section is designed to operate at a jet Reynolds number equal to 18000, consistent with jet flows planned for the liquid metal experiments. The WTF is capable of operation as a dual jet or a single jet facility. In the dual jet mode, the velocity and temperature of each jet operates independently with separate pumps, separate flow meters and separate pump suction reservoirs. Dimensioned CAD drawings of the as-built facility are provided in figures 11-14. These drawings were provided to ANL where they are being used to provide boundary conditions for the CFD simulations. The instrumentation support structures are included in those simulations.

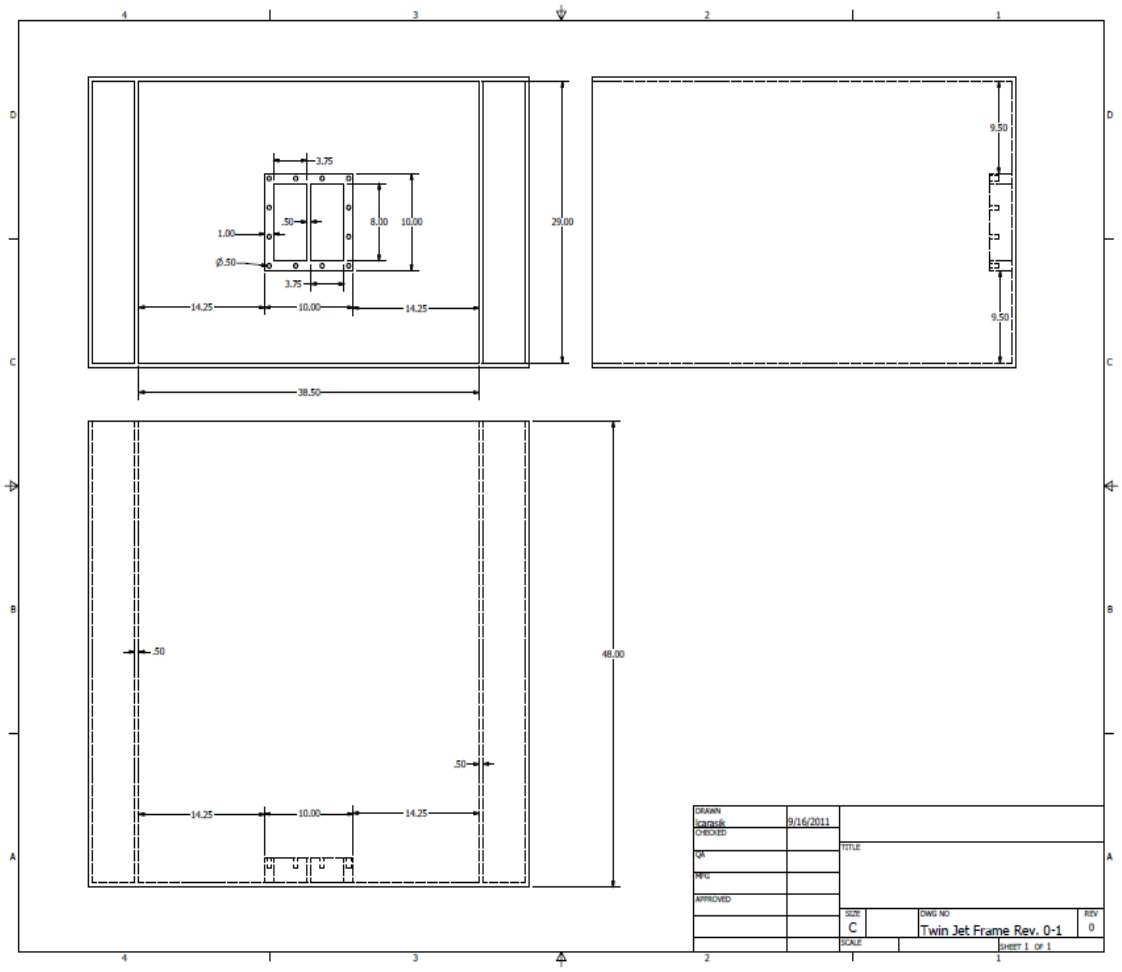

Figure 11. Twin Jet Frame.

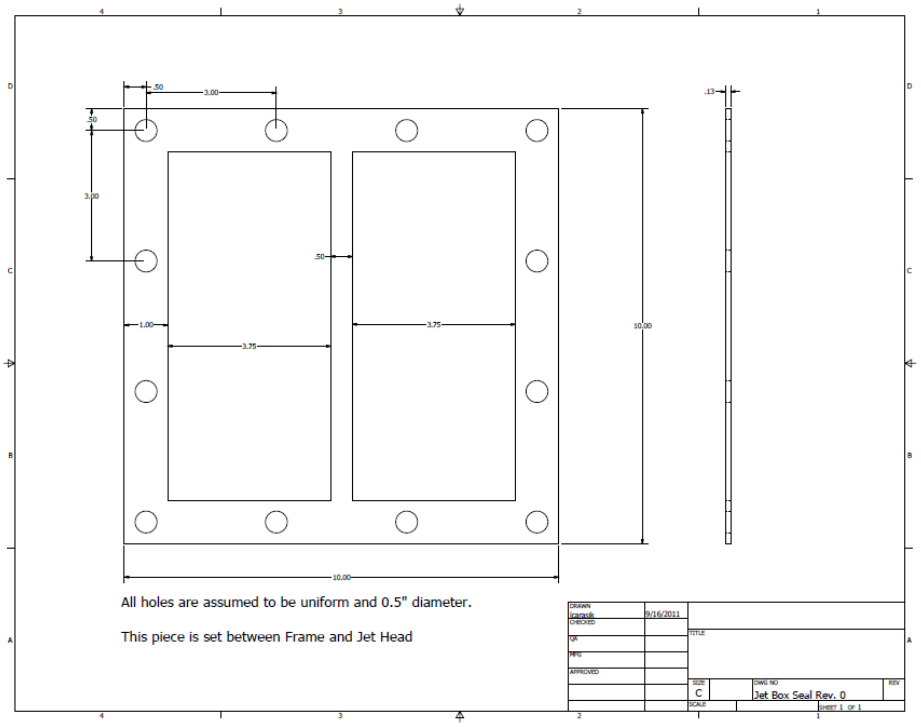

Figure 12. Jet Box Seal.

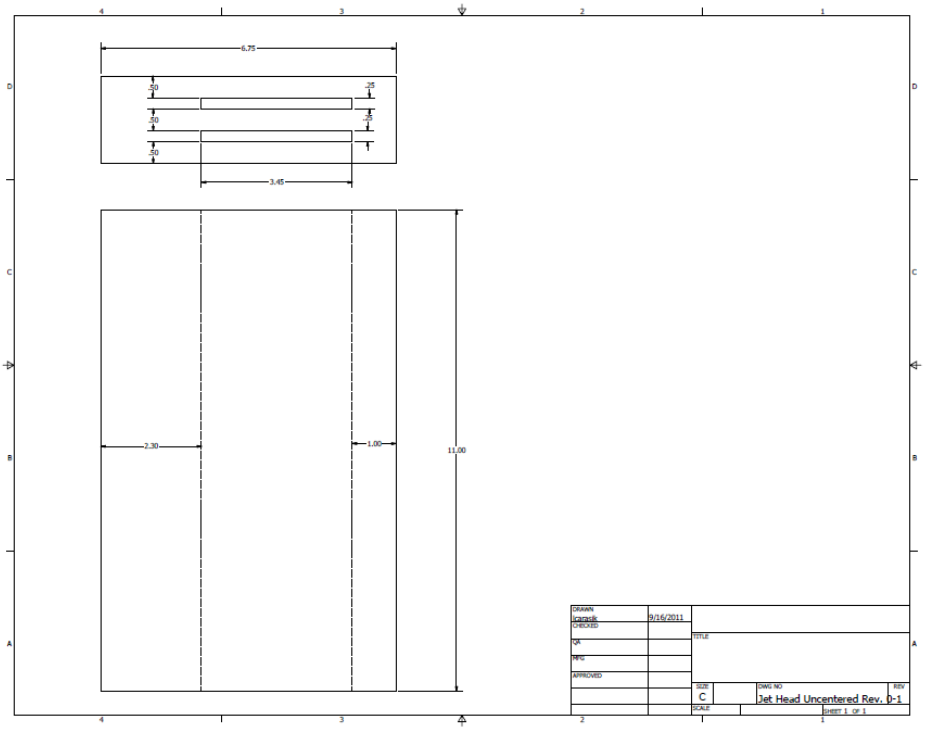

Figure 13. Jet Head Uncentered.

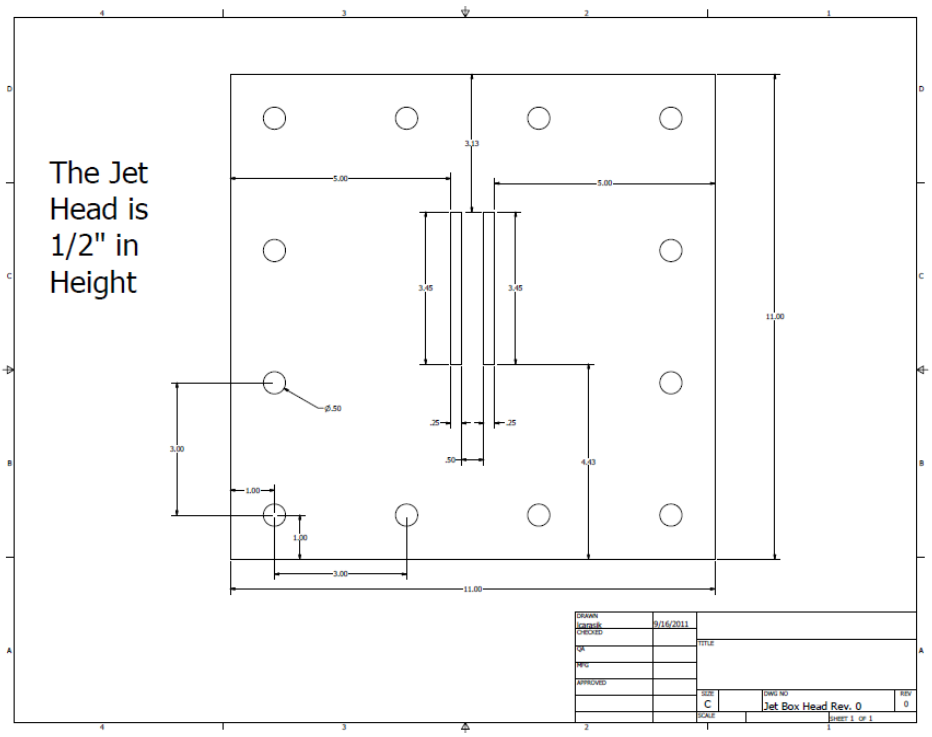

Figure 14. Jet Box Head.

Design constraints include the minimum resolution of the ultrasound, the measurement range of the two rotameter flow meters (Manufacturer: King Instrument Company, S/N: 2575051101) and the pumping capacity available. Subsequent test section dimensions were tailored to achieve the target Reynolds number, subject to the design constraints. The rotameter flow range is 2-20 gpm (1.2618E-4 – 1.2618E-3 m^3/s) with accuracy plus or minus 4 percent. The centrifugal pumps chosen for the water test section are 1/2 hp (Manufacturer: WEG, Model: 1UMO+CLNCJ1/202E). These pumps are capable of producing a maximum of 10 gpm at 40 ft of head and are fitted with a 3.175 cm intake and a 2.54 cm discharge. Figure 15 depicts the flow loop plumbing and the flow control system. The as-built dimensions of the jet inlet cross-sections are 8.8 cm by 0.6

cm, and the gap between the jets is 1.2 cm as shown in figure 16. Figures 17 and 18 are pictures of the jet lid and inlet geometry.

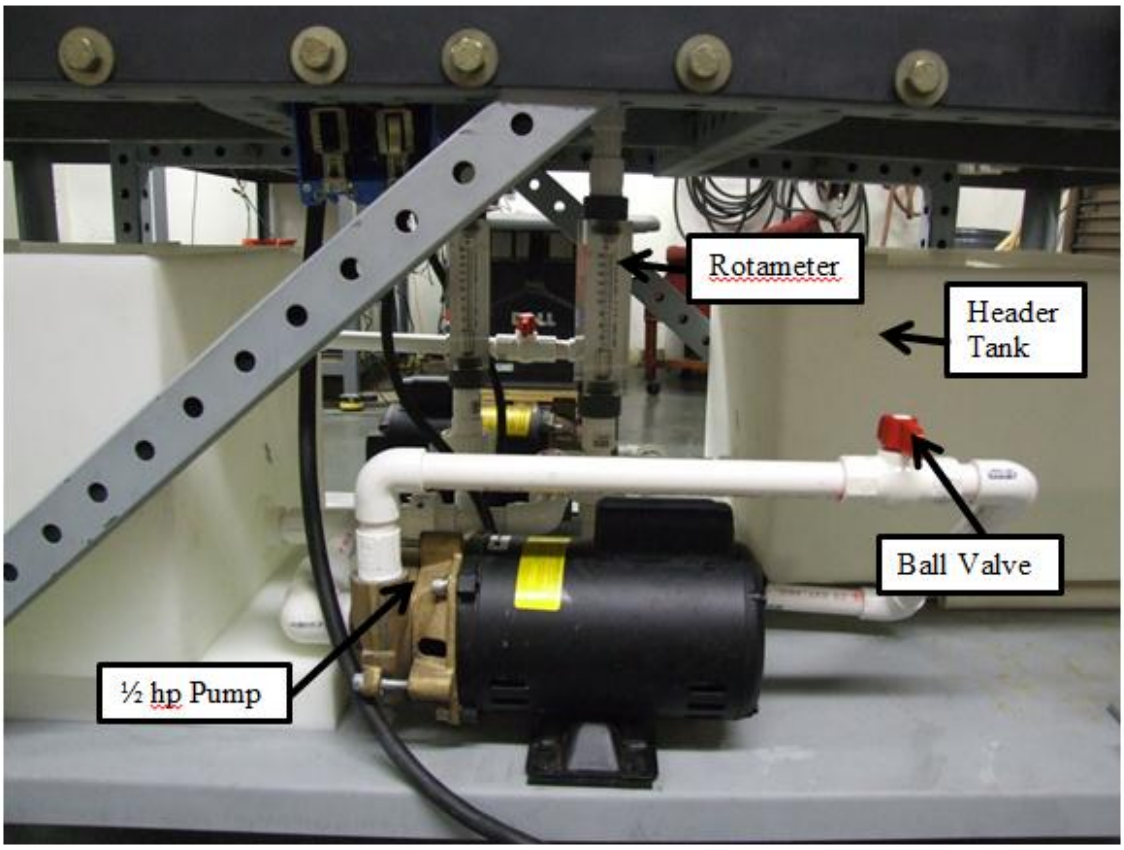

Figure 15. Water Facility Plumbing

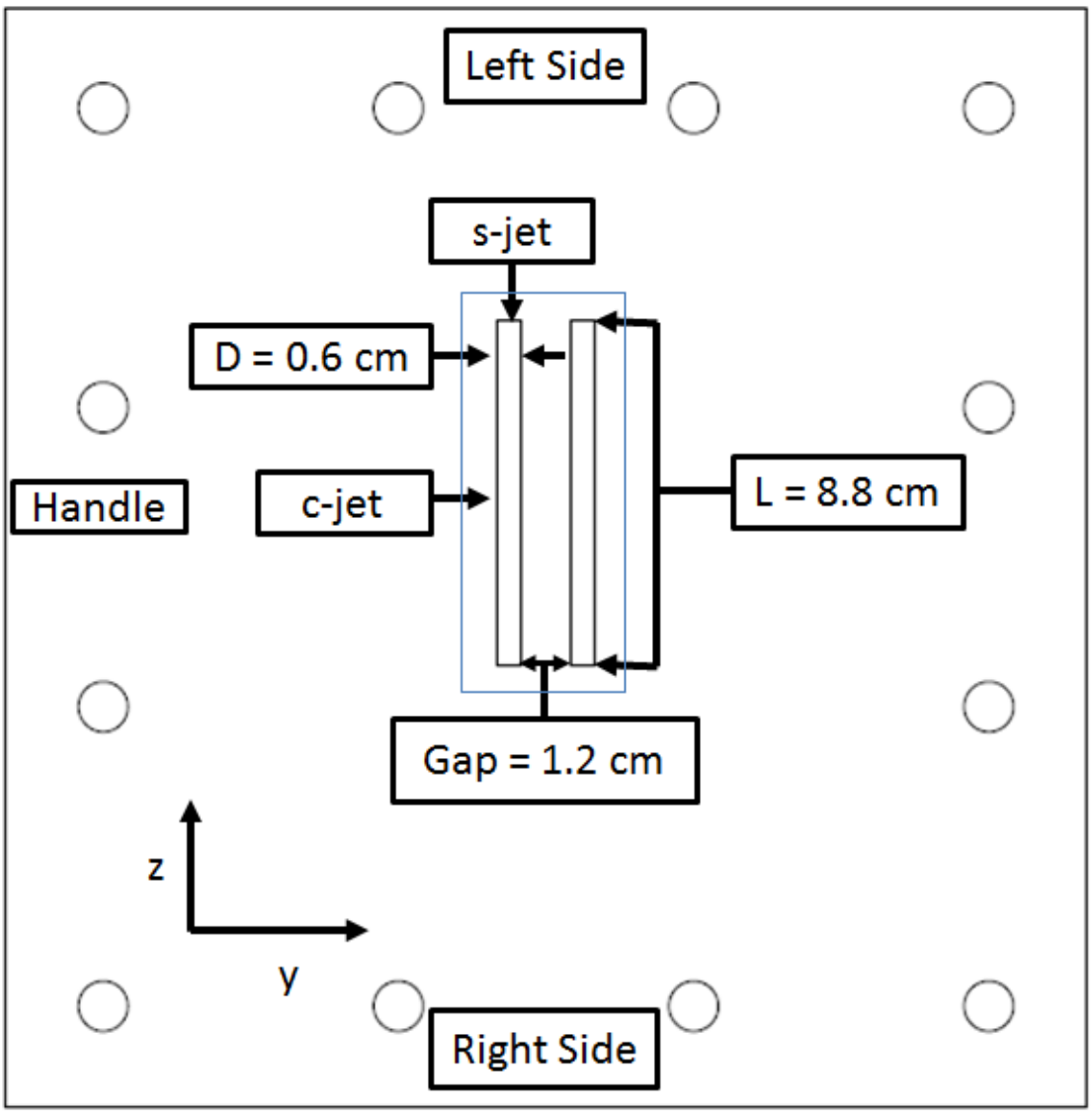

Figure 16. Dimensioned Jets

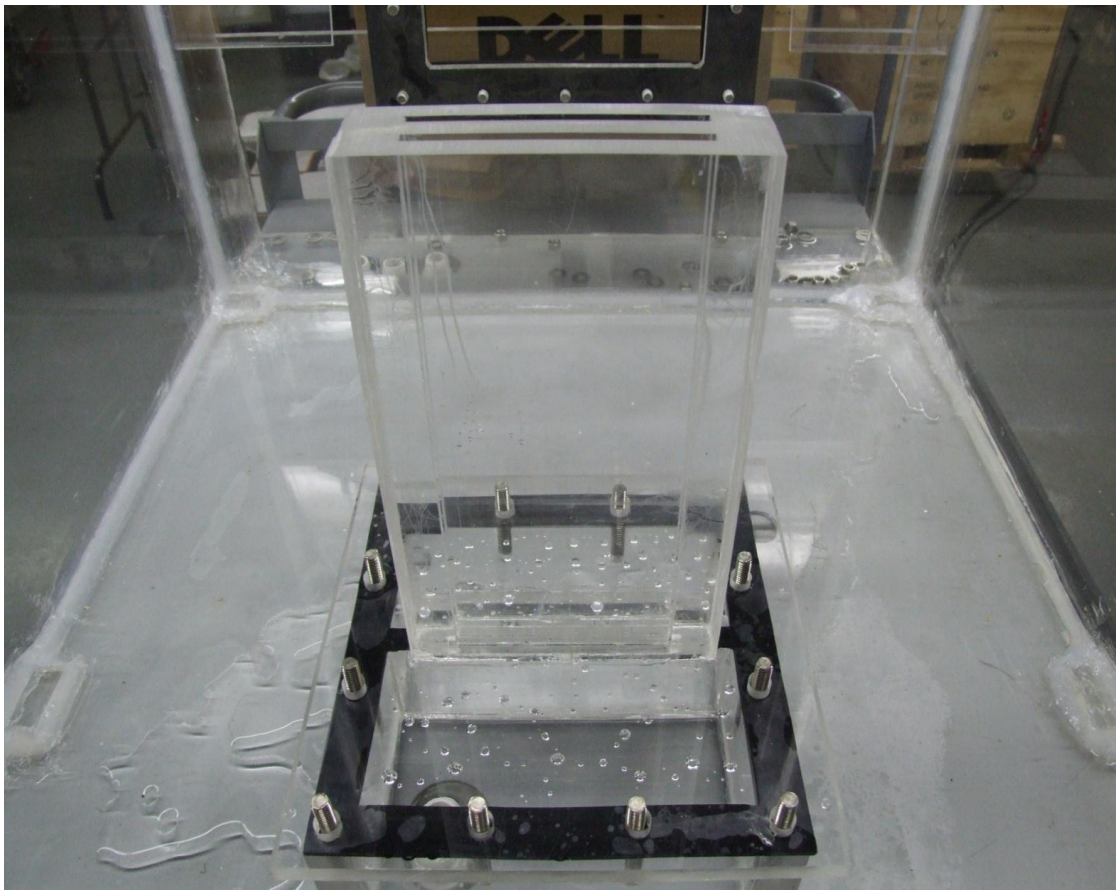

Figure 17. Rectangular Jet Outlet

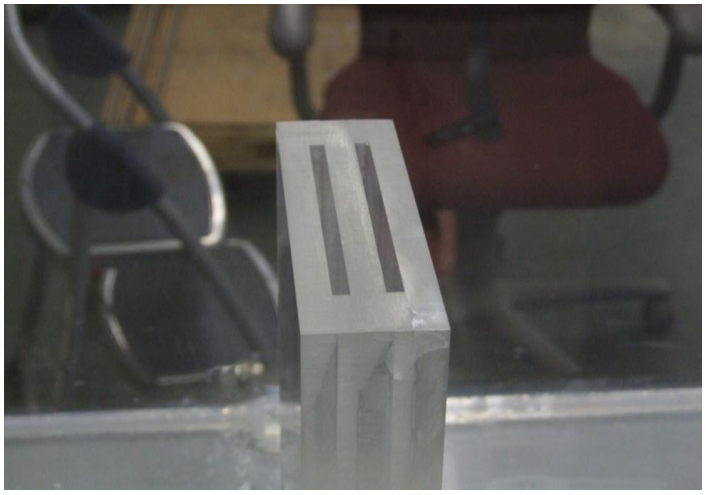

Figure 18. Close Up of the Jet Outlet

The jet width is 9 times the minimum recommended spatial resolution of the UVP system. Holding the width of the rectangular jet constant and applying the set point constraint, the maximum length of the jet is calculated such that the volumetric flow of the jet is constrained by the achievable and measurable system volumetric flow rate. An Excel sheet is composed to iteratively determine the jet velocity based on varying jet dimensions. The required velocity to achieve a Reynolds number equal to 18000 is calculated

$$v = \frac{Re * \mu}{\rho D_h} \tag{56}$$

where μ is the dynamic viscosity of the fluid, ρ is the density of the fluid, and D_h is the hydraulic diameter of the jet. The velocity required to maintain a Reynolds number equal to 18000 is compared against the volumetric flow rate of the jet exit. At a flow rate of 12 gpm the setpoint is achieved if the jet cross-section length is 8.763 cm. Results of these iterations are displayed in table 7. The properties of water used for the calculations of the maximum velocity and maximum volumetric flow for the water jets at room temperature (25 C) and ten degrees above room temperature are depicted in table 8. Table 7 can quickly be reevaluated for experiments where hot water is run through one of the jets, using table 8.

Table 7. Excel Sheet for Water Facility Flows.

L (cm)	W (cm)	P (cm)	A (cm^2)	Dh (cm)	V (cm/s)	Vol Flow (cm^3/s)	GPM
9.144	0.635	19.558	5.80644	1.187532	135.4459	786.4587403	12.46563
9.017	0.635	19.304	5.725795	1.186447	135.5698	776.2449905	12.30373
8.89	0.635	19.05	5.64515	1.185333	135.6972	766.0312406	12.14184
8.763	0.635	18.796	5.564505	1.184189	135.8283	755.8174907	11.97995
8.636	0.635	18.542	5.48386	1.183014	135.9633	745.6037408	11.81806
8.509	0.635	18.288	5.403215	1.181806	136.1023	735.389991	11.65617
8.382	0.635	18.034	5.32257	1.180563	136.2455	725.1762411	11.49428
8.255	0.635	17.78	5.241925	1.179286	136.3931	714.9624912	11.33239
8.128	0.635	17.526	5.16128	1.177971	136.5453	704.7487413	11.1705
8.001	0.635	17.272	5.080635	1.176618	136.7024	694.5349915	11.0086
7.874	0.635	17.018	4.99999	1.175224	136.8645	684.3212416	10.84671
7.747	0.635	16.764	4.919345	1.173788	137.032	674.1074917	10.68482
7.62	0.635	16.51	4.8387	1.172308	137.205	663.8937419	10.52293
7.493	0.635	16.256	4.758055	1.170781	137.3839	653.679992	10.36104
7.366	0.635	16.002	4.67741	1.169206	137.5689	643.4662421	10.19915
7.239	0.635	15.748	4.596765	1.167581	137.7605	633.2524922	10.03726

Table 8. Water Properties of Interest.

Water @ 25 C			Water @ 35 C	
Re	18000			
mu	0.00891	g/(cm*s)	0.0072	g/(cm*s)
rho	0.9971	g/cm^3	0.9941	g/cm^3

The jet lid used for these studies is made of ½ inch clear acrylic as pictured in figure 17 and figure 18. The presented experiments are performed at a volume flow rate of 10 gpm and a Reynolds number of 15024. The water facility is capable of operation at Reynolds numbers from 3000-30000. Depicted in figure 19 are the jets and entrance chambers that provide the opportunity for the flow to transition from the circular supply piping to the rectangular jets.

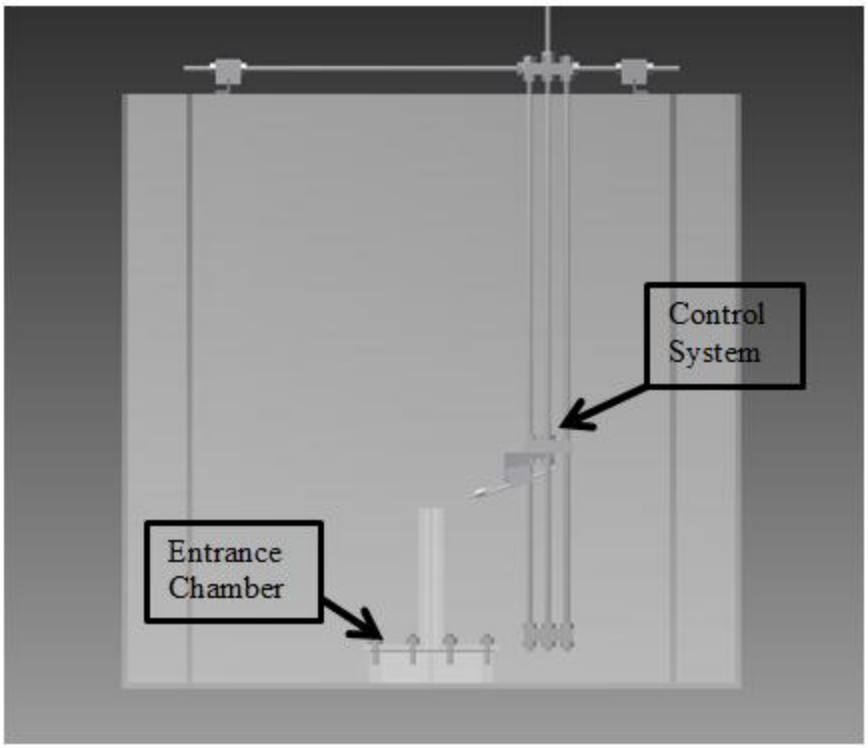

Figure 19. CAD Drawing of Water Facility

The deviation of the jet dimensions from the as-built values highlighted in table 7 to the values calculated to obtain the flow condition of Reynolds number equal to 18000 is attributed to the uncertainty associated with the formation of the extruded acrylic product and the bonding of the acrylic pieces. The extruded acrylic sheets are prone to shrinkage in the direction of extrusion and expansion perpendicular to the direction of extrusion. This type of acrylic has the potential to absorb fast drying solvent cements faster than cast or continuous cast acrylic. This may result in joint failures and incomplete gluing. This knowledge is important for construction of large volume tanks.

The flow for each jet must traverse a minimum distance to assure that each jet exhibits a fully developed velocity profile at the entrance into the test section. The developing length required to achieve a fully developed turbulent flow for the as built hydraulic diameter and a 10 gpm flow rate is

$$L_e = 4.40 D_h Re^{1/6} \quad (57)$$

The minimum required developing length is approximately 24.55 cm. The developing length is set to 27.94 cm. The fully developed jet inlet flow is useful to planned CFD simulations.

The position control system for the ultrasound transducer is depicted in figure 19. Figures 20-21 provide close up views of the as built control system. This system is designed to have the flexibility to attach various types of instrumentation. The 4 MHz ultrasound probe is shown mounted on the position control system in figure 22. The probe is held stationary by a collar that is welded to a steel rod.

Figure 20. Top of Control System.

Figure 21. Bottom of Control System

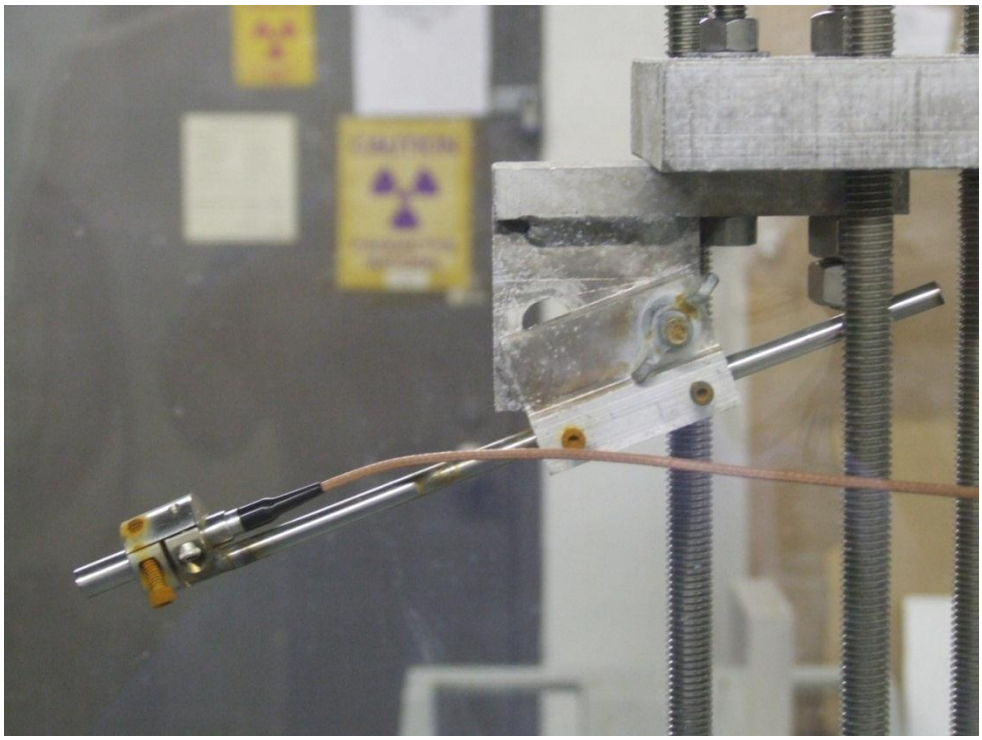

Figure 22. 4 MHz Ultrasonic Probe in Mounting.

The rod is bolted to a stationary block at an angle of 20 degrees. The angle of the ultrasound probe can be increased or decreased as needed. The block, depicted in figure 22, holding the ultrasound probe is penetrated by 4 rods. The outside rods are stationary and run down to an anchor plate. These three rods provide the tracks for the probe's vertical control (x-direction motion). The center rod (the vertical control rod) is restricted to the holding block via nuts and washers. This rod can be raised and lowered manually. The vertical displacement is controlled by a raising and lowering of a nut on the control plate. This method provides for fine adjustments of the vertical position of the probe. The vertical displacement of the probe is measured as the displacement of the

vertical control rod. This is measured using a micrometer, and a meter stick is used when the displacement exceeds the 150 mm range of the micrometer. The micrometer is accurate to 0.01 mm and the meter stick is accurate to 0.5 mm. The black steel frame, shown in figure 20, provides the tracks for z-direction positioning. The probe is typically zeroed on a repeatable portion of the jet and displaced in the z-direction to a measurement location. The aluminum blocks depicted in figure 20 are manually repositioned along the frame to vary z-direction position. The z-direction displacement is measured via two meter sticks permanently attached to the frames, and is accurate to 0.5 mm. The motion in the y-direction is controlled by the two rods that penetrate the aluminum blocks depicted in figure 20. The control block is positioned so that the ultrasound probe is zeroed on a repeatable point in the test section and then two nuts are tightened against each other so that they do not move during the course of the experiment. The control block is displaced from the two stationary nuts and it is held in position by additional nuts and washers.

The ultrasound machine that drives the 4MHz ultrasound probe is the Met-Flow UVP-XW-Psi. This system was built in the early 1990's and is capable of employing an array of ultrasonic transducers of different frequencies.

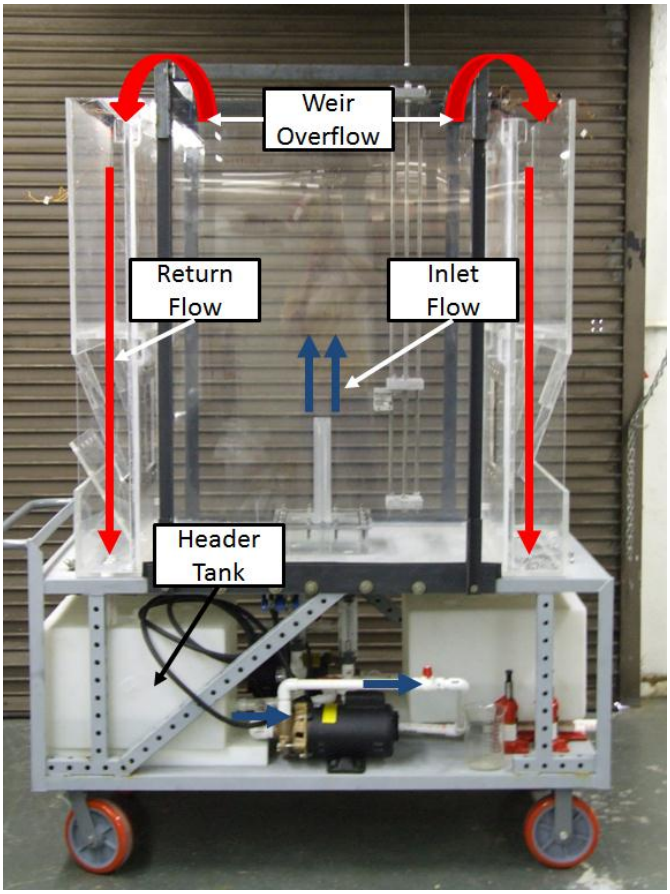

Figure 23. Water Test Facility

The tank outflow is at the top surface over two weirs as shown in figure 23. Flow over the weirs is controlled by the test section incline. Four bottle jacks depicted in figure 24 are used to raise the cart and test section off the floor. Fine adjustments of the test section incline are achieved with these bottle jacks, allowing control of flow over the two weirs.

Figure 24. Bottle Jack Used for Water Test Facility.

There are two access ports on opposing sides of the water test facility. These are designed to provide both a method of draining the facility, once testing has concluded, and provide easy access for changing the jet geometry. The ability to quickly and easily exchange the jet lid geometry adds to the versatility and uniqueness of the facility.

The water test facility is situated on a rolling cart as shown in figure 23. This cart was modified from the original purchased design. It was determined that additional steel supports were necessary to support the 2000 plus pounds of the filled test section on the top shelf. The bottom shelf of the cart holds the two pumps, two flow control valves, two flow meters, and the two header tanks. These components are labeled in figure 15. The two 17 gallon header tanks

allow each jet to be supplied with water of different temperature. This functionality has been exercised and the results were presented in Peters 2011. The volume flow rate of each jet is controlled by independent ball valves. These valves provide a significant source of flow pressure loss but the size of the pumps provide sufficient energy to overcome these losses. There is also a flow line between both header tanks with an isolation valve. When the flow loops are operating isothermally this line remains open. When the flow loops are operating non-isothermally this line is closed and the header tanks are isolated.

CHAPTER 4

ULTRASONIC MEASUREMENTS AND THEORY

4.0 Instrumentation

The single jet and twin jet fluid velocities are measured via ultrasonic interrogation. The attributes of this measurement approach are presented here as a fundamental component of qualifying the data for CFD validation. Almost all measurements are inferences, and the transfer from the actual measured quantity (i.e., Doppler shift of an acoustic echo) to the reported quantity (i.e., fluid velocity) is presented here.

A Metflow UVP-XW-Psi is used in combination with a 4 MHz transducer to obtain a profile of the velocity field at discrete volumes along the measurement axis. The returned value of the velocity volume is a function of space and time and additional factors that govern ultrasonic measurements. It is important to note that the ultrasonic velocimetry measurements are not direct measurements of the fluid velocity. Instead ultrasound velocimetry tracks the motion of particulate in the flow field based on the Doppler shift of the echo returned from the particulate. The critical assumptions made with this measurement approach are that the particulate (seeds) returning echoes follow the motion of the fluid, and that they differ in their acoustic impedance (ρc) from the fluid of interest.

The UVP model employed can accommodate a 1 MHz, 2 MHz, or 4 MHz transducer. A 4 MHz transducer is used here for all measurements. The seeds

imaged in the investigated flow fields are particulate that are typically present in the Knoxville, TN tap water. The details of the imaged seeds are unknown. Based on ultrasound reflection theory, it is surmised that the size of the particulate is of the order λ/4, where λ is the wavelength of the pressure wave emitted by the transducer. The suggested minimum seed diameter for a 4 MHz transducer is 92.5E-6 m. The particulate present in the tap water may be below this threshold. Experiments using seeds (Type: Polyethylene; Size: 355-425 μm) in the water did not improve the performance of the measurements.

The 4 MHz transducer employed is a piezoelectric transducer that emits a plane wave. A diagram of a typical piezoelectric transducer is provided in figure 25. Piezoelectric transducers convert electric pulses into mechanical waves and can convert mechanical waves into electric pulses. They achieve this by electrostriction. Electrostriction is a property of dielectric materials. When an electric field is applied the molecules in the material align with the electric field causing the material to have a minute change in dimension, creating a mechanical wave.

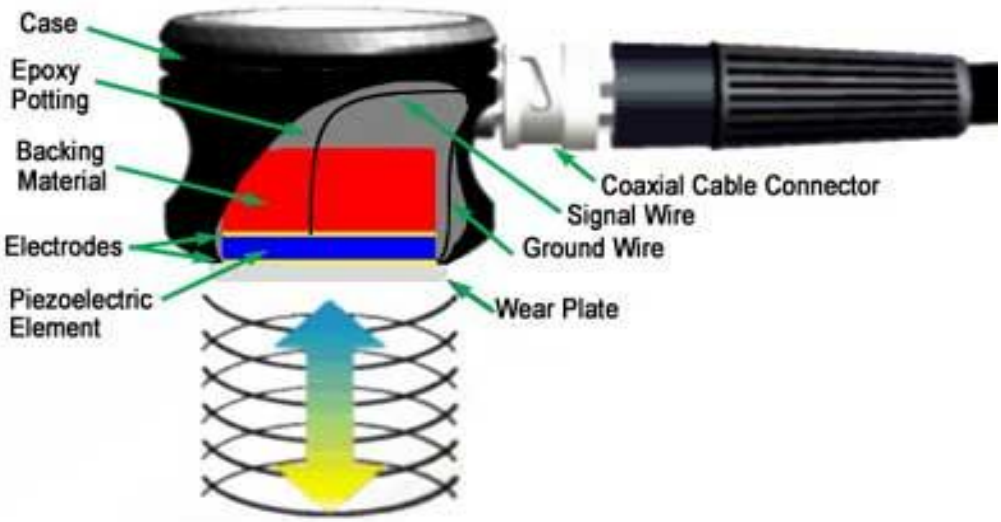

Figure 25. Piezoelectric Transducer. **(**NDT Resource Center January 2011)

The mechanical waves induce sound waves that propagate through the fluid medium. Upon reflection from a seed particle the transducer switches from a transmitting mode into a receiving mode. The received sound wave is converted from a mechanical wave into an electric signal. The electric signal is then processed via the Metflow software.

The functionality of ultrasonic velocity profiling is based on Doppler shift theory. Subsequently, it is important to know the rate at which sound propagates in the medium of interest, the velocity and position of the transmitter/receiver, and the reaction of the particulate imaged to pressure wave impingement. A sound wave that impinges a moving particle is partially reflected back towards the source. The frequency of the reflected sound wave is shifted. This shift in frequency is termed the Doppler shift. The Doppler shift of sound waves is

experienced when the sirens of an approaching emergency vehicle are at a higher frequency than the sound of the sirens of the same emergency response vehicle as it recedes from the observer. In this example it is apparent that the frequency heard by the observer is dependent not only upon the speed and direction of the approaching source but also upon the speed and direction of the observer.

Particles significantly less than the ultrasound wavelength, λ, undergo Rayleigh scattering. If the particles are the same density as the fluid medium but they have a different compressibility, the particle will emit a monopole response. It expands and contracts at a specific frequency. If the compressibility of the particle is the same as the fluid medium and the density of the particle is different, then the particle will emit a dipole response, where it oscillates back and forth in response to the incident wave.

The response of particles that are the size of the ultrasound wave length is governed by Mie theory (Geisler 2001). In electromagnetic theory, the Mie solution describes the scattering of electromagnetic radiation from a sphere. The specific response will depend on the density and compressibility with respect to the medium with which the sound wave is transmitted. The response of a perfectly spherical seed can be calculated exactly based on Mie theory. The dependence of the particle response allows for the signal to be distinguished between solid and gaseous particulate. Within the Rayleigh regime the backscatter radiation increases with the size of the particle. Particles that

experience Mie scattering oscillate about the maximum backscatter response. This makes particulate that experience Mie scattering the optimum choice for imaging.

The signal strength at the moment of interaction with a seed particle decreases with the distance from the generation source. The reduction in signal strength occurs because of the spreading of the wave from the source and because of attenuation (absorption and scattering). Sound waves propagate through a medium due to the potential energy stored during the compression of a volume and the imparting of the potential energy into kinetic energy of particles. Energy is taken away from the system (acoustic wave) through attenuation. The attenuation along the axis of measurement is described by Beer's Law (Geisler 2001).

$$p = p_0 e^{-\alpha d} \tag{58}$$

where p_0, p are the pressures at the start of the signal and end of the signal, α is the coefficient of attenuation and d is the distance along the line of propagation. The attenuation coefficient for echo strength, but not for Beer's law, depends on the square of the ultrasound frequency. This indicates that the frequency of the transducer chosen must be balanced against the field of view required. Higher frequency transducers yield higher spatial resolution over shorter distances and lower frequency transducers have lower spatial resolution, but over much longer distances.

Following Huygens theory, it is assumed that every point on the surface of the active region of the transducer plate is the origin of a source for a spherical wave. This theory restricts the propagation of waves to the forward direction. If the transducer is operated in a continuous wave mode, the principal of superposition of waves indicates that the center of the transducer will provide the maximum amplitude source. Surrounding this center lobe will be progressively smaller lobes. However, if the transducer is critically damped and operated in a pulse wave mode then the side lobes are mitigated and the amplitude of pressure waves across the transducer face is of constant angle. A depiction of the amplitude of a constant angle is provided in figure 26. The transducer employed in all experiments operates in pulse wave mode. As the distance from the transducer face increases the ultrasound beam diverges. The divergence of the beam is dependent on the ultrasound wavelength and the active area of the transducer face. The divergence of the beam adversely affects the beam strength at distance. Additionally, the divergence of the beam affects the volume in which echoes are generated.

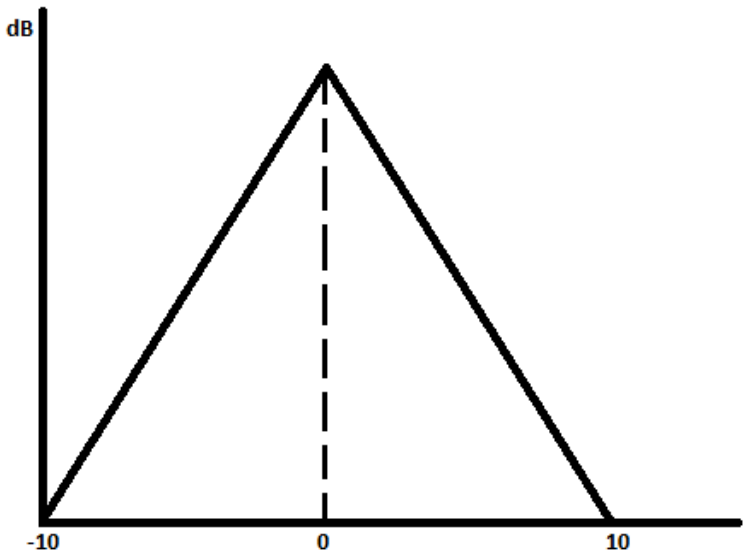

Figure 26. Pulsed Ultrasonic Beam Profile

The employed transducer operates in pulse echo mode. The transducer first emits a pulse and then switches to a listening mode and waits for a response from a particle. It is important to know the angle of the transducer with respect to the direction of flow. The particle trajectory forms a Doppler angle with respect to the measurement axis. Only the particle's velocity component along the measurement axis contributes to the measured Doppler shift. The speed of the particle is

$$v = \frac{v_a}{\cos\propto} \tag{59}$$

where α is the Doppler angle. It is important to note that the velocity measurements are of discrete particles located somewhere in the active volume of the transducer. As a result of beam divergence, the measurement volume

should increase with distance away from the transducer face. If the angle of divergence is small and the measurement window is short, it may be appropriate to assume the cross sectional area of measurement is constant. The Metflow machine approximates the diameter of the measurement volume as the diameter of the main lobe, based on a base model transducer that they produce. The echoes that are recorded within a specific volume are averaged and assigned to the center of the volume. The Doppler angle adjusted velocity is a projection of the one component of the Doppler shifted velocity. The recorded speed of the volume in the direction of flow could be different from Doppler angle adjusted velocity of the particles that produced echoes from that volume as is addressed in more detail later.

The selection of the angle of the ultrasonic probe and the certainty with which the angle of the probe is situated is important to obtaining accurate velocity profiles. Figure 27 is a graph of the error that is introduced into velocity measurements for a 4 MHz transducer via uncertainty in the angle of the ultrasonic probe. Figure 28 depicts the angle necessary to capture varying ranges of velocities for a 4 MHz transducer without aliasing. As a consequence of choosing a specific angle the maximum measureable depth for the ultrasound instrument is governed by the curve in figure 28. The velocity range in the water experiments is between 1.0 – 1.5 m/s. This dictates the angle that is required for the experiments. It also provides positioning limitations for the ultrasonic probe.

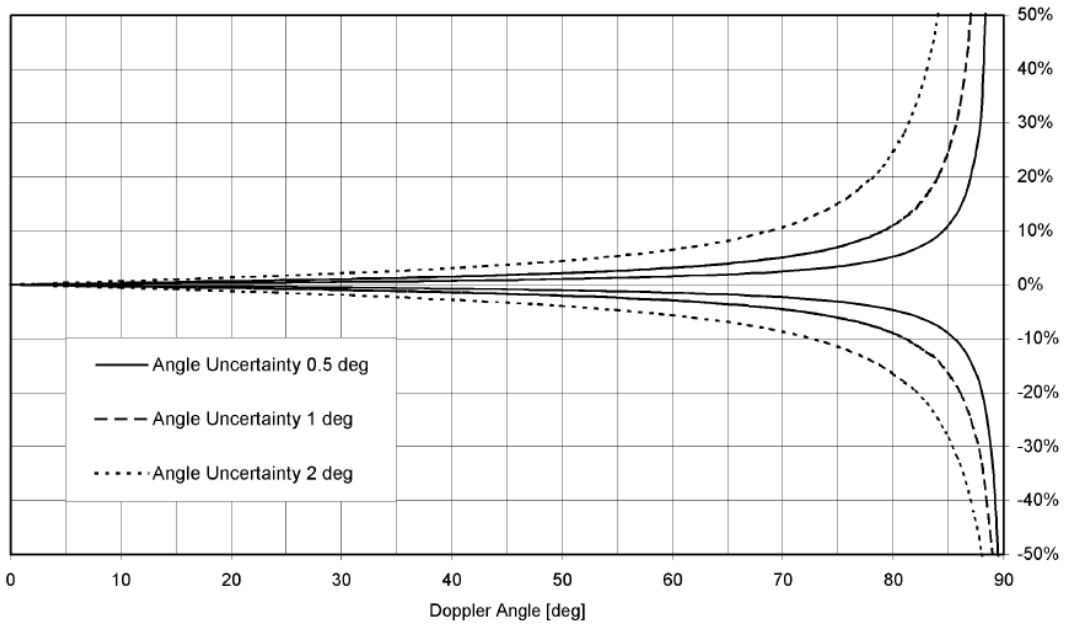

Figure 27. 4 MHz Probe Angle Uncertainty Contribution to Velocity Bias. (Geisler 2001)

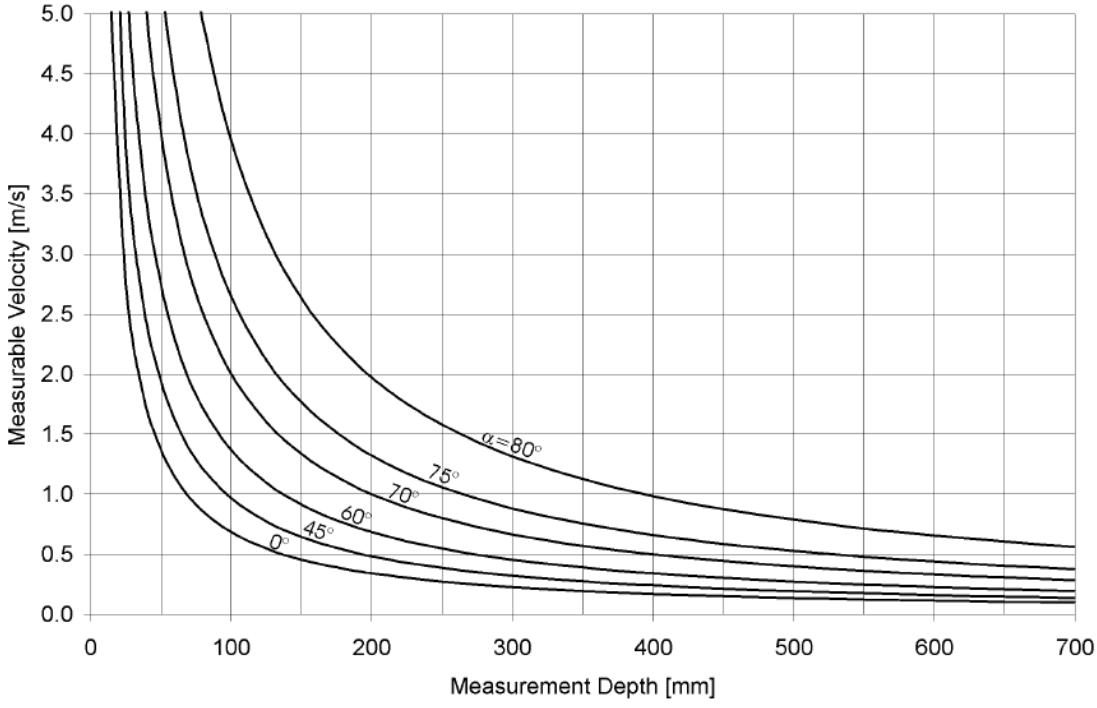

Figure 28. 4 MHz Required Angle for Flow Measurement. (Geisler 2001)

The ultrasound velocity profiler operates by emitting an ultrasound signal from the transducer in the measurement axis of the probe. The signal travels along the measurement axis and the signal interacts with a seed particle in one of three ways: Part of the energy is reflected back to the transducer, part of the energy is scattered, and the remaining energy is transmitted through the particle. If the seed particles are gaseous the sound transmission will be poor. The reflected signal returns to the transducer after a delay period t.

$$t = \frac{2x}{c} \tag{60}$$

where c is the speed of sound in the measurement medium, and x is the distance traveled. The received signal is Doppler shifted if the particle is moving along the axis of the transducer.

$$\frac{v}{c} = \frac{f_d}{2f_o} \tag{61}$$

f_d is the Doppler frequency shift, f_o is the transmitting frequency, and v is the velocity along the transducer axis. Knowledge of both the delay t and the Doppler shift allows for computation of both position and velocity of the particle.

The ultrasound monitors/collects data in discrete volumes along the measurement axis. These measurement volumes are termed channels. The GUI provides control of the channel width. The window width is defined as the total measurement region. The window width consists of multiple channels that are separated by a channel distance. The combination of these three measurement

regions define the level of detail that one can achieve/measure in the flow field. The achievable spatial resolution is defined

$$w = \frac{cn}{2f_o} = \frac{n\lambda_o}{2} \tag{62}$$

where w is the channel width and n is the number of cycles per pulse. The minimum cycles the UVP system is capable of producing is 2 cycles per pulse. The wavelength of sound produced by a 4 MHz transducer in water near room temperature is 0.37 mm. It is generally recommended that the UVP system is set to 4 cycles per pulse (claimed in the user manual). The channel distance is variable only by integer multiples of the spatial resolution. The channel distance is constant throughout the measurement window for a specific selection. There will always be 0-127 channels within the measurement window. The measurement window is defined

$$w = starting\ channel + 127 * channel\ distance \tag{63}$$

The velocity resolution is determined

$$\Delta V = \frac{V_{max}}{127} \tag{64}$$

where

$$V_{max} = \frac{c^2}{8f_o P_{max}} \tag{65}$$

P_{max} is the maximum measurable depth.

Overlapping of the measurement windows is possible if the channel distance is set smaller than the channel width. If this phenomenon occurs, the internal programming performs a spatial averaging for each channel taking into account each adjacent channel. The spatial resolution becomes dependent upon the channel width and not the channel distance. The spatial averaging smoothes the velocity profile. The raw data can be recorded independently.

Figure 29 is a diagram taken from the Metflow UVP user manual. It illustrates the spatial measurement resolution of the UVP system. Tables 9-11 provide descriptions of the maximum velocities detectable, velocity resolution, spatial resolution, and temporal resolution. Tables 9-11 encompass all of the conditions that are encountered in the present water experiments. There are 128 channels or measurement windows within the window width. In the case of

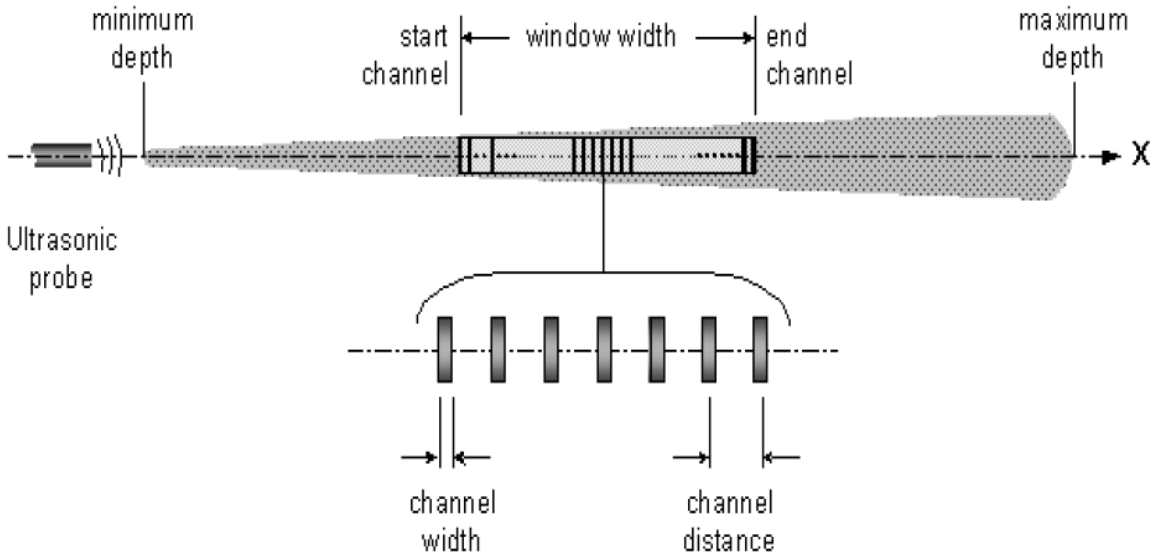

Figure 29. Ultrasonic Measurement Window. (Met-Flow 2000)

Table 9. Low Resolution, files h (high scenario).

	Nrep = 200; n = 32; *f0* = 4MHz				
Temperature *C*	18	19	~19.5	20	21
c (speed of sound) *m/s*	1476	1479	1480	1482	1485
F*prf* (pulse repetition frequency) *Hz*	6514.085	6514.085	6967.985	6514.085	6514.085
w (channel width) *m*	0.005904	0.005916	0.00592	0.005928	0.00594
Vmax *m/s*	0.600924	0.602146	0.644539	0.603367	0.604588
ΔV (velocity resolution) *m/s*	0.004732	0.004741	0.005075	0.004751	0.004761
ΔT (averaged profile measuring time) *s*	0.030703	0.030703	0.028703	0.030703	0.030703

Table 10. Medium Resolution, files m (Medium scenario).

	Nrep = 96; n = 16; *f0* = 4MHz				
Temperature *C*	18	19	~19.5	20	21
c (speed of sound) *m/s*	1476	1479	1480	1482	1485
F*prf* (pulse repetition frequency) *Hz*	6514.085	6514.085	6967.985	6514.085	6514.085
w (channel width) *m*	0.002952	0.002958	0.00296	0.002964	0.00297
Vmax *m/s*	0.600924	0.602146	0.644539	0.603367	0.604588
ΔV (velocity resolution) *m/s*	0.004732	0.004741	0.005075	0.004751	0.004761
ΔT (averaged profile measuring time) *s*	0.014737	0.014737	0.013777	0.014737	0.014737

Table 11. High Resolution, files l (low scenario).

	Nrep = 32; n = 4; *f0* = 4MHz				
Temperature *C*	18	19	~19.5	20	21
c (speed of sound) *m/s*	1476	1479	1480	1482	1485
F*prf* (pulse repetition frequency) *Hz*	6514.085	6514.085	6967.985	6514.085	6514.085
w (channel width) *m*	0.000738	0.00074	0.00074	0.000741	0.000743
Vmax *m/s*	0.600924	0.602146	0.644539	0.603367	0.604588
ΔV (velocity resolution) *m/s*	0.004732	0.004741	0.005075	0.004751	0.004761
ΔT (averaged profile measuring time) *s*	0.004912	0.004912	0.004592	0.004912	0.004912

channel overlap a smoothing function is implemented via the UVP-XW-Psi internal program. Exactly how the smoothing function is implemented remains unclear. Several runs at various resolution levels are provided for select orientations to present the differences between the application of the internal smoothing and those runs that show no overlap of channels. Additional details about individual runs are located within the data files that accompany this dissertation.

The speed of sound within the medium is important to the accuracy of calculations. The speed of sound in the fluid medium is an input that can be set at the beginning of each run. This input can only be entered in whole numbers. The speed of sound is calculated as (Lubbers 1998):

$$c = 1405.03 + 4.624 * T - 0.0383 * T^2 \quad (66)$$

where T is the absolute temperature of the fluid. During an experimental run, the fluid temperature may rise due to two factors: Energy deposited in the fluid via the 2, ½ hp pumps (745 Watts total) or a change in the room/outside temperature. All experiments were performed next to a large metal rolling door that radiates significant heat on hot days and provides a cold source during evenings. The observed change in the speed of sound differs by at most 0.6 percent. These changes are accounted for as the temperature change was detected during the course of the experiment.

In order for the output from the UVP to be of use to the validation efforts a connection between the ultrasound measurement volume and a corresponding volume within the computational domain must be established. Factors that must be considered to create a defendable link include: defining the measurement line axis, the averaging techniques used in the ultrasound processing, and the size and orientation of the measurement volume. The velocity gradient that is within the measurement volume affects the velocity average computed from echoes off particulate traveling through the volume. In the case of jets, the line of measurement traverses the cross section of the jet at an angle of 20 degrees, as shown in figure 30.

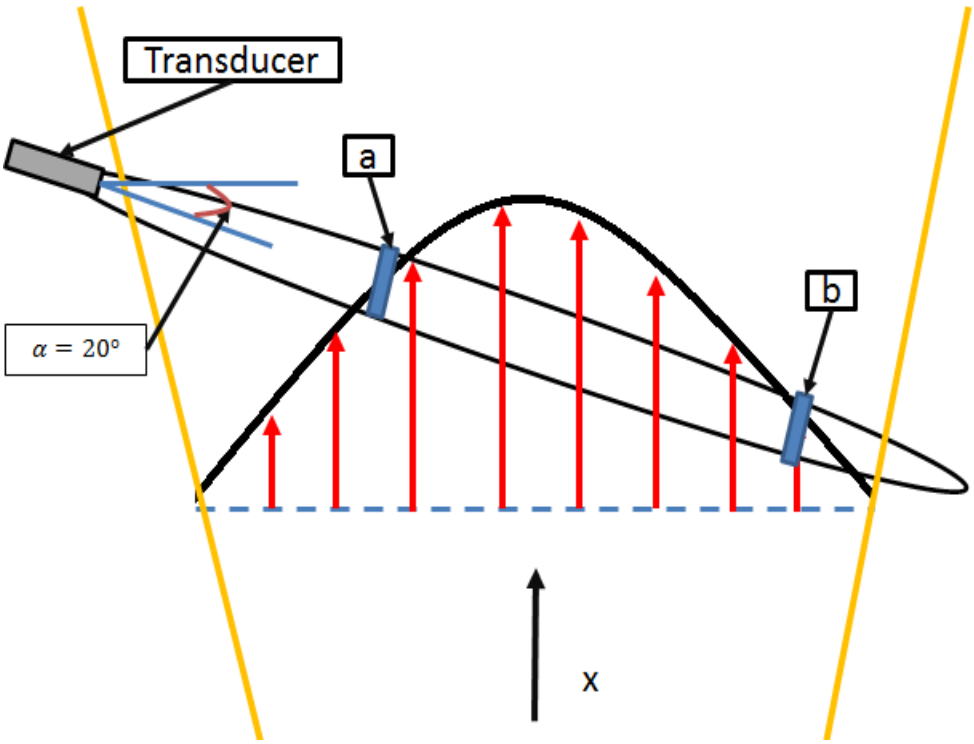

Figure 30. UVP Measurement and Jet Velocity Profile.

An angled volume entering the shear layer from a low velocity region experiences a higher velocity in the leading portion of the measurement volume, as depicted by volume *a* in figure 30. Measurements volumes exiting the shear boundary layer will experience a lower averaged velocity at the leading portion of the volume compared to the trailing edge, as depicted by volume *b* in figure 30. Additionally, the gradient within the volume will affect the outcome of the average. Depicted in figures 31-32 are two different gradients that will shift the returned value if a typical average is conducted, depending on how the average is implemented. The Metflow user's manual suggests overlapping of measurement volumes in the presences of large gradients to provide a better picture of the flow.

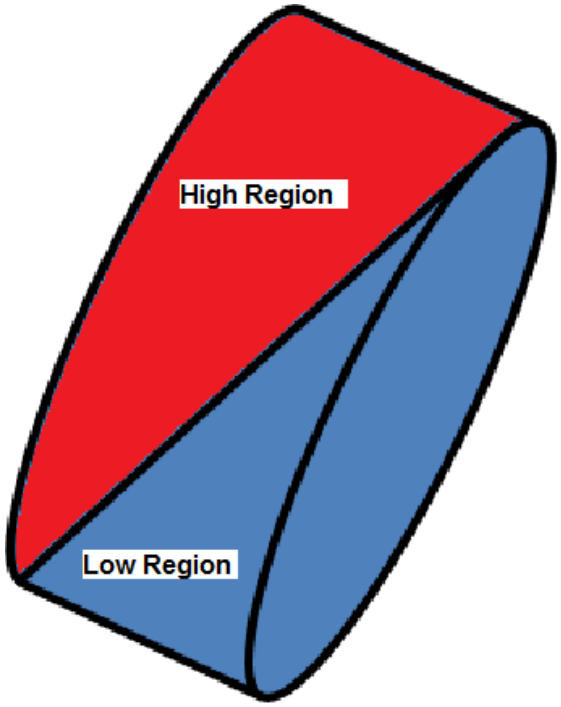

Figure 31. Averaging Scenario 1.

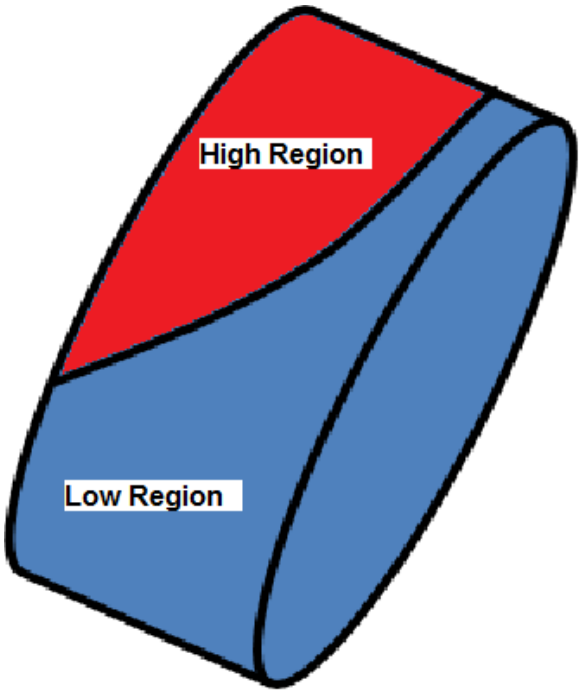

Figure 32. Averaging Scenario 2.

The location of the each volume along the measurement axis must be matched with a corresponding volume within the computational domain. The ultrasound measurement volume diverges by an amount that is dependent upon the specific transducer. This divergence must be characterized and the average values returned through the Metflow GUI must be modified to represent the expansion of the measurement volume along the measurement axis.

The spreading of the ultrasound beam can be mapped by holding the ultrasound transducer stationary and moving an object from a reference point, perpendicular to the transducer beam axis, across the beam axis. The position of the object from the reference point to where echoes are first visible on an oscilloscope is recorded. Figure 33 displays a very modest narrowing of the

beam as distance increases from the probe. It is surmised that this is a result of weak echoes that are below the noise threshold in the peripheral regions of the beam at larger distances from the probe face. Note that the gain for echo detection is elevated for channels far from the transducer face, and this can be controlled somewhat through the GUI.

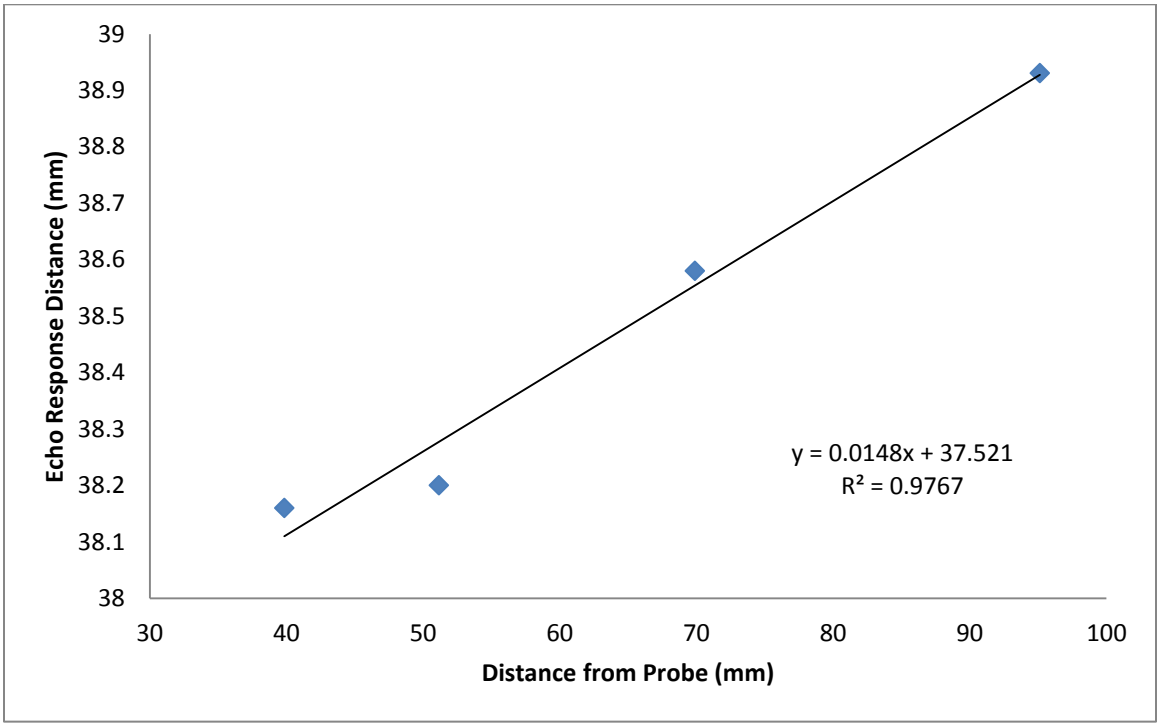

Figure 33. UVP Beam Echo Response

The ultrasound probe records echoes in a bin for each particle traversed, as shown in figure 34. Multiple particles may traverse the same measurement bin, each with unique trajectory. Echoes may be generated from anywhere within the disk, shown in figure 35. The Doppler velocity measurements in each bin are local instantaneous measurements, and these values are averaged,

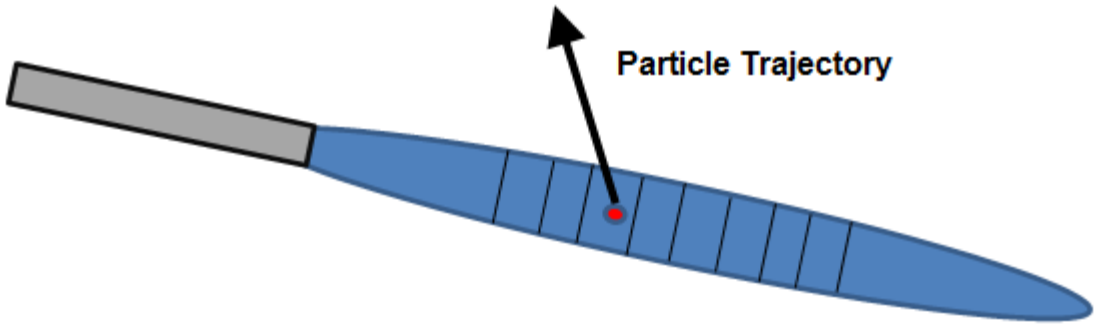

Figure 34. Particle Traveling Through the UVP Beam

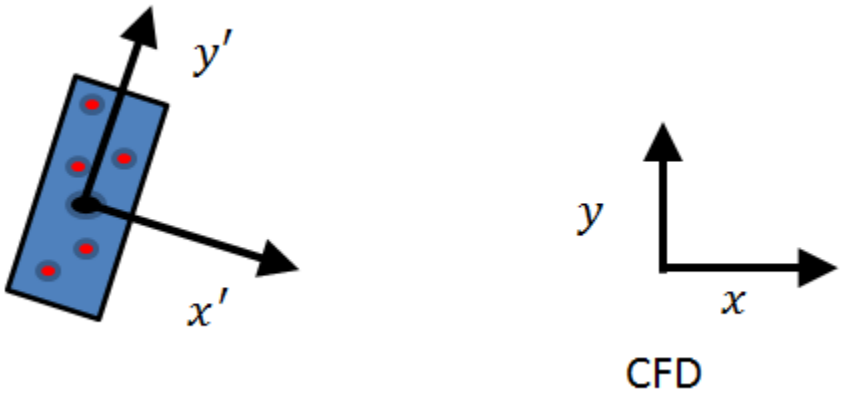

Figure 35. Particles in a Measurement Volume

$$\overline{u'} = \frac{\sum_{n=1}^{N} u'_{Doppler}}{N} \quad (67)$$

to give a time averaged Doppler velocity value. This time averaged velocity value is also from anywhere in the measurement disk where echoes return, within the time gate,

$$D - \delta < D < D + \delta \quad (68)$$

$$\delta = \frac{c\xi}{2} \tag{69}$$

where ξ is the gate width. Thus the actual returned value of velocity is also volume averaged,

$$\langle \overline{u'} \rangle = \frac{\int_T \frac{\iiint_V cu' dV}{V} dT}{T} \tag{70}$$

where $c(y')$ is a weighting function for echoes from the volume. The $c(y')$ may be plausibly represented as figure 36. Assuming the intensity of the pulse in the primary lobe is proportional to a weighting function at a location x' then the weighting function is scalable for all x'. The distribution of particle size and associated echo strength would also influence this weighting function.

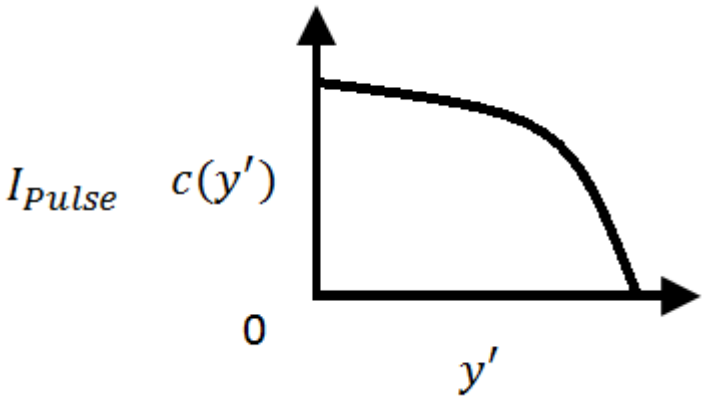

Figure 36. Possible Weighting Function

4.1 Theory of Measurements

An additional complexity in the ultrasonic measurement is associated with the measurement volume, and the discrete echoes produced within each measurement volume from particulates or small bubbles in the flow, as presented in the previous section. This section relates the measurement to the Reynolds Transport Theorem, and acknowledges that the echoes are from particles and small bubbles located somewhere in the measurement volume, providing a connection between the measurement and anticipated CFD predictions.

The ultrasound transducer emits short near critically damped pulses with a primary harmonic frequency of 4 MHz. The transducer receives echoes from particles in the primary lobe of the broadcast field of the transducer, which is normally 10 cm long, and about the width of a pencil. The shape of the transducer broadcast field is shown in figure 29. Echo producing particles pass through this volume intermittently. The ultrasound Doppler velocimeter calculates velocity values determined from the frequency shift of an echo, or a set of echoes, returned from the measurement volume. The time of the echo return relative to the pulse emission is used to determine the distance of the echo source from the transducer face,

$$D = \frac{2c}{\Delta T} \tag{71}$$

where c is the speed of sound. The echo return times are separated into 128 bins, providing 128 axial positions along the primary lobe where velocity data are collected from Doppler frequency evaluations. The UVP instrument simultaneously measures time and space averaged velocities. Most other measurement modalities are only capable of measuring time and space values sequentially. What follows is a revision of space and time averaging methods for fluid flow to bridge the UVP measurement, as described in equation 70, to the CFD prediction.

The instantaneous flow equations solved in CFD equations can be time average over an interval [T]. The interval must be chosen so that it is large compared with the turbulent fluctuations and small compared with the overall flow fluctuations so that measurements are not obfuscated. What follows is a generic development of the single time-averaged and double time-averaged fluid transport equations as developed by Delhaye (Delhaye 1981). Applying table 12 at any point in the development will yield the corresponding result for conservation of mass, linear momentum, angular momentum, total energy, or entropy, for a phase denoted by subscript k.

Table 12. Definition of Symbols Used in the Generalized Integral Balance (Re-copied from Delhaye 1981)

Balance	ψ_k	J_k	φ_k	φ_i
Mass	1	0	0	0
Linear Momentum	v_k	$-T_k$	$\boldsymbol{F}$	0
Angular Momentum	$r \times v_k$	$-T_k \cdot R^*$	$\boldsymbol{r} \times \boldsymbol{F}$	0
Total Energy	$u_k + \frac{1}{2} v_k^2$	$q_k - T_k \cdot v_k$	$F \cdot v_k$	0
Entropy	s_k	$\frac{1}{T_k} q_k$	$\frac{1}{\rho_k} \Delta_k$	Δ_i

The particle k is measured intermittently; function f_k will have the piece wise appearance shown in figure 37.The local instantaneous transport equation is integrated over the time interval [T]. [T_k] is the sum of the seed residence times in the measurement field. Subscript k can apply to the liquid phase, or the particles. We focus on the particles as the source of echoes for measurement.

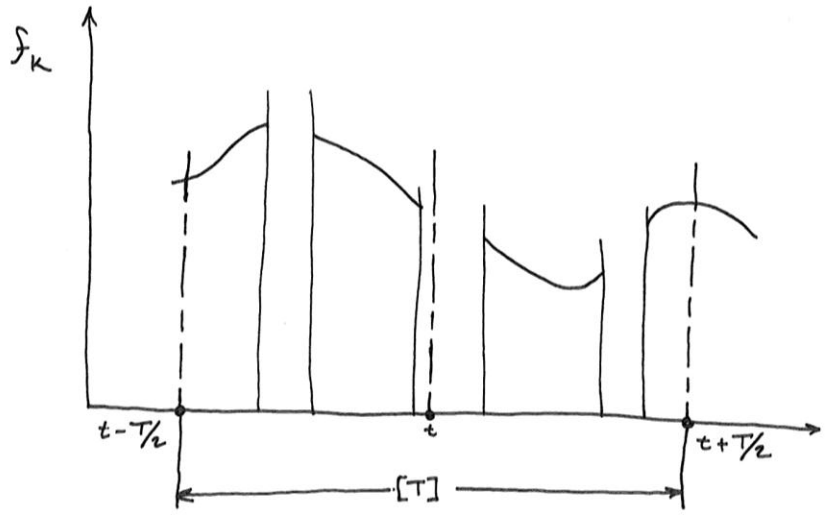

Figure 37. An Intermittent Function. (Reproduced from Delhaye 1981)

$$\int_{[T_k]} \frac{\partial}{\partial t} \rho_k \psi_k dt + \int_{[T_k]} \nabla \cdot (\rho_k \psi_k \boldsymbol{v}_k)\, dt + \int_{[T_k]} \nabla \cdot \boldsymbol{J}_k dt - \int_{[T_k]} \rho_k \varphi_k dt = 0 \tag{72}$$

The limiting form of Leibniz Theorem is

$$\int_{[T_k]} \frac{\partial f_k}{\partial t} dt = \frac{\partial}{\partial t} \int_{[T_k]} f_k dt - \sum_{disc \in [T_k]} \frac{1}{|\boldsymbol{v}_i \cdot \boldsymbol{n}_k|} f_k \boldsymbol{v}_i \cdot \boldsymbol{n}_k \tag{73}$$

Assuming f_k=1, the particle is either present or not, reduces to

$$\frac{\partial \alpha_k}{\partial t} = \frac{1}{T} \sum_{disc \in [T_k]} \frac{\boldsymbol{v}_i \cdot \boldsymbol{n}_k}{|\boldsymbol{v}_i \cdot \boldsymbol{n}_k|} \tag{74}$$

Where α_k is the residence fraction of k.

$$\alpha_k \triangleq \frac{T_k}{T} \tag{75}$$

The limiting form of the Gauss Theorems

$$\int_{[T_k]} \nabla \cdot \boldsymbol{B}_k(x,t) dt = \nabla \cdot \int_{[T_k]} \boldsymbol{B}_k(x,t) dt + \sum_{disc \in [T_k]} \frac{1}{|\boldsymbol{v}_i \cdot \boldsymbol{n}_k|} n_k \cdot \boldsymbol{B}_k(x,t) \tag{76}$$

where $\boldsymbol{B}_k$ is a general term later defined.

With the aid of Leibniz and Gauss theorems provided, the local instantaneous transport equation becomes:

$$\frac{\partial}{\partial t} \alpha_k \overline{\rho_k \psi_k}^X + \nabla \cdot \alpha_k \overline{\rho_k \psi_k v_k}^X + \nabla \cdot \alpha_k \bar{\boldsymbol{J}}_k^X - \alpha_k \overline{\rho_k \varphi_k}^X =$$

$$-\sum_j l_j^{-1} (\dot{m}_k \psi_k + \boldsymbol{J}_k \cdot n_k)_j \tag{77}$$

where $\dot{m}_k$ is the mass transfer per unit area of interface and per unit of time, associated with each phase k. The mass transfer between solid particles and the liquid is zero. l_j is defined

$$l_j \triangleq T|\boldsymbol{v}_i \cdot \boldsymbol{n}_k|_j \tag{78}$$

The local time-averaged equations for mass and momentum are offered as,

$$\frac{\partial}{\partial t}\alpha_k\overline{\rho_k}^X + +\nabla \cdot \alpha_k\overline{\rho_k \boldsymbol{v}_k}^X = -\sum_j l_j^{-1}\dot{m}_{k\,j} \tag{79}$$

$$\frac{\partial}{\partial t}\alpha_k\overline{\rho_k \boldsymbol{v}_k}^X + \nabla \cdot \alpha_k\overline{\rho_k \boldsymbol{v}_k \boldsymbol{v}_k}^X - \nabla \cdot \alpha_k\overline{T_k}^X - \nabla \cdot \alpha_k\overline{\rho_k \boldsymbol{F}}^X =$$

$$-\sum_j l_j^{-1}(\dot{m}_k \boldsymbol{v}_k + \boldsymbol{T}_k \cdot \boldsymbol{n}_k)_j \tag{80}$$

It is assumed that the function g(x,t) describing the single time-averaged operator is capable of being expanded into a Fourier series. The resulting equation can then be split into a signal and noise. It is desired that the function g(x,t) be low-pass filtered such that

$$\bar{g}(x,t) \cong g_{signal}(x,t) \tag{81}$$

$$\frac{\partial}{\partial t}\bar{g}(x,t) \cong \frac{\partial}{\partial t}g_{signal}(x,t) \tag{82}$$

If these conditions are not met a double time-averaging operator is needed. Delhaye and Achard have shown that these conditions are not always met. The flow structure may have time and space scales smaller than measurement time

intervals, or measurement volume leading to discontinuous $\frac{\partial}{\partial t}\bar{g}(x,t)$.The first derivative with respect to time is satisfied by

$$\overline{\overline{f_k}^X} \triangleq \frac{1}{T}\int_{t-T/2}^{t+T/2}\left(\frac{1}{T_k}\int_{[T_k]} f_k d\eta\right) d\tau \tag{83}$$

where $\bar{\bar{f}}^X$ is the double time-average operator. The new Leibniz and Gauss Theorems are

$$\overline{\overline{X_k \frac{\partial f_k}{\partial t}}} = \frac{\partial}{\partial t}\overline{\overline{X_k f_k}} - \sum_j L_j^{-1}(f_k v_i \cdot n_k)_j \tag{84}$$

$$\overline{\overline{X_k \nabla \cdot \boldsymbol{B}_k}} = \nabla \cdot \overline{\overline{X_k \boldsymbol{B}_k}} + \sum_j L_j^{-1}(\boldsymbol{n}_k \cdot \boldsymbol{B}_k)_j \tag{85}$$

These theorems are employed to develop the double time-average transport equation:

$$\frac{\partial}{\partial t}\beta_k \overline{\overline{\rho_k \psi_k}}^X + \nabla \cdot \beta_k \overline{\overline{\rho_k \psi_k \boldsymbol{v}_k}}^X + \nabla \cdot \beta_k \bar{\bar{\boldsymbol{J}}}_k^X - \beta_k \overline{\overline{\rho_k \varphi_k}}^X =$$

$$-\sum_j l_j^{-1}(\dot{m}_k \psi_k + \boldsymbol{J}_k \cdot n_k)_j \tag{86}$$

Development of the complete picture of the test section requires the use of composite equations that either: average local time-averaged equations over the measurement channel cross-section or average over a time interval the instantaneous equations that have been averaged over the measurement channel cross-section.

The development of this comprehensive picture of the flow in the measurement channel cross-section requires that the time averaged transport equations be averaged spatially. This results in a composite-averaged transport equation. From the averaging operator definition

$$\prec \alpha_k \overline{f_k}^{X} \succ = \prec \overline{X_k f_k} \succ \triangleq \frac{1}{\boldsymbol{a}} \int_a \left(\frac{1}{T} \int_{[T]} X_k f_k dt \right) d\boldsymbol{a} \tag{87}$$

the following results

$$\prec \alpha_k \overline{f_k}^{X} \succ_2 \equiv \overline{R_{k_2} < f_k >_2} \tag{88}$$

this combines the time average operation with the spatial average operation. R_{k_2} is the area fraction of k in a specific cross-section.

$$R_{k_2} \triangleq \frac{\boldsymbol{a_k}}{\boldsymbol{a}} \tag{89}$$

Equation 88 can be generalized for any dimension

$$\prec \alpha_k \overline{f_k}^{X} \succ_n \equiv \overline{R_{k_n} < f_k >_n} \tag{90}$$

In order to connect the interfacial area to the speed of interface displacement, it is convenient to examine the confined flow, figure 38. The speed of interface displacement is what the UVP measures. The particle k is moving through the measurement volume defined by a' and a'', separated by distance Z. The interfacial area at a position within the volume is defined by $a_i(t)$.

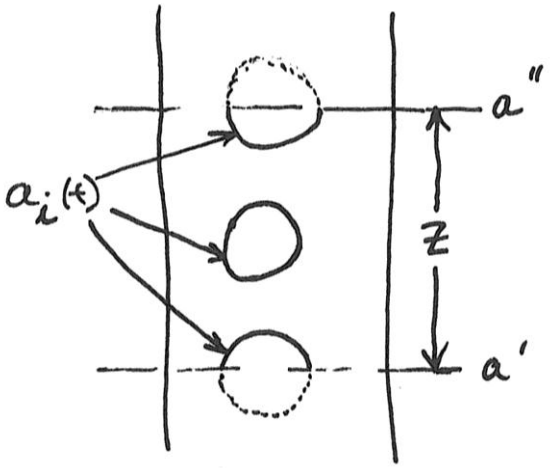

Figure 38. Time Dependent Interfacial Area. (Reproduced from Delhaye 1981)

The following identity is satisfied for an arbitrary vector field $\boldsymbol{B}_k(x,t)$

$$\int_V \left[\sum_j l_j^{-1}(\boldsymbol{B}_k \cdot \boldsymbol{n}_k)_j\right] dV \equiv \overline{\int_{a_\iota(t)} \boldsymbol{B}_k \cdot \boldsymbol{n}_k d\boldsymbol{a}} \tag{91}$$

$$l_j \triangleq T|\boldsymbol{v}_i \cdot \boldsymbol{n}_k|_j \tag{92}$$

where T is the integration period and $v_i \cdot n_k$ is the speed of the interfacial area displacement at instant i. Choosing the vector field B_k to represent the interface normals

$$\boldsymbol{B}_k \equiv \boldsymbol{n}_k \tag{93}$$

yields the relation between interfacial area and speed of interface displacement.

$$\int_V \left(\sum_j l_j^{-1}\right) dV \equiv \overline{\boldsymbol{a}_\iota(t)} \tag{94}$$

adding definitions of local specific area $\gamma(x)$ defined on period $[T]$ and the integral specific area $\Gamma_3(\mathrm{t})$ instantaneously defined for volume V

$$\gamma(\boldsymbol{x}) \triangleq \sum_j l_j^{-1} \tag{95}$$

$$\Gamma_3(\mathrm{t}) \triangleq \frac{\mathbf{a}_\mathrm{i}(\mathrm{t})}{\mathrm{V}} \tag{96}$$

a link is established between integral specific area and local specific area.

$$\lessdot \gamma(x) \gtrdot_3 \equiv \overline{\Gamma_3(\mathrm{t})} \tag{97}$$

As the height Z of the volume shrinks towards zero, a link between interaction terms in the time-space averaged equations emerges (that is equally valid for space-time averages).

$$\lessdot \sum_j l_j^{-1}(\boldsymbol{B}_k \cdot \boldsymbol{n}_k)_j \gtrdot_2 \equiv \frac{1}{a}\overline{\int_\varsigma \boldsymbol{B}_k \cdot \boldsymbol{n}_k \frac{d\varsigma}{\boldsymbol{n}_k \cdot \boldsymbol{n}_{k\varsigma}}} \tag{98}$$

The total cross-sectional area average of the local time-averaged equation yields

$$\frac{\partial}{\partial t} \lessdot \alpha_k \overline{\rho_k \psi_k}^X \gtrdot_2 + \frac{\partial}{\partial z} \lessdot \alpha_k \overline{\boldsymbol{n}_z \cdot (\rho_k \psi_k \boldsymbol{v}_k)}^X \gtrdot_2 + \frac{\partial}{\partial z} \lessdot \alpha_k \boldsymbol{n}_z \cdot \bar{\boldsymbol{J}}_k^X \gtrdot_2 - \lessdot$$
$$\alpha_k \overline{\rho_k \varphi_k}^X \gtrdot_2 = -\lessdot \sum_j l_j^{-1} (\dot{m}_k \psi_k + \boldsymbol{J}_k \cdot \boldsymbol{n}_k)_j \gtrdot_2 - \int_{\varsigma_1+\varsigma_2} \alpha_k \boldsymbol{n}_k \cdot \bar{\boldsymbol{J}}_k^X \frac{d\varsigma}{\boldsymbol{n}_k \cdot \boldsymbol{n}_{k\varsigma}} \tag{99}$$

The UVP measures the velocity component of individual particles, along the beam axis, that traverses a measurement volume. The UVP is measuring the velocity of the interfacial area of the seed particles. During an acquisition time window, the velocities related to recorded echoes specific to a spatial window are

averaged. Possibly, the average performed is weighted within the measurement volume as previously discussed. Each measurement volume is then assigned an average velocity value that is averaged spatially (across the volume) and time averaged (measurement window for each measurement volume), similar to equation 70. Equation 99 relates to conservation of mass by inserting the values of table 12

$$\frac{\partial}{\partial t} \prec \alpha_k \overline{\rho_k \psi_k}^X \succ_2 + \frac{\partial}{\partial z} \prec \alpha_k \overline{n_z \cdot (\rho_k \psi_k \boldsymbol{v}_k)}^X \succ_2 = - \prec \sum_j l_j^{-1} \left(\dot{m}_k \psi_k\right)_j \succ_2 \qquad (100)$$

Equation 100 is the appropriate interpretation of the measured UVP velocity values. The mass transfer term, $\dot{m}_k$, is zero for solid particles. It is important to note that prior to substituting values of table 12 into equation 99 for the momentum and energy equations, care must be taken when performing the square of the velocity and cube of the velocity. The average of squares is not equal to the square of averages. It would be wise to perform the square of a term prior to any step that averages that result.

CHAPTER 5

SIMULATIONS

5.0 Water Simulations

CFD simulations were performed early in the research (2009) to help guide the design of experiments. Characterizing the velocity field of the jets, including the regions where gradients are steep, was important to properly scale the experiments to accommodate the limitations of the ultrasonic measurement modality. This effort is presented here because the CFD simulations produce velocity fields. These predicted velocity fields are not like any of the legacy data presented in the literature review. The velocity fields predicted by the CFD are like the measured data presented in the following chapters. These simulations do not directly reflect the measured velocity fields that follow because the size of the WTF was enlarged after these early simulations were performed. CFD simulations of the WTF flow field are underway at ANL.

The multiphysics code COMSOL version 3.4 was used for CFD simulations. Single jet and twin jet simulations were performed. The single jet simulations served as a rudimentary qualification of the COMSOL code for applicability to free shear flow phenomena relevant to the physics of a jet impinging vertically into a stagnant fluid of identical fluid. The twin jet simulations served as a guide to the design of test facilities and instrumentation placement decisions. Prior to employing COMSOL in this manner, the capability of

COMSOL to reproduce vetted data for a single vertical water jet injected into a pool of water was explored. The code performance was not great, but was adequate to guide design. Other more advanced CFD tools were not available due delays in progress of other program team participants.

COMSOL is a commercially available finite element equation solver, capable of solving partial differential equations. It is built on the MATLAB programing language. The COMSOL graphical user interface is elaborate. Several types of boundary conditions, solver options, and meshing options are available to the simulator. COMSOL integrates numerous physics through the use of modules. It employs basic Reynolds Averaged Navier Stokes (RANS) turbulence models and also includes forced and natural convection models.

The COMSOL k-epsilon and k-omega models were employed for turbulence modeling in the jet simulations. The k-epsilon and k-omega models are two-equation turbulence models that allow the velocity and length scales of a turbulent flow to be determined. Rodi indicates that the k-epsilon model can be used to model free shear flows. However, two constants, C_μ and $C_{\varepsilon 2}$, should be modified to improve agreement with experimental results (Rodi 1984). The constant associated with the COMSOL k-omega model that is modified from its default value is C_μ. The list of pertinent k-epsilon and k-omega constants used in the COMSOL simulations are displayed in table 13. $C_{\varepsilon 1}$ is the Dissipation rate equation production coefficient, $C_{\varepsilon 2}$ is the dissipation rate equation dissipation coefficient, C_μ is the eddy viscosity coefficient, $\alpha_{closure}$ is a closure coefficient, β_0

is a closure coefficient, β_{0k} is a closure coefficient, σ_k is the turbulent Prandtl number for kinetic energy, σ_ω is the turbulent Prandtl number for the specific dissipation rate, and σ_ε is the turbulent Prandtl number for dissipation rate.

Table 13. K-ε and K-ω Constants. (L. Tschaepe 2010)

k-ω		k-ε	
α closure	0.53	C_ε1	1.44
β 0 closure	0.072	C_ε2	1.8533
β 0k closure	0.09	σ_k	1
σ_k	0.5	σ_ε	1.3
σ_ω	0.5	C_μ	0.05
C_μ	0.05	turbulent kinetic energy	0.005
turbulent length scale	0.01	turbulent dissipation rate	0.005
turbulence intensity	0.05		

The simulation geometry shown in figure 39 for the water validation closely mimics the experimental setup used by Tokuhiro (Tokuhiro 1999). The main difference is the simulation employs a reduced test section height. A heat transfer module, describing the fluid properties, is used in addition to the stated turbulence models for each of the simulations. The cases presented are isothermal simulations. Inclusion of the heat transfer module allows for the evaluation of the material properties over a temperature range and eliminates the need to manually input material properties. Figure 39 displays the pertinent boundary conditions that are applied for the isotropic single water jet injected vertically into a pool of water. Employment of two modeling modules requires two boundary conditions at each boundary, excluding continuity boundaries. For all walls, the wall offset in viscous units is 1000. This assumes that the flow near the walls is of little concern and should be valid as long as the jet does not

directly impact the walls. The assumption that the simulated jet flow field does not impact the wall is visually verifiable through COMSOL post processing menus. To satisfy the heat transfer module at the walls, the boundary condition is chosen to be thermal insulation. The flow inlet boundary conditions prescribe the velocity as 0.5 m/s and the inlet temperature as 293.15 K. The outlet boundary conditions prescribed are zero pressure and convective flux. Figure 40 displays the mesh density at the outlet used in the simulation for the single water jet. It was determined, through iterations, that an increased mesh density at the flow outlet is beneficial to the conservation of mass. The total number of elements and degrees of freedom in the k-epsilon simulation are 7236 and 63469, respectively. The total number of elements and degrees of freedom in the k-omega simulations are 9576 and 97731. A stationary segregated iterative solver is used for the present simulations. The employed segregated solver breaks the opportunity into three groups consisting of velocity and pressure components, log(d) and log(k) for the k-epsilon solver (log(w) and log(k) for the k-omega solver), and Tf and Jf. Each group uses a Direct (PARDISO) solver and iterates until the solution converges below 1E-3.

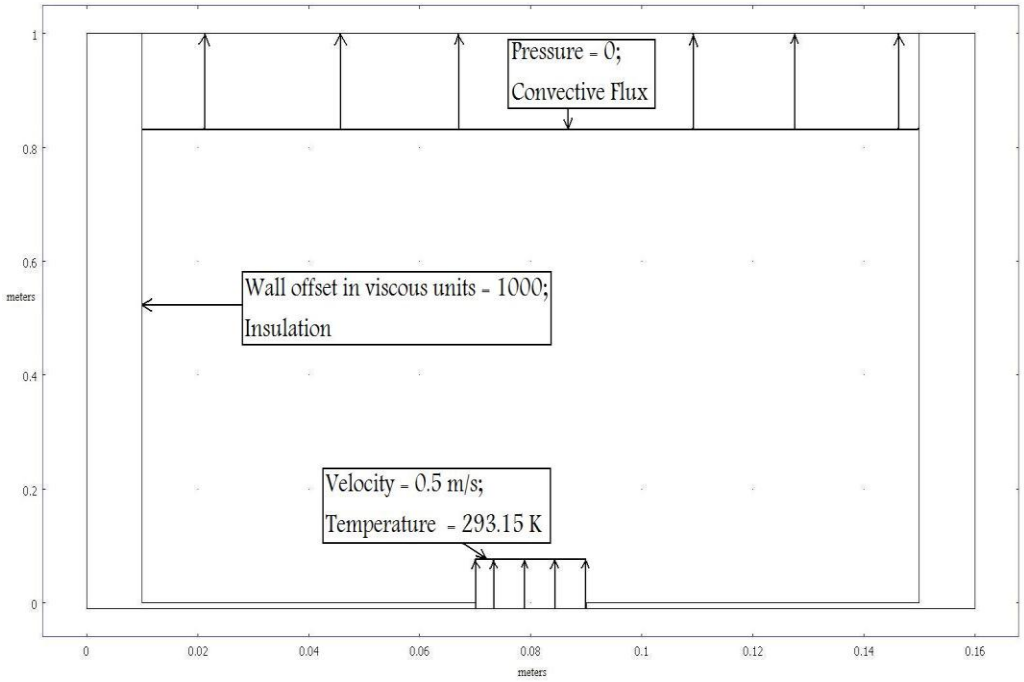

Figure 39. Single Jet Boundary Conditions. (L. Tschaepe 2010)

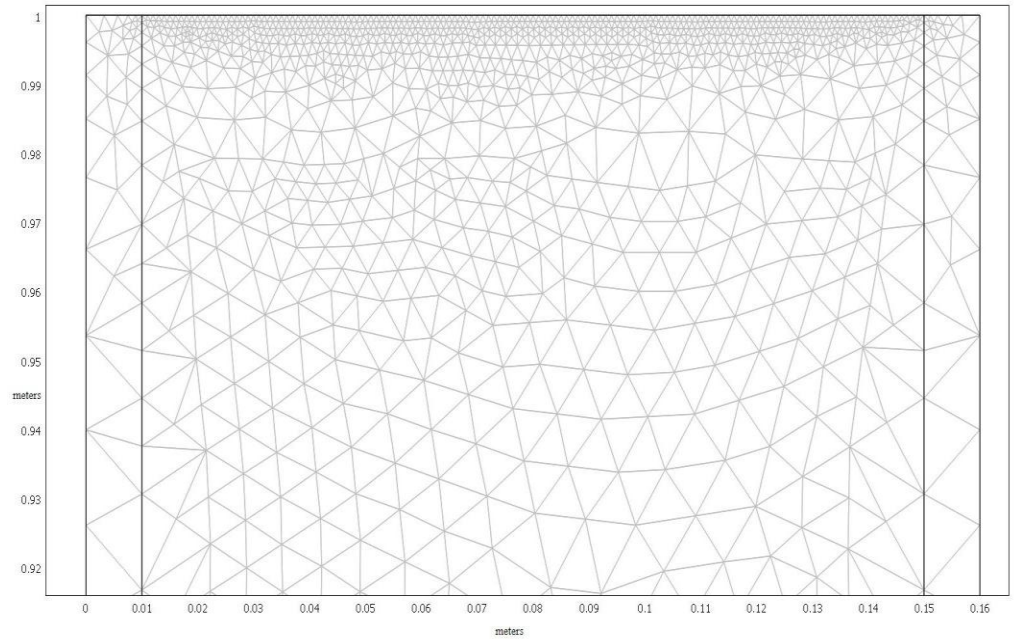

Figure 40. Single Jet Mesh Density. (L. Tschaepe 2010)

Prior to comparing the COMSOL simulations to experimental results, the simulations are juxtaposed with theoretically determined mass and momentum balances. The integral transport equation is:

$$\frac{d}{dt}\iiint \rho c dV + \oiint \rho c(\vec{v})\vec{n}dA = \iiint \rho\varphi dV + \oiint \vec{J}\vec{n}dA \quad (101)$$

where c = 1, $\vec{J} = 0$, and $\varphi = 0$ yields mass conservation. It is assumed for all conservation analysis that the solution is at steady state, and the fluid is incompressible. Applied to the COMSOL mesh and geometry in figure 40, the mass conservation

$$v_{out} = \frac{v_{in}A_{in}}{A_{out}} \quad (102)$$

returns an outlet velocity of 0.0714285714 m/s. The COMSOL predicted outlet velocity for the k-omega simulation is 0.0715714286 m/s. The mass flow errors for the k-epsilon and k-omega simulations are 0.8% and 0.2%, respectively.

The integral momentum balance is represented by equation 100 with $c = \vec{v}$, $\vec{J} = \bar{\bar{\tau}} - p\bar{\bar{I}}$, and $\varphi = \vec{g}$. Applying these new constraints to equation 100 and neglecting viscous effects yields:

$$p_{in} = \frac{\rho g}{A_{out}}[hA_{out} + v_{in}^2 A_{in}] \quad (103)$$

The outlet boundary is assumed to be maintained at 0 Pa. The calculated inlet pressure is 10170.4543 Pa. The k-epsilon and k-omega simulated inlet

pressures are 9923.95975 Pa and 9964.2331 Pa, respectively. The resulting errors for the k-epsilon and k-omega simulations are 2.4% and 2%. These variations from the theoretical results can potentially be attributed to a coarse mesh.

Figure 41-42 are comparisons of the COMSOL k-epsilon and k-omega models to existing literature data for the decay of the centerline velocity versus axial distance and the half radius half max. It is apparent that the COMSOL k-epsilon model show reasonable agreement with these data. The COMSOL k-epsilon simulation results in a slightly non-linear decay of the centerline velocity. However, the COMSOL k-epsilon simulation results remain bounded by previous experimental results for methane, air, and water. The jet half radius comparison shows that the COMSOL k-epsilon simulation predicts a slope which mimics the historical data. These results lend confidence to the COMSOL k-epsilon simulations. The k-omega results do not perform well under the applied conditions. It significantly over predicts the decay of the centerline velocity and the slope of the k-omega velocity prediction in figure 41 is much steeper than prior experimental results. The k-omega predicted jet half radius is also inconsistent with prior experimental results. The poor performance of the k-omega may be due to overzealous diffusion parameters used to obtain a stable solution for the k-omega simulation. Unless significant improvement can be made, the k-omega model as implemented in COMSOL will not be used for the future development of the mercury and sodium separate effects facilities.

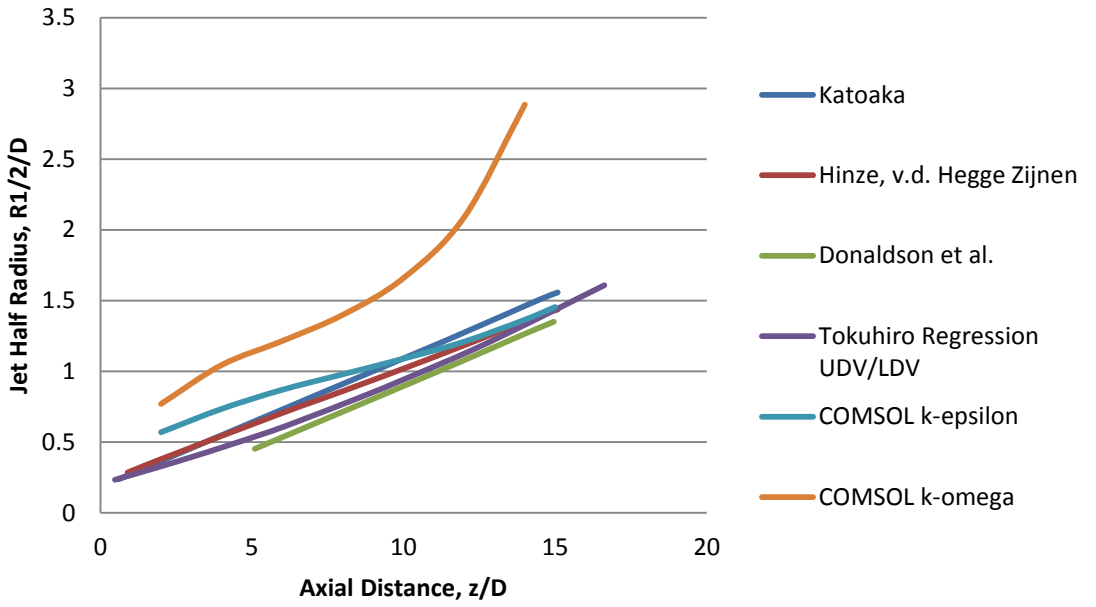

Figure 41. Decay of the Centerline Velocity versus Axial Distance. (L. Tschaepe 2010)

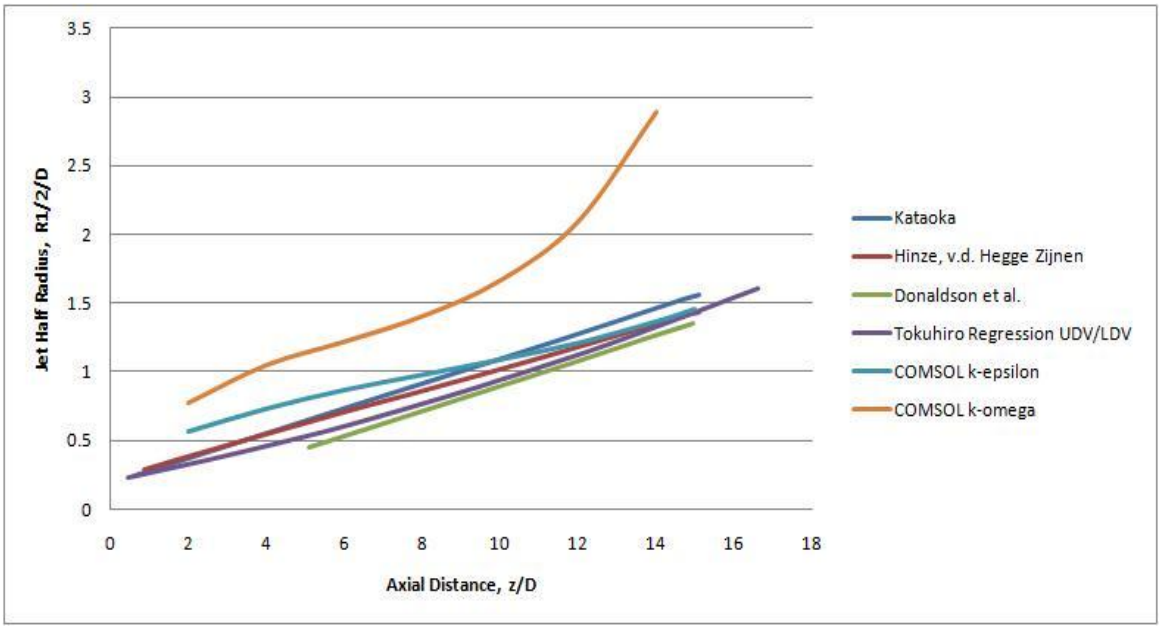

Figure 42. Jet Half Radii versus Axial Distance. (L. Tschaepe 2010)

5.1 Liquid Metal Simulations

The premise of the experimental setup is that two vertical jets will be combining under free turbulence and will be uninfluenced by wall effects. For the experiments of interest, the temporal fluctuations of the measured quanta, temperature and velocity, are likely large where the jets first combine. Temporal fluctuations will be smaller further away from the jet inlets. CFD methods employing LES models, or DNS methods, can reproduce both temporal and spatial attributes of the mixing jets. The capability to measure and to model these fluctuations are of interest to CFD validation efforts. While COMSOL using RANS models will not deliver time resolved turbulence outcomes, these simulations are still quite useful to the early design effort.

Based on jet theory and historical experiments (in non-liquid metals) for a single round jet: The mean velocity profile does not become self similar until x/D > 20. The stream wise velocity fluctuations become self similar at x/D = 50, and the transverse velocity fluctuation components become self similar at x/D = 70. It is at this point that the singular jet is considered to have reached a self preserving state. The presented two jet simulations assume an x/D = 160.

The inlet diameter of each jet is 0.00635 m. The mercury flow rate is 2 L/min. This flow rate results in a jet inlet velocity of 0.526 m/s for mercury at 293 K. To effectively relate the momentum simulations between the investigated fluids, they are examined at equal Reynolds numbers. The multiphysics code COMSOL is used to simulate theoretical outcomes for the mercury test section.

The results for the COMSOL k-epsilon and k-omega velocity fields are presented in figure 43. Figure 43 are velocity simulations of isothermal mercury twin jet flows. It is apparent that, as currently implemented, there are significant differences between the k-epsilon and k-omega results.

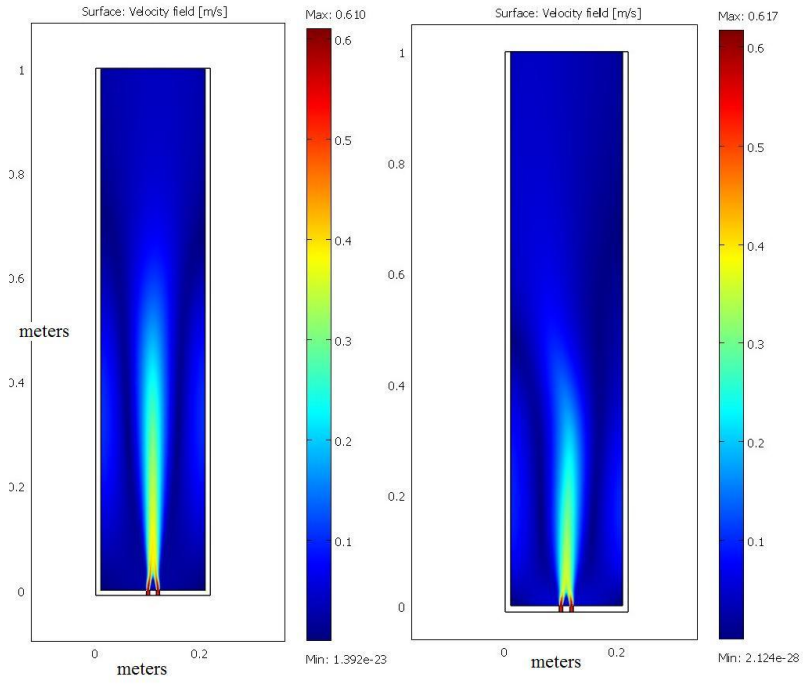

Figure 43. k-epsilon (left) and k-omega (right) Simulations of Mercury Velocity Profile. (L. Tschaepe 2010)

Similar to the water validation, analytic mass and momentum balances are performed to determine, to the extent possible, the validity of the simulations. The theoretical and simulated solutions for the mass and momentum balances are compared in table 14. Error reported in table 14 is defined as theory minus COMSOL divided by theory. Mesh refinement forces the simulation towards the theoretical solution. Equation 104 is calculates the reported error.

$$error = \left|\frac{analytic - simulation}{analytic}\right| \quad (104)$$

Table 14. Mass and Momentum Comparisons. (L. Tschaepe 2010)

Mercury				
Solutions	Exit Velocity	Error	Inlet Pressure	Error
analytic	0.033401		132996.3642	
k-ε	0.034155	0.02257	134857.5293	0.013994
k-ω	0.03379	0.01165	135030.8849	0.015298

COMSOL is used to guide the design of an experimental facility for gathering high resolution data for mixing of two liquid metal jets. The default settings provided by COMSOL serve as a starting point for jet simulation, with the k-epsilon model providing reasonable fidelity to legacy data for single jet flows. The k-omega model appears to be too diffusive using the recommended settings. The likely primary intent of the COMSOL developers was the implementation of turbulence models for wall bounded flows.

Going forward, the high resolution data from the two jet mixing experiments, including time resolved temperature and velocity variation statistics, will allow a more complete validation of turbulence models for flow simulations. More advanced turbulence modeling approaches, such as LES, will benefit from the more comprehensive validation data.

CHAPTER 6

SINGLE JET EXPERIMENT AND DATA

The first sets of experiments presented are for a single jet. The single jet experiments are included in the suite of validation data due to the additional historical reference which the experimental results can be compared. Each experimental facility is unique and as a result the data from these experiments are not directly comparable to previous experiments. The WTF is elevated slightly at the handles to force all return flow to the first header tank, as shown in figure 23. Specifics of the elevation were not measured or recorded but the inclination is no more than 3 degrees. A graphical description of the single jet experiments is provided in figure 44. The remaining figures are provided in appendix A. The darkened region serves as indication that the second jet is not operating. The S-Jet label corresponds to the orientation of the ultrasound probe for the data acquisition in the sjetXX_by_channel file series. The data obtained in all experiments is publically accessible and is categorized via the delineated file protocol. The data accompanies this dissertation through a file system provided by the University of Tennessee. Data are acquired along the direction of the arrow. The sjetXX_by_channel file series is located within the Single Jet folder. The C-Jet corresponds to the orientation of the ultrasound probe for the data acquisition in the cjetXX_by_channel file series. Data is acquired along the direction of the arrow. The cjetXX_by_channel file series is located within the Single Jet folder. The provided MATLAB script (located within the Single Jet

folder) imports into MATLAB the name_by_channel.txt files and sorts them into unique arrays. If an individual file is called, then all of the raw data associated with the run is accessed. Note: the MATLAB path must be set to the location of the .txt files. The MATLAB code for importing and sorting the data is provided in appendix B. The y-coordinate and z-coordinate are explicitly defined in figure 44. The x-coordinate is out of the page. The same coordinate system is used in all experiments.

Figures 45-46 are pictures of two separate dye injection runs for single jet experiments. Figure 45 is taken from the left side of the WTF and figure 46 is taken from the right side of the WTF, as defined in figure 44. The same jet is in operation for each picture. Figure 45 is operating at a Reynolds number that is higher than figure 46, on the order of 1E4. The development of the potential core within the high Reynolds flow is clearly discernible in figure 45.

The intermittency of the shear layer is easily detectable within the low Reynolds flow, figure 45. Figures 47-48 are the average velocities and the standard deviations for the cjet_by_channel file series. Figures 49-50 are the average velocities and the standard deviations for the sjet_by_channel file series. The velocity profiles of the cjet files heuristically appear to be correct. The color scales at the right of the figures depict the intensity of the velocity and standard deviation. The velocities are reported in units of m/s. Fluctuations exist in the corners of the reported fields. The only data processing of the raw data is due to

the conversion from the Doppler shifted frequency to the projection of the velocity component in the direction of the jet axis.

It is apparent from the figure 51 that there is a small shift in the bin number that records the peak centerline position. An explanation for the walking of the maximum in the velocity profile may be in the test facility physical orientation. Bottle jacks are used to level the test facility. Single jet experiments are conducted by raising one end of the tank to allow use of one weir. In the experiment presented, the bottle jacks on the handle side are raised. This action forces all of the return to flow over the opposing weir. It also changes the boundary condition placed on the facility. The change of the boundary condition could potentially lead to a shear gradient on the handle side of the single jet. This may “tilt” the jet towards the return weir.

The recorded flow rate for the single jet experiments is 10 gpm. Accounting for the jet exit cross section (8.8 cm by 0.6 cm), the mean jet velocity at exit should be 119.4 cm/s. Where the mean velocity is defined as the total volume flow rate divided by the jet cross sectional area. It is apparent from the presented graphs that the UVP is measuring velocity values in excess of the mean supplied velocity.

The difference between the supplied and measured velocity prompted a rerun of the cjet experiments to insure that the recorded flow rate for the single jet experiments are correct. Three sets of measurements are recorded for each

measurement height. The file nomenclature is hcjetX, mcjetX, lcjetX. The first letter in the file “h, m, l” corresponds to the level of spatial and temporal resolution. h indicates a high spatial and temporal resolution, m indicates a mid-level spatial and temporal resolution, and l represents a low spatial and temporal resolution. Specifics of the spatial and temporal resolution for each run are in table 15.

Table 15. Testing Conditions Synopsis

	Nrep = 32; n = 4; *f0* = 4MHz, “h-files”	Nrep = 96; n = 16; f0 = 4MHz, “m-files”	Nrep = 200; n = 32; f0 = 4MHz, “l-files”
Temperature *C*	16.4	16.4	16.4
c (speed of sound) *m/s*	1471	1471	1471
F*prf* (pulse repetition frequency) *Hz*	6967.9849	6967.9849	6967.9849
w *m*	0.0007355	0.002942	0.005884
Vmax *m/s*	0.640619112	0.640619112	0.640619112
ΔV (velocity resolution) *m/s*	0.005044245	0.005044245	0.005044245
ΔT (averaged profile measuring time) *s*	0.004592432	0.013777297	0.028702703

Figures 52-55 are comparisons of the high, medium, and low resolution measurements at the 3rd, 6th, 17th, and 21st elevations. The corresponding height above the jet inlet is noted in the figure captions. The probe is located on the left side of these graphs. The measured values leading into the jet active region are similar for the first two profiles presented. The results for the three

measurement resolutions differ for the receding edge of the jet, in the first two profiles. However, the medium and low resolution profiles match well for the final two profiles presented. No conclusions can be offered as to which of the results is closer to a true value, because an alternative measurement modality (PIV, hotwire anemometry, etc.) was not available. It can be noted that the high resolution measurements deliver lower velocities, compared to the medium and low resolution measurements.

Surface plots of the average velocities and standard deviations are provided for the high, medium, and low resolution measurements in figures 56-61. The first 5-7 bins of these profiles experience aberrant signals and they should be discounted when evaluating results. It is apparent that the results of the repeated experiment closely mimic the original experiments.

Figure 62 indicates a slight rise in the velocity across the length of the jet (sjet files). This may indicate that there is a slight parabolic velocity profile at the jet outlet and indicate that the jet center velocity should be elevated, compared to a uniform velocity assumption. This would be caused by a friction factor that varies across the channel length or by an exit form factor that varies across the jet exit. These are phenomena to be examined using CFD. An option for reducing the variation in the velocity profile across the length of the jet is to modify the jet inlet.

One of the goals of this project is the development of data sets suitable for verification and validation. A cog in that effort is the post processing of the data so that it can be compared to simulation outcomes. Figure 63 illustrates the geometric arrangement of the measurements. The transducer is set at an angle of 20 degrees with respect to the axis perpendicular to the primary direction of flow. A transformation from the measurement coordinate system to a coordinate system conducive to the simulation environment is needed. Equations 105 and 106 provide the required transformation.

$$\hat{\imath}' = \hat{\imath}\cos 20 + \hat{\jmath}\sin 20 \quad (105)$$

$$\hat{\jmath}' = \hat{\jmath}\cos 20 + \hat{\imath}\sin 20 \quad (106)$$

The transformation is completed by setting x,y and x',y' equal to zero at a specified point. As a result of the small angle required for the experiments the measured component of the velocity in the direction of the flow is small. This is a result of the cosine of the probe angle. Less than 10 percent of the velocity in the x-direction is actually captured by the UVP Doppler measurement. Note that flow velocity normal to the jet axis is nearly collinear with the transducer, and 94 percent of those velocities are captured by the UVP Doppler measurement.

Figure 64 is a graph of the maximum measured velocity divided by the maximum predicted supplied velocity. This velocity ratio is plotted against X/D where D is the width of the jet outlet (0.6 cm) and X is the vertical position of the ultrasound transducer. The X position is not the same as the location of the

maximum bin. The difference between X and the real X is due to the 20 degree angle of the probe. For all measurements, the actual bin position is below X.

The steep drop in the velocity profiles of figure 62 indicate the surrounding fluid that is provided to the jet flow as entrainment. The fluid is being drawn into the jet in a direction normal to the jet axis, the direction along which the UVP is most nearly aligned. The small flow velocity away from the probe face likely is as important as the growing flow in the direction of the jet flow in the shear layer, leading to zero and occasionally negative velocity measurements. This layer of fluid is just outside of the free shear layer. The velocity trough appears to remain located to the same 3-4 bin region of measurements (discounting the first 3 runs). CFD post processing could reproduce the velocity the probe should be measuring.

Ignoring the first 20 bins in the sjet file series outside the jet core, the maximum velocity of each measurement level appears at or near the end of the velocity profile. Figure 65 is a graph of the maximum measured velocity divided by the mean predicted supplied velocity. This velocity ratio is plotted against X/D where D is the width of the jet outlet (0.6 cm) and X is the vertical position of the ultrasound transducer. This profile is similar to the profile presented for the cjet file series.

Figures 66-74 are velocity profiles at three closely spaced intervals for a single jet. High, medium, and low resolution measurements are performed at

each level. The ultrasound probe for these measurements is set to 90 degrees (parallel with the y-axis). The measured velocities are only the component of the flow in the y-direction. Measurements are recorded for opposing sides of the jet. It is apparent from the figures that the flow from the jet is asymmetric. The flow on the boundary nearest the handle is elevated compared to the receding side. The orientation of the probe is based on figure 44. This further corroborates the observed movement in the peak jet centerline velocity.

Several single jet experiments were performed and selected results are provided. It is important to note that each element of the grid displayed in the MATLAB outputs contain data points. The single jet was mapped at various positions as indicated in figure 44. Data measurements were recorded for various resolutions of the UVP. Differences between the various UVP GUI settings are visible on the overlapped profiles. It is apparent that the jet is reasonably uniform. The decay of the center line velocity is also mapped. Based on the literature review the results of these experiments are consistent with expectations.

CHAPTER 7

DUAL JET EXPERIMENTS AND DATA

The next sets of experiments presented are for dual parallel mixing jets. These experiments serve as a foundational piece of the NEUP funding grant objectives. A graphical description of the dual jet experiments is provided in figure 75. Data files corresponding to the labels provided in figure 75 are acquired along the direction of the arrows. In addition to the arrows labeled 0-6, data is acquired 180 degrees to these arrows with a start position on the jet furthest from the handle. The files corresponding to the left and right of the jet are located in the *Left and Right of Dual Jet Centerline* folder. Three types of files exist within these folders: *hjetX_by_channel*, *mjetX_by_channel*, and *ljetX_by_channel*. The *h*, *m*, and *l* correspond to the scenarios depicted in tables 9-11. The *X* in the file name relates to the run and the elevation of the probe. The elevation is correlated to the run number in the accompanying Excel file. The files corresponding to the 0-6 labels are located in the *Dual* Jet folder. The subfolders reference the position of the probe. The *Dual Jet Near Handle* references those files that correlate to the arrows drawn in figure 75 and the *Dual Jet Far Handle* correlates to those files that are 180 degrees to the arrows shown in figure 75. The provided MATLAB script (located within the respective dual jet folder) imports into MATLAB the *name_by_channel.txt* files and sorts them into unique arrays. If an individual file is called, then all of the raw data associated with the run is accessed. Note: the MATLAB path must be set to the location of the *.txt*

files. The y-coordinate and z-coordinate are explicitly defined in figure 75. The x-coordinate is out of the page. The same coordinate system is used in all experiments.

The average velocities and standard deviations for the scenarios depicted in tables 9-11 are provided in figures 76-93. The high, medium, and low scenarios are evaluated for the left and for the right sides to determine if there is uniformity in the measurements and if the jets provide uniform flow. Figures 82-84 are single channel velocity profiles from the left side, extracted from the high, medium and low resolution velocity profiles. These profiles provide a direct comparison between different spatial and temporal resolutions at varying levels. It is again evident that the high resolution measurements predict velocities that are below the medium and low resolution measurements. Also, the velocity values measured via medium and low resolution are similar. Figures 91-93 are velocity profiles from the right side of the jets. These profiles indicate similar trends to those recorded from the left side of the jets.

Figures 94-107 compare the high scenario to the low scenario for measurements 0-6 in the near handle position. The figures appear in pairs with the high scenario first and the low scenario second. The high spatial resolution data were taken to a height of 400 mm. While, the lower resolution/spatially averaged data extends to a height of 500 mm.

Several dual jet experiments were performed and selected results are provided. It is important to note that each element of the grid displayed in the MATLAB outputs contain data points. The dual jets were mapped at various positions as indicated in figure 75. Data measurements were recorded for various resolutions of the UVP. UVP GUI settings causing overlapped profiles produce velocity values different from measurements using other GUI settings.

CHAPTER 8

CONCLUSIONS AND FUTURE WORK

8.0 Conclusions

This Nuclear Energy University Program (NEUP) funded research intended in part to quantify the relationship between data from experiments and multi-physics simulations. This included a review of the current state of verification and validation standards (S. Peters et al. 2011), and a review of the ASME standard for experimental data treatment (ASME 19.1). Demands of the data used for validation escalate as the complexity of multi-physics simulations escalates. Even within the relatively well circumscribed situation of a single jet emerging in a quiescent pool, or of two jets of unequal temperature mixing, the demands to coordinate experiment design, data collection and CFD modeling activities in order to achieve a meaningful validation of the CFD simulation are quite formidable.

Mixing of twin parallel jets is of interest to Liquid metal reactor design. Liquid metal fast reactor (LMFR) coolant enters the bottom of the fuel bundles and exits through the top of the bundle. Spatial power variation in the core fuel bundles causes variation in bundle exit flow temperatures. The flow exiting the bundles must mix in the upper plenum of the reactor, prior to exiting through the hot leg of the reactor. Incomplete mixing can lead to unacceptable thermal stresses in the hot leg piping. The physics governing the flow exiting fuel bundles

into the upper plenum resembles the flow physics in interacting parallel jets. Consequently, the parallel jet geometry is of interest to liquid metal reactor design, and data from this research will be useful to validation of CFD codes used in liquid metal reactor design and simulation.

Prior literature on single jets and mixing jets is reviewed and preliminary simulations of jet mixing in a pool were conducted using COMSOL to inform the design of these experiments. Subsequent to these studies, a water test facility capable of measuring velocity and temperature profiles in jets to X/D > 100 was designed, built, and operated. The facility is flexible, allowing jet inlet flow geometries to be changed, and either one or two jets can be operated. The individual jets are supplied from individual header tanks so that jets of different temperature, conductivity, or color can be introduced for mixing studies. The facility is transparent, and capable of gathering data via Particle Image Velocimetry (PIV) as well as UVP. The jet inlet geometry and flow conditions are easily modified. The velocity field for single and dual jets was mapped using ultrasonic velocimetry in the WTF for this dissertation. Prior work by Peters 2010 mapped the thermal profiles of mixing jets of dissimilar temperature, with Reynolds numbers similar to those used for the velocity studies.

The velocity data presented herein are collected in a tight spatial matrix, and include statistics on velocity variation. The jet inlet flow is fully developed, providing well quantified boundary/inlet condition for CFD simulation. These are improvements over much of the legacy data.

The connection of the ultrasonic Doppler fluid velocity data to the governing equations for flow is developed herein. This transformation is an important component of validation data. The ultrasonic instrument measures Doppler shift in echoes from particulates and bubbles in the fluid. These echoes may return from anywhere in the measurement volume, as defined by the time gate for returns and the diameter of the active zone of the transducer. The Reynolds transport equation for the particulate flow is used to develop the transformation between the measured velocities and associated measurement volume, particle size distribution, and temporal averaging. These transformations are required to relate the velocity values measured to predicted values from a CFD simulation. However, the understanding of the measurement volume and echo response remains incomplete. Further experimentation to quantify the response of the Ultrasonic Doppler velocimeter is required to improve the fidelity of the transformation of the measured velocities to the actual flow attributes. A second measurement modality, such as Particle Image Velocimetry (PIV) or particle tracking could be used to corroborate the UVP data in water. This effort is planned, and will be very useful prior to movement to opaque fluids such as mercury and sodium.

The uncertainty in measurement position and in water sound speed, which contributes to ultrasonically determined velocity uncertainty, is quantified. The study of the connection of the velocity data to multi-physics computational outcomes remain for others to assess.

8.1 Future Work

Going forward, the WTF may be used for thermal stratification studies, or other fluid mixing experiments. Such experimental campaigns would support the broader goal of V&V of computational methods, and allow further refinement of the connection between data and simulation outcomes required to perform Validation, and generate confidence intervals and uncertainties for simulation outcomes. These relatively simple cases offer significant challenges, and help educate us regarding the practical limits of our validation competence.

Other experiments in mercury and sodium are being planned. The mercury experiments at UTK will have Reynolds number and jet thickness identical to the WTF. The width and height of the mercury test section will be reduced, relative to the WTF, due to inventory constraints. Matching the Reynolds numbers between the WTF and the mercury experiments will require the velocity of the mercury flows to be lower. A slightly larger probe angle is possible in the mercury experiments since the jet velocities are slower and the speed of sound in mercury is similar to water. Corroboration of the water data obtained using ultrasonic Doppler methods in the WTF is planned using Particle Image Velocimetry (PIV) or particle tracking instrumentation in collaboration with Texas A&M. The optical velocity data in WTF will help establish Ultrasonic Velocity Profiler GUI settings best suited to velocity measurements in mercury and sodium.

The most useful data for CFD validation is time and space correlated multivariate data. Almost all measurement approaches fall short of this capability, but optical particle tracking while simultaneously measuring temperature variations with thermocouples of fast time response could move us closer to this goal in the WTF.

LIST OF REFERENCES

Abramovich, G. N., *Theory of Turbulent Jets*. The M.I.T. Press, (1963).

Albertson, M. L., Y. B. Dai, R. A. Jensen, and H. House, “Diffusion of Submerged Jets,” Proc. Am. SOC. *Cioil* Engrs., 74, 1751 (1948).

Anderson, E. A. and Spall, R. E., “Experimental and Numerical Investigation of Two-Dimensional Parallel Jets.” 123, 401-406, (2001).

Anderson E.A., Snyder D.O., and Christensen J., “Periodic Flow Between Low Aspect Ratio Parallel Jets.” ASME J Fluids Eng 125:389–392, (2003).

B.E. Boyack, I. Catton, R.B. Duffey, P. Griffith, K.R. Katsma, G.S. Lellouche, S. Levy, U.S. Rohatgi, G.E. Wilson, W. Wulff, N. Zuber. J. *An Overview of the Code Scaling, Applicability and Uncertainty Evaluation Methodology*, Nuclear Engineering and Design, Vol 119, No. 1, pp. 1-16, (1990).

Best Practice Guidelines for the Use of CFD in Nuclear Safety Applications, Committee on the safety of nuclear installations, NEA/CSNI/R(2007)5. (2007).

Binnie, A. M., “The Turbulent Spreading of a Water Jet,” Engineering, June, 503-504 (1942).

Cleeves, V. and L. M. K. Boelter, “Isothermal and Nonisothermal Air Jet Investigations,” Chem. Eng. Progr., 43, No. 3,123 (1947).

Cleve, K., “Die Wirkungsweise von Wirbelluftduesen,” Feuerungstechnik, 25, 317 (1937).

Corrsin, S., “Investigation of Flow in an Axially Symmetrical Heated Jet of Air,” NACA ACR (declassified) Dec., (1943).

Corrsin, S. and Uberoi, M. S., “Further Experiments on the Flow and Heat Transfer in a Heated Turbulent Air Jet,” NACA TN 1865, (1949).

Cosner, R. R, Oberkarmf, W. L., Rumsey, C.L., Rahaim, C.P. and Shih, T.I., *AIAA Committee on Standards for Computational Fluid Dynamic: status and plan*, AIAA 2006-0889. (2006).

Delhaye, J. M. and Achard, J. L., “On the Use of Averaging Operators in Two-Phase Flow Modeling,” in Thermal and Hydraulic Aspects of Nuclear Reactor Safety, vol. 1: Light Water Reactors, eds. O. C. Jones and S. G. Bankoff, pp. 289-332, ASME, New York, (1977).

Delhaye, J. M. and Achard, J. L., “On the Averaging Operators Introduced in Two-Phase Flow Modeling in Transient Two-Phase Flow,” Proc. CSNI Specialists Meet., Aug. 3 and 4, 1976, Toronto, eds. S. Banerjee and K. R. Weaver, vol. 1, pp. 5-84, AECL (1978).

Delhaye, J. M., Giot, M., and Reithmuller, M. L., *Thermohydraulics of Two-Phase Systems for Industrial Design and Nuclear Engineering*. pp. 159-186. Hemisphere Publishing Corporation, (1981).

Donald, M. B. and H. Singer, “Entrainment in Turbulent Fluid Jets,” Trans. Inst. Chem. Engrs., 37,255 (1959).

Donaldson, C. duP., Gray, A. E., “Theoretical and Experimental Investigation of the Compressible Free Mixing of Two Dissimilar Gases,” AIAA J., 4, pp. 2017-2025 (1966).

Fossett, H., and L. E. Prosser, “The Application of Free Jets to the Mixing of Fluids in Bulk,” *J. Inst.* Mech. Engrs., 160, No. 2, 224 (1949).

Förthmann, E., Über turbulente Strahlausbreitung. Ingr., -Archiv., V, 1, (1934).

Frisch, U., “Fully Developed Turbulence and Intermittency.” Annals of the New York Academy of Sciences, 357: 359–367. doi: 10.1111/j.1749-6632.1980.tb29703.x, (1980).

Geisler, Thomas., “Ultrasonic Velocity Profile Measurements in Experimental Hydraulics.”Graz University of Technology, Austria. June (2001).

Görtler, H., “Berechnung von Aufgaben der freien Turbulenz auf Grund eines neuen Naherungsansatzes,” ZAMM, 22, 5, (1942).

Guide for the Verification and Validation of Computational Fluid Dynamics Simulation, AIAA G-077-1998, American institute of Aeronautics and Astronautics, (1998).

Guidelines for Substantiating a Fire Model for a Given Application, Society of Fire Protection Engineering, Draft for Comments, 2009, Final publication in (2011).

Hinze, J. O., Van der Hegge Zijnen, B. G., "Transfer of Heat and Matter in the Turbulent Mixing Zone of an Axially Symmetrical Jet," Appl. Sci. Res., A1, 435 (1949).

NDT Resource Center, http://www.ndt-ed.org/EducationResources/CommunityCollege/Ultrasonics/EquipmentTrans/characteristicspt.htm Retrieved January 10 (2011).

J.H. Rushton, "The Axial Velocity of a Submerged Axially Symmetrical Fluid Jet," AIChE J., vol. 26 (6), pp. 1038–41. (1980).

Kataoka, K., "Modeling turbulent jets with variable density," in *Encyclopedia of Fluid Mechanics, Dynamics of Single-Fluid Flows and Mixing*, (Cheremisinoff, N. P., Ed.), Vol. 2, Chap. 20, Gulf Publ., Houston, USA, (1986).

Kimura, N., M. Nishimura, and H. Kamide, "Study of Convective Mixing for Thermal Striping Phenomena (Experimental Analyses on Mixing Process in Parallel Triple-Jet and Comparisons Between Numerical Methods)." JSME Int. J., Ser. B, 45, 3, Special Issue Int. Conf. Power and Energy Sys., p. 592, (2002).

Kolmogorov, A. N., “The Local Structure of Turbulence in Incompressible Viscous Fluid for Very Large Reynolds Number.” C. R. (Dokl.) Acad. Sci. URSS 30: 301; also Sov. Phys. Usp. 10: 734. (1941).

Kraichnan, R. H., “Inertial Ranges in Two-Dimensional Turbulence.” Phys. Fluids 10: 1417, (1967).

Kuethe, A., “Investigation of the Turbulent Mixing Regions Formed by Jets,” J. Appl. Mech., 11,3, A, 87 (1935).

Lin, Y. F. and Sheu, M. J., ”Interaction of Parallel Turbulent Plane Jets,” AIAA J., 29, pp. 1372-1373. (1991)

L. Tschaepe, et al., “Computational Fluid Dynamic Simulations of Jet Momentum Transport in Liquid Metals.” NUTHOS-8, Shanghai, China, October 10-14, (2010).

Lubbers, J. and Graaff, R., “A Simple and Accurate Formula for the Sound Velocity in Water.” Ultrasound in Medicine and Biology, Vol. 24, No. 7, pp 1065-1068. (1998).

Mandelbrot, B. B., In Turbulence and Navier-Stokes Equation, Lecture Notes in Mathematics, Vol. 565. R. Temam, Ed.: 121. Springer-Verlag. New York. (1976).

McElroy, G. E., “Effect of Size and Shape of Pipe and of Adjacent Walls on Velocity and Entrainment Ratios, Part 11, Air Flow at Discharge of Fan-Pipe Lines in Mines,” U. S. Dept. of Interior, Bureau of Mines, Nov., (1943).

Met-Flow SA, *UVP Monitor User guide*. Lausanne, Switzerland, (2000).

Miller, D. R. and Comings, E. W., “Force Momentum Fields in a Dual-Jet Flow,” J. Fluid MEch., 7, p. 237. (1960).

Murai, K., Taga, M., and Akagawa, K., “An Experimental Study on Confluence of Two Two-dimensional Jets,” Bulletin of the JSME, Vol. 19, No. 134, pp. 958-964. (1976).

Nasr, A. and Lai, J. C. S., “Comparison of Flow Characteristics in the Near Field of Two Parallel Plane Jets and an Offset Plane Jet,” Phys. Fluids, 9, No. 10, Oct, pp. 2919-2931. (1997).

Nishimura, M., Tokuhiro, A., N. Kimura, and H. Kamide, “Numerical Study on Mixing of Oscillating Quasi-Planar Jets with low Reynolds Number Turbulent Stress and Heat Flux Equation Models.” Nucl. Eng. and Design, 200 (1), 77, (2000).

Nottage, H. B., J. G. Slaby and W. P. Gojsza, “Isothermal Ventilation- Jet Fundamentals,” Heating, Piping, and Air Cond., 24-1, 165 (Jan., 1952).

Prandtl, L., “Bemerkung zur Theories der freien Turbulenz,” ZAMM, 22, 5, (1942).

Prandtl, L., “Bericht über Untersuchungen zur ausgebildeten Turbulenz.” ZAMM, 5, 136, (1925).

Predvoditelev, A. and E. Stupotshenko, “A Contribution to the Problem of the Decay of a Gas Jet Discharging from a Pipe,” Moscow Therm. Tech. *Inst.* received April 25, (1936).

Reichardt, H., “Gesetzmässigkeiten der freien Turbulenz,” VDI-Forschungsh., 414, (1951).

Rodi, W. Turbulence Models and Their Application in Hydraulics, Brookfield, Brookfield, Vt. (1984).

Ruden, P., “Turbulente Ausbreitungsvorgange im Freistrahl,” Naturwiss, 21, 21-23, 375 (1933).

S. Peters, L. Tschaepe, B. Zhang, and A. Ruggles, “V&V Methodology Comparisons: AIAA G-077(1998), ASME V&V 20 (2009), ASTM E1355-05a (2005), NEA/CSNI/R(2007), and NRC CSAU(1998)”, NURETH-14, Ontario, Toronto, September 25-30, (2011).

S. Peters. “Thermocouple Temperature Measurements for Twin Jet Thermal Mixing.” Thesis. University of Tennessee. (2011).

Standard Guide for Evaluating the Predictive Capability of Deterministic Fire Models. ASTM std. E1355-05a*,* ASTM. (2005).

Standard for Verification and Validation in Computational Fluid Dynamics and Heat Transfer, ASME V&V 20-2008, American Society of Mechanical Engineers, (2008).

Tanaka, E., "The Interference of Two-Dimensional Parallel Jets (1st Report, Experiments on Dual Jet)," Bull. JSME, 13, No. 56, pp. 272-280. (1970)

Tanaka, E., ''The Interference of Two-Dimensional Parallel Jets (2nd Report, Experiments on the Combined Flow of Dual Jet),'' Bull. JSME, **17,** No. 109, p. 920. (1974).

Taylor, G. I., "The Transport of Vorticity and Heat Through Fluids in Turbulent Motion," Proc. Roy. Soc., (London), A, 135, 828, 685, (Appendix by A. Fage and V. M. Falkner.) (1932).

Tennekes, H. and Lumley J., "A First Course in Turbulence." MIT Press. Cambridge, Massachusetts. (1972).

Test Uncertainty, ASME PTC19.1-2005, American Society of Mechanical Engineers, (2005).

The Plastics Distributor and Fabricator. http://www.plasticsmag.com/features.asp?fIssue=Nov/Dec-00 Retrieved Nov. 21, (2011).

Tokuhiro, A. “Experimental Investigation of a Vertical Planar Jet by Ultrasound and Laser Doppler Velocimetry”, Journal of Nuclear Science and Technology, Vol. 36, No. 6, p. 540-548. June (1999).

Trüpel, T., “Über die Einwirkung eines Luftstrahles auf die umgebende Luft,” Zeitschrift für das gesammte Turbinenwesen, 5-6. (1915).

Tuve, G. L., and G. B. Priester, “The Control of Air-Streams in Large Spaces,” Transactions, ASHVE, 50, 153 (1944).

Verification & Validation of Selected Fire Models for Nuclear Power Plant Applications, NUREG-1824, U.S. NRC with the Electric Power Research Institute (EPRI) and National Institute of Standards and Technology (NIST), (2007).

Voorheis, T. S., “Entrainment of Air by Axially Symmetrical Gas Jets,” Master of Science thesis, Calif., Berkeley (1939).

Zimm, W., “Uber die Stromungsvorgange in freien Luftstrahl, Forsch. Febiete Zngenieurw., 234 (1921).

APPENDIX A: FIGURES 44 THROUGH 107 (DATA)

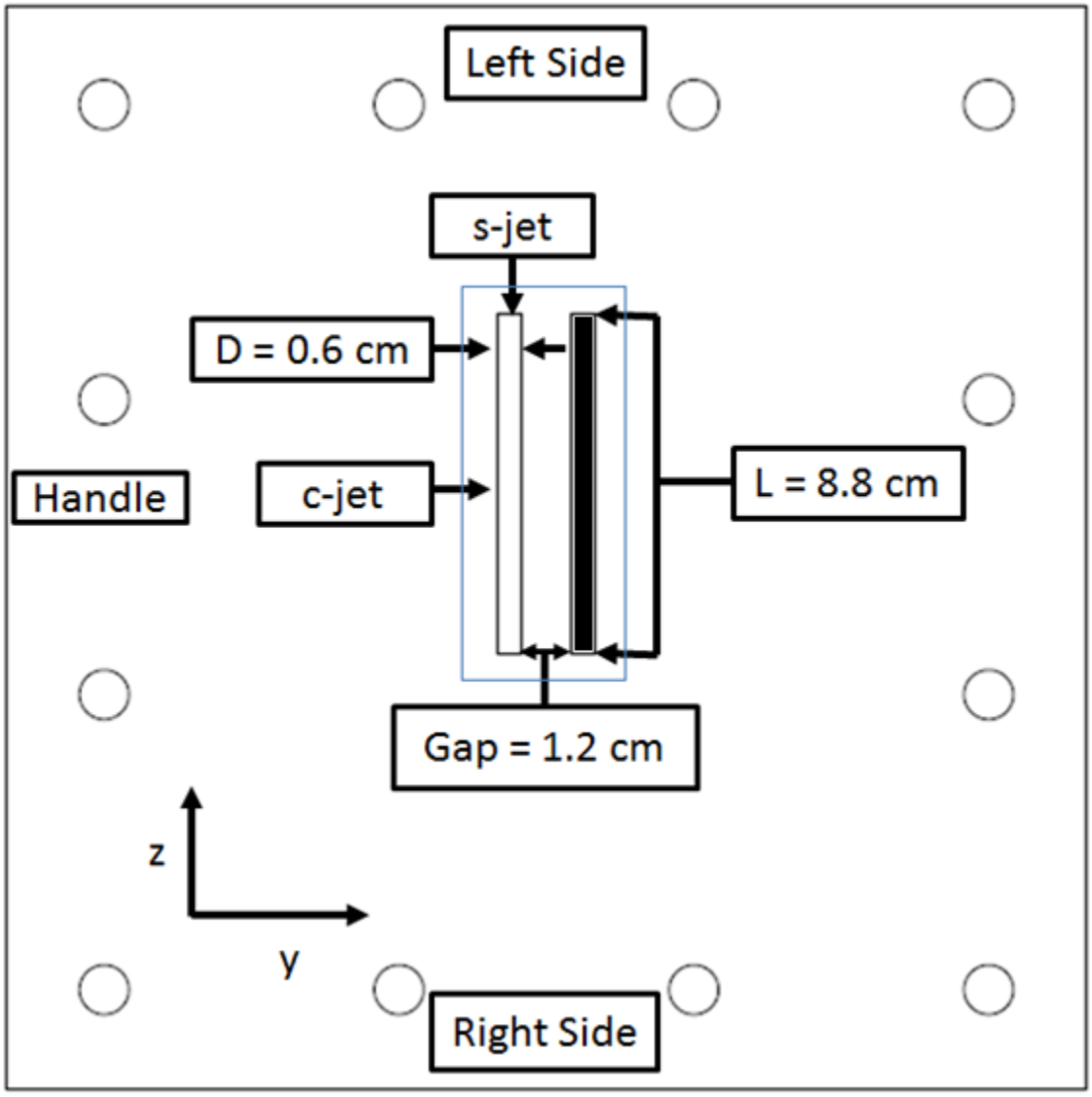

Figure 44. Single Jet Data Orientation.

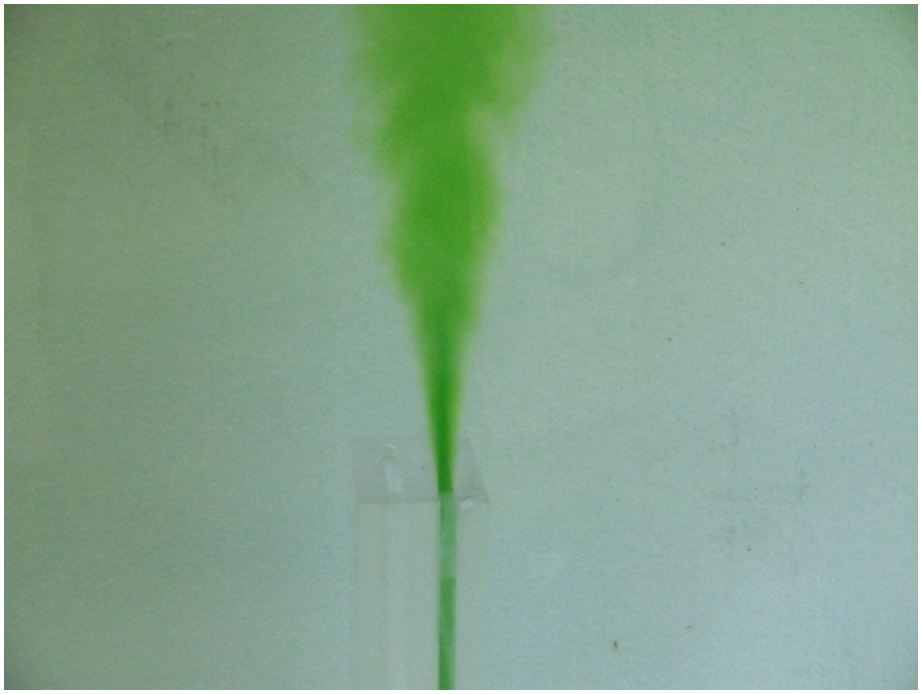

Figure 45. Dye Injection for a Single Jet Experiment High Reynolds Number.

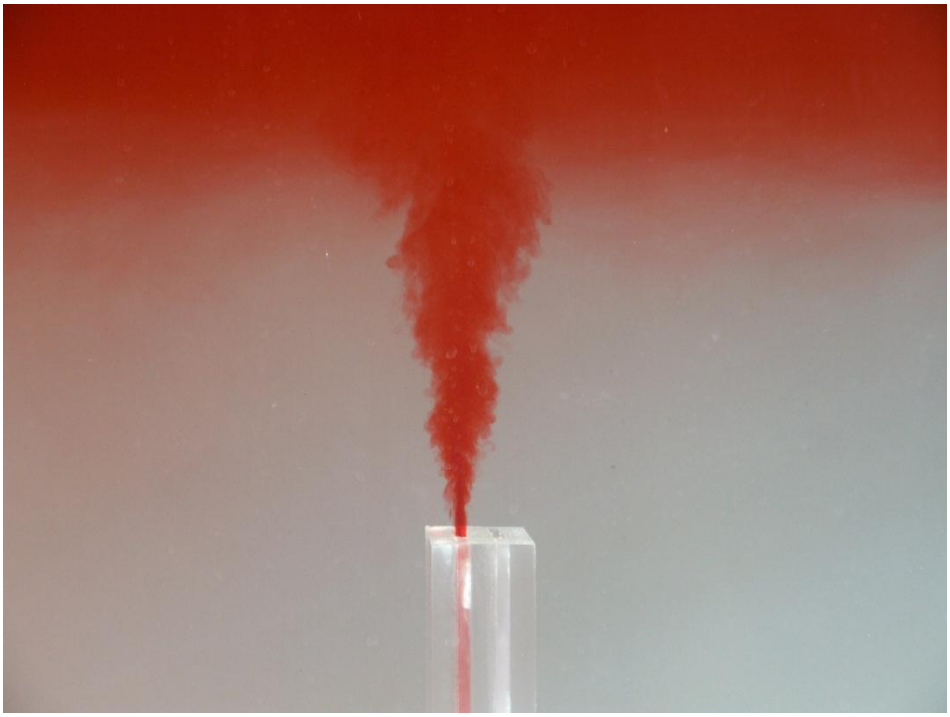

Figure 46. Dye Injection for a Single Jet Experiment Low Reynolds Number, Jet Temperature Near 40 C, Tank Temperature Near 15 C.

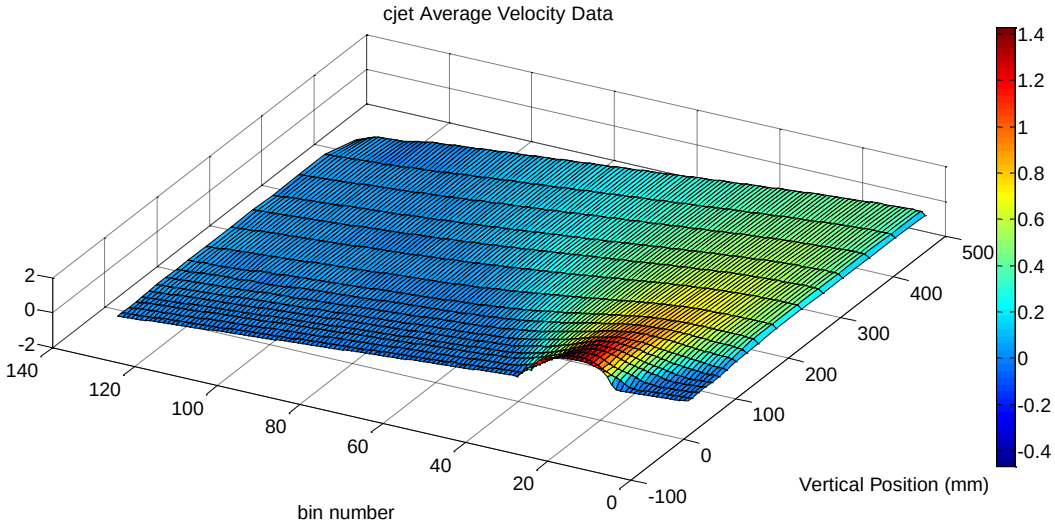

Figure 47. Cjet Average Velocity.

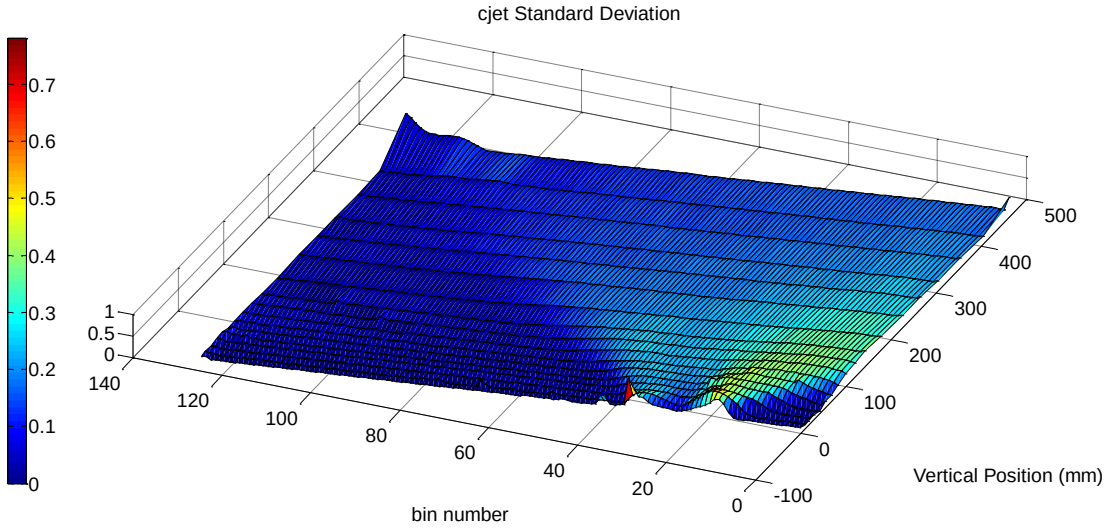

Figure 48. Cjet Standard Deviation.

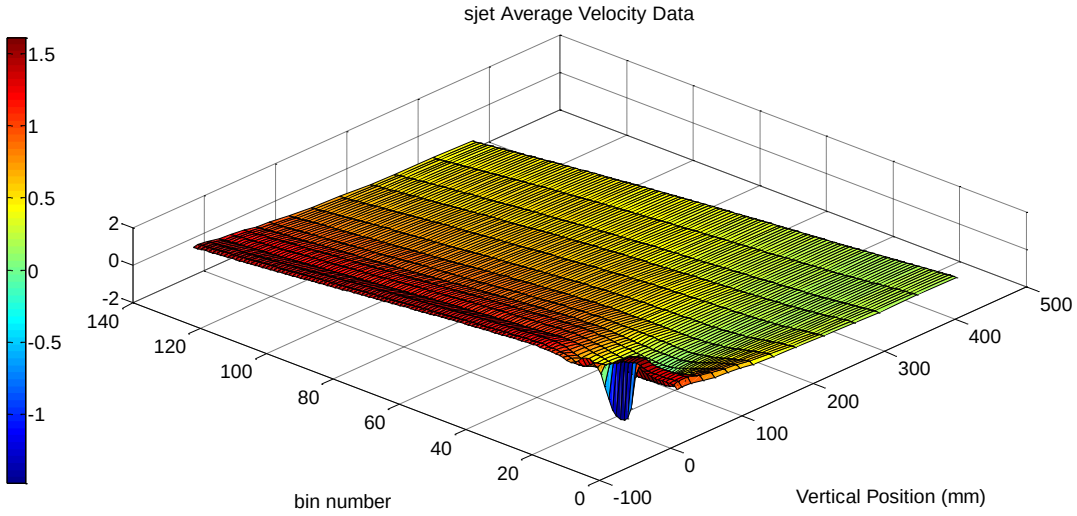

Figure 49. Sjet Average Velocity.

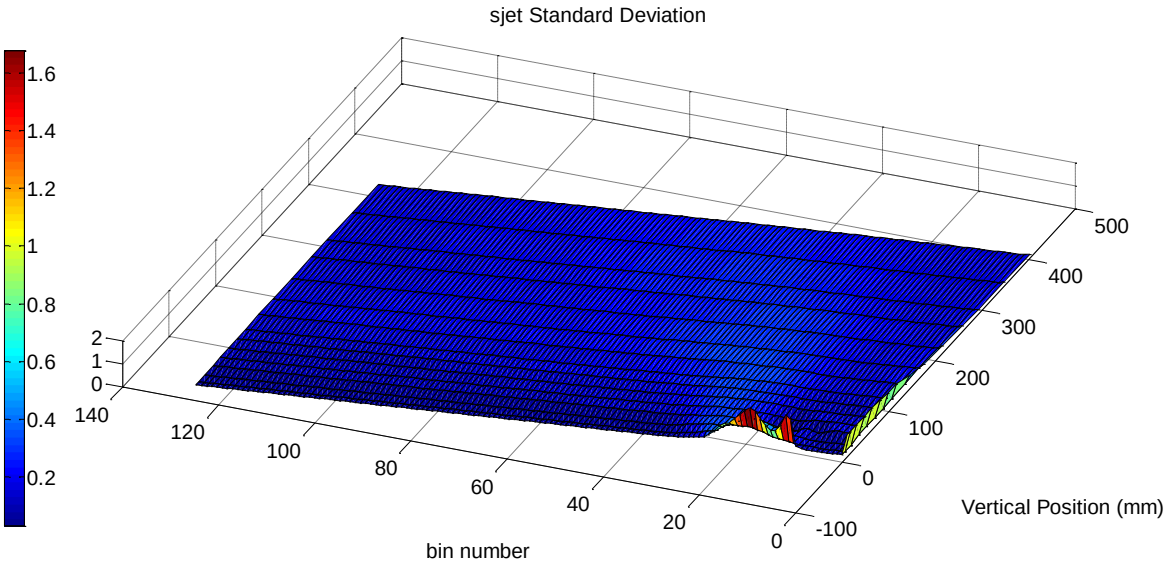

Figure 50. Sjet Standard Deviation.

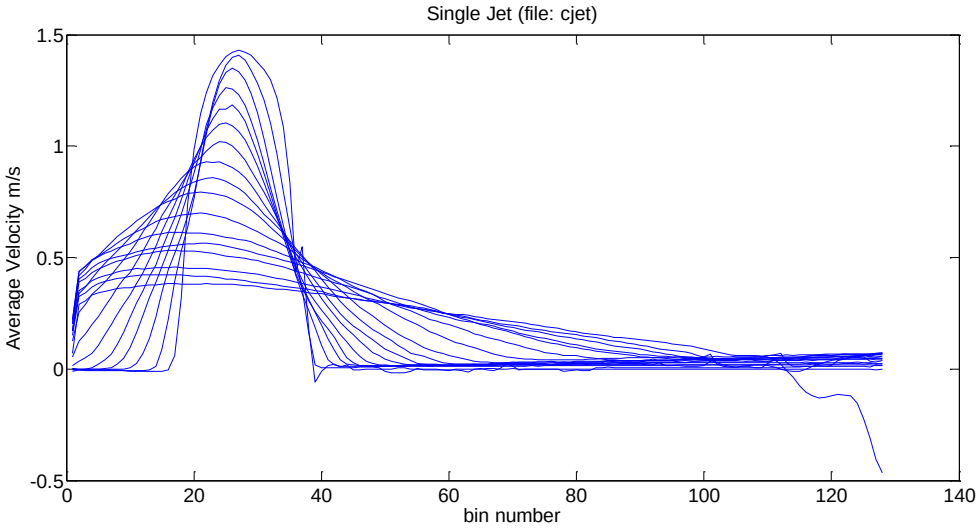

Figure 51. Single Jet Centerline Average Velocity (file: cjet).

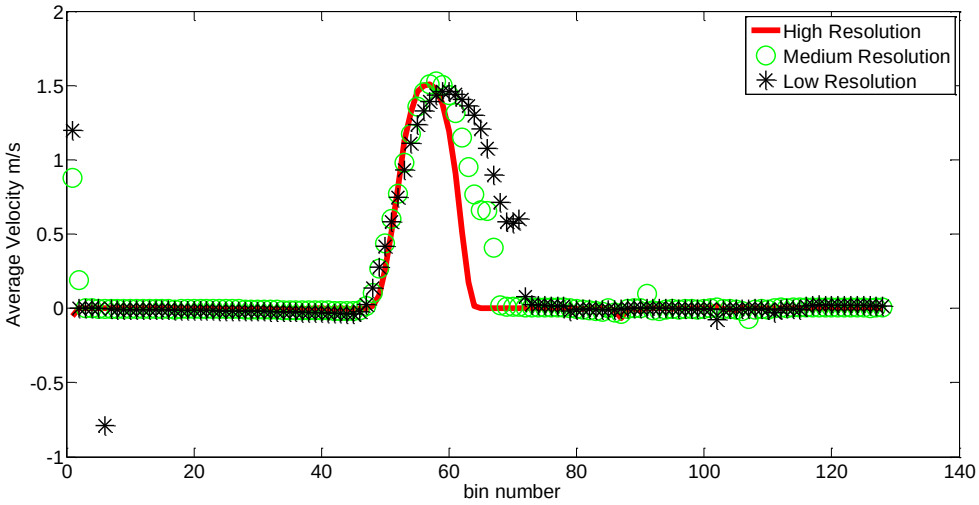

Figure 52. 3rd Level

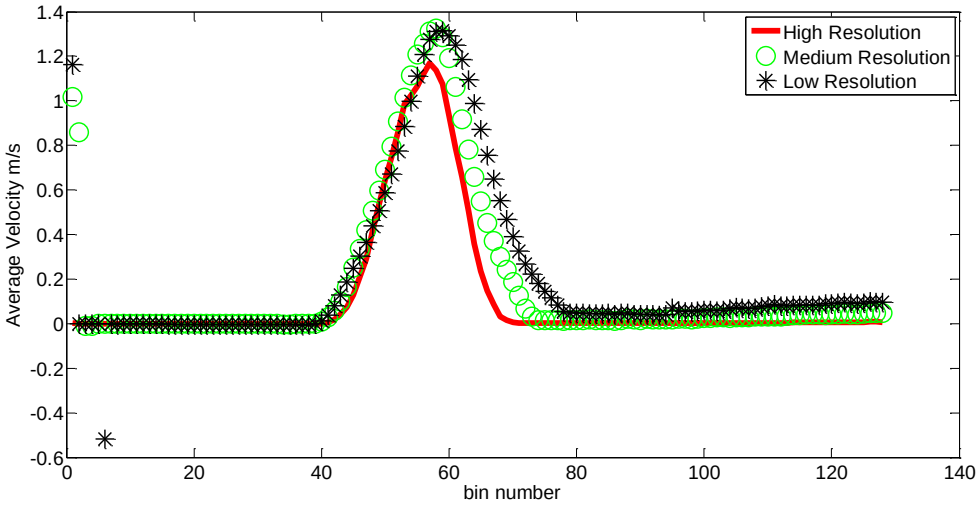

Figure 53. 6th Level

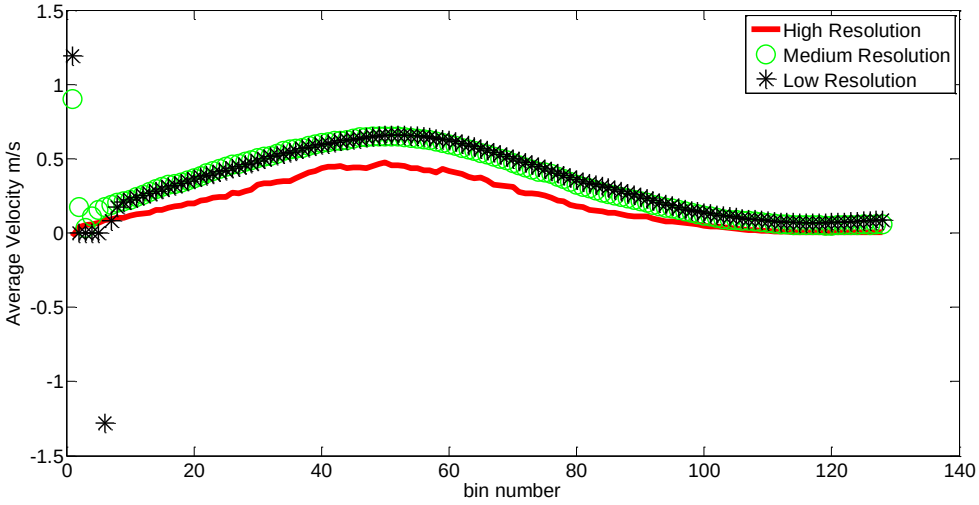

Figure 54. 17th Level

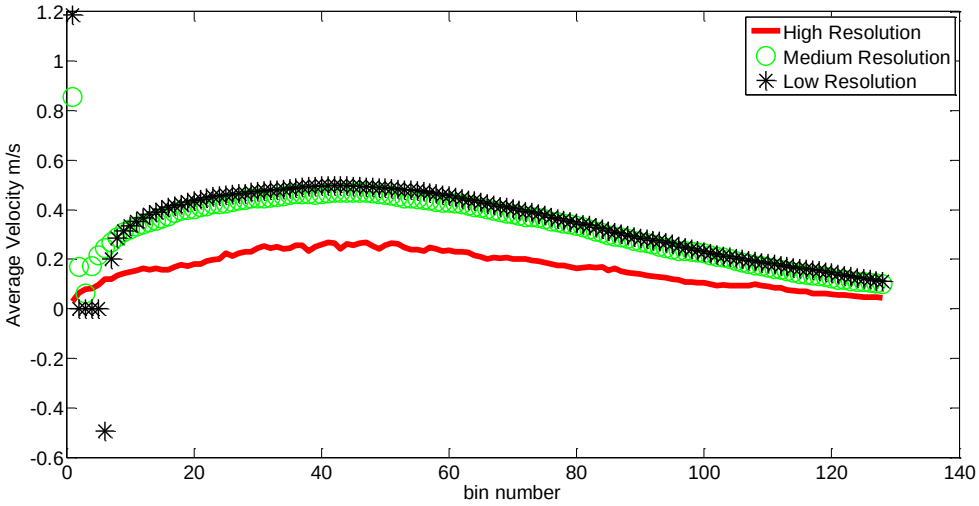

Figure 55. 21st Level

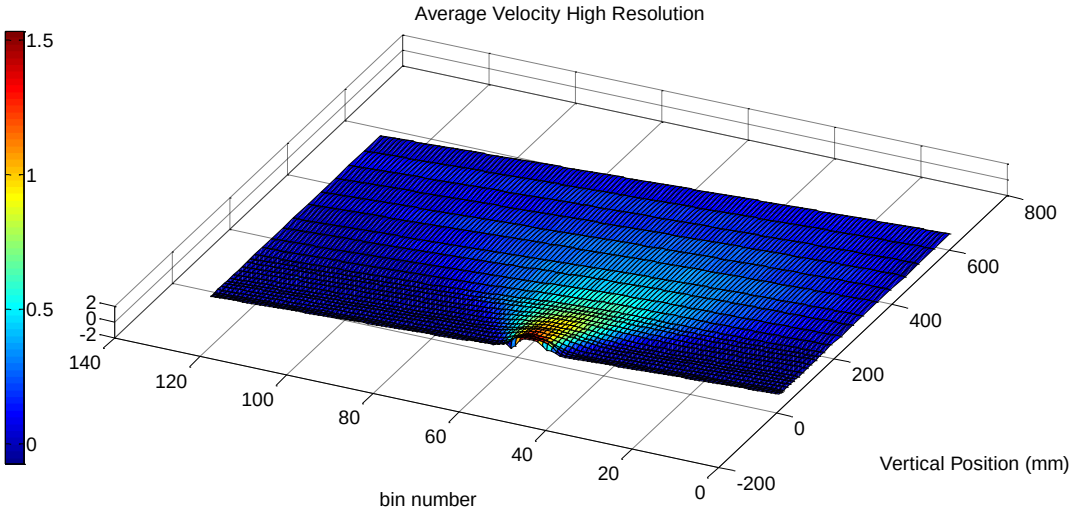

Figure 56. Single Jet Average Velocity High Resolution

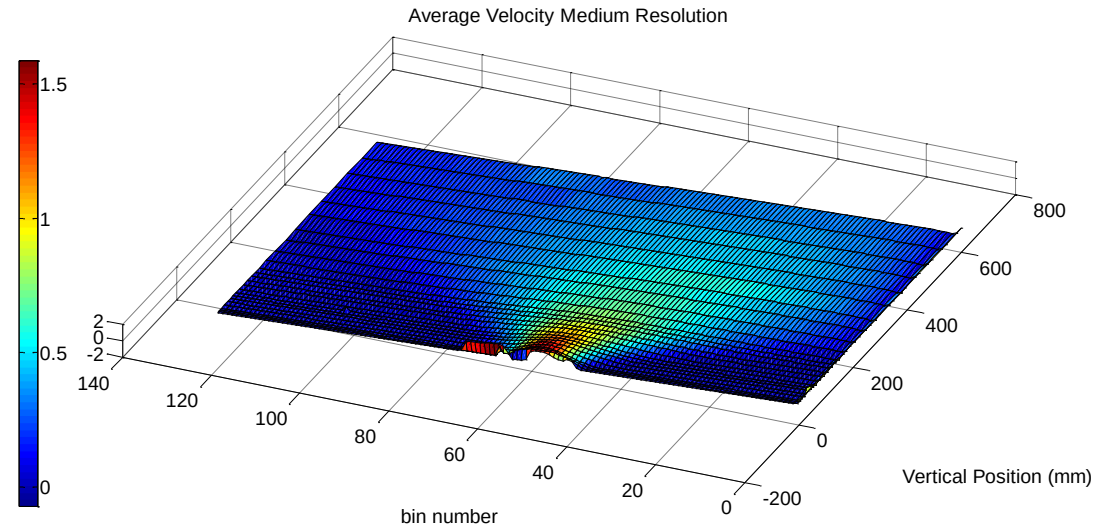

Figure 57. Single Jet Average Velocity Medium Resolution

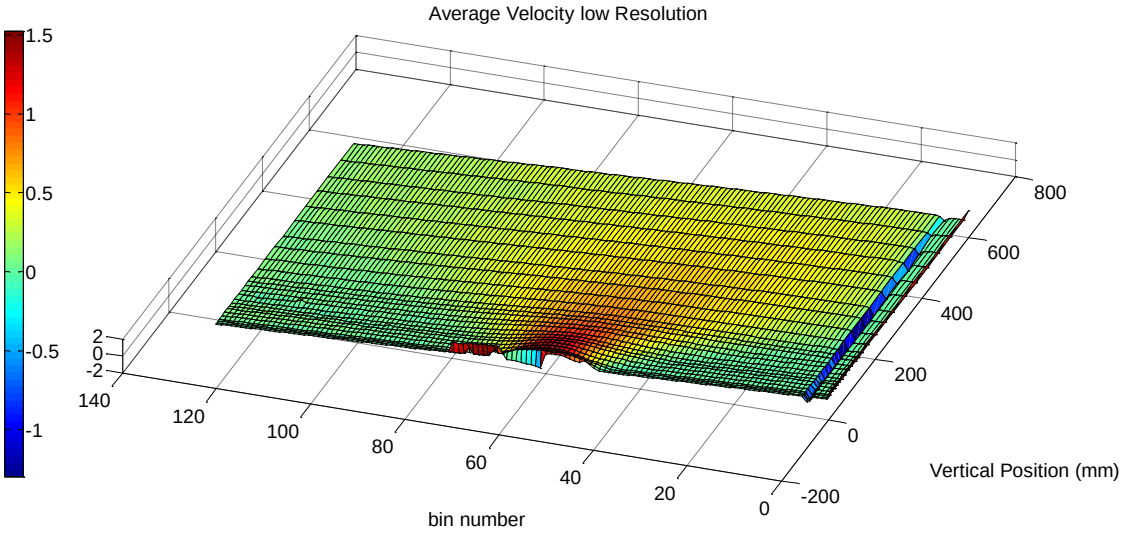

Figure 58. Single Jet Average Velocity Low Resolution

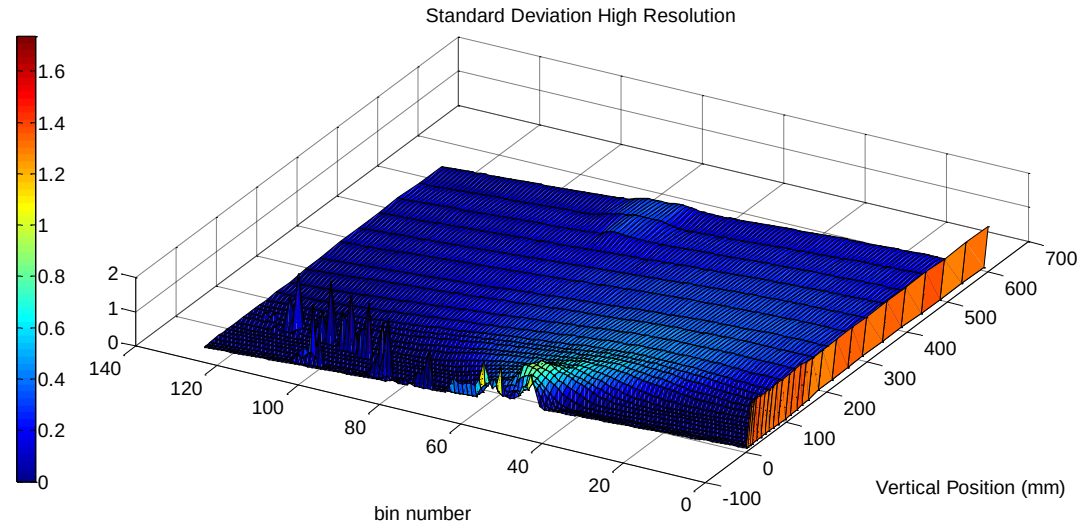

Figure 59. Single Jet Standard Deviation High Resolution

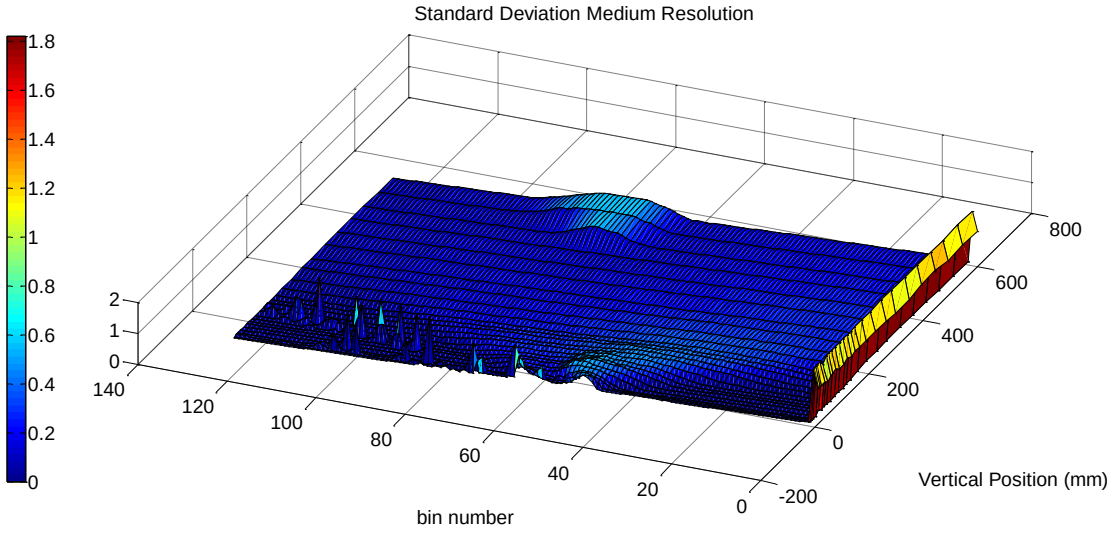

Figure 60. Single Jet Standard Deviation Medium Resolution

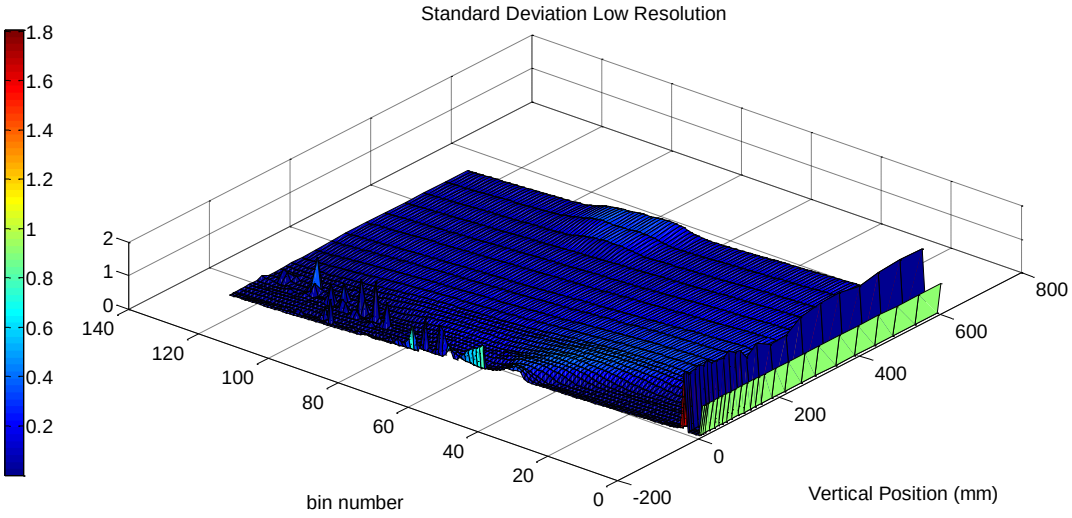

Figure 61. Single Jet Standard Deviation Low Resolution

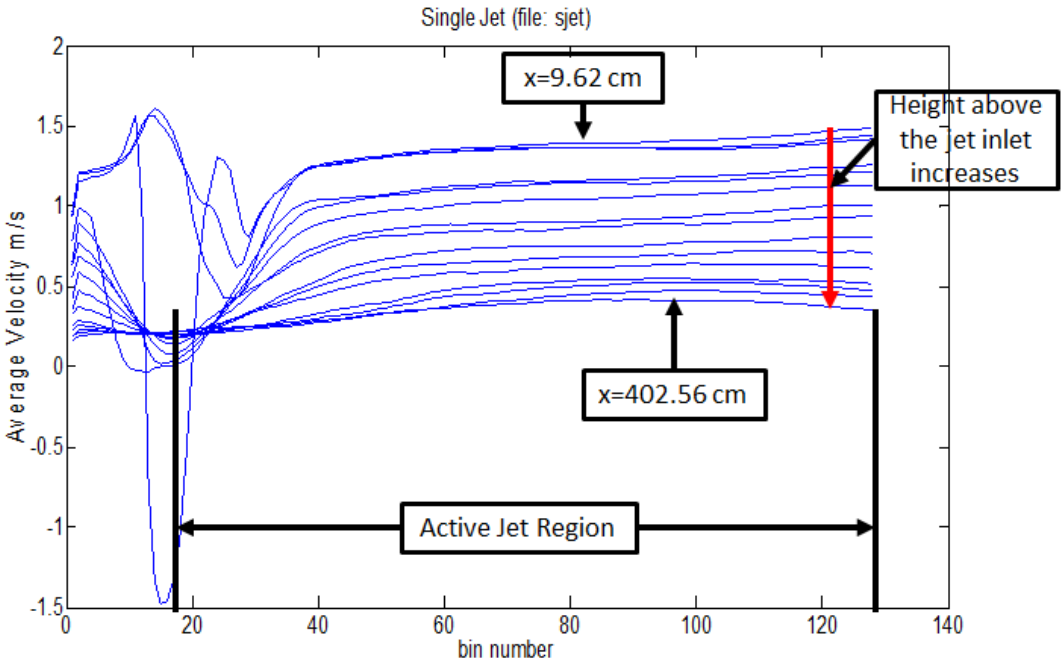

Figure 62. Single Jet Centerline Average Velocity (file: sjet).

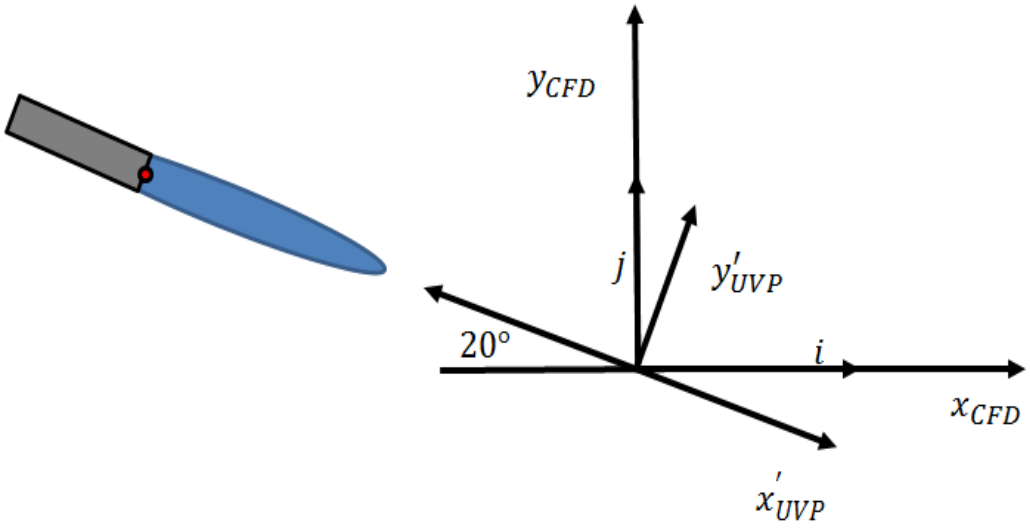

Figure 63. Axis Transformation

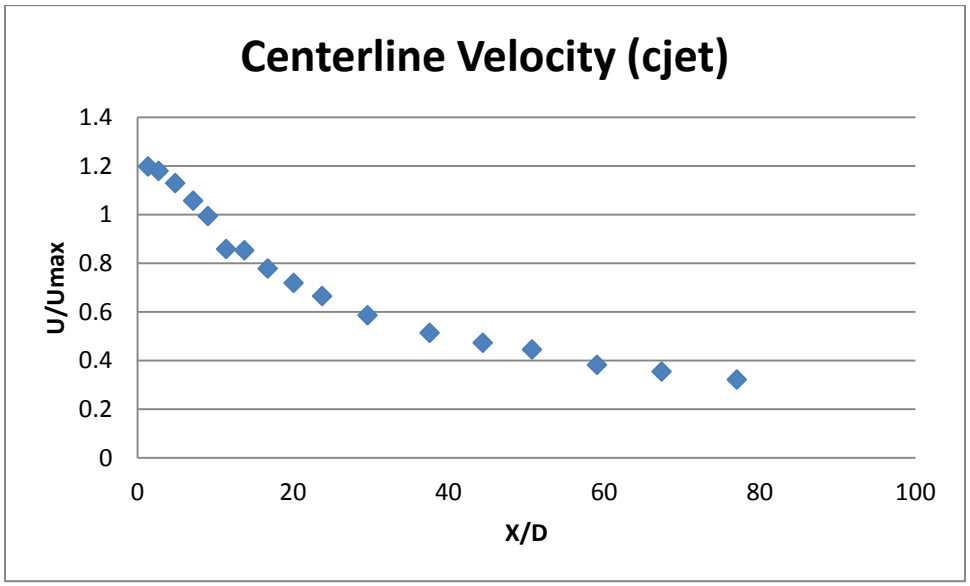

Figure 64. cjet Centerline Velocity

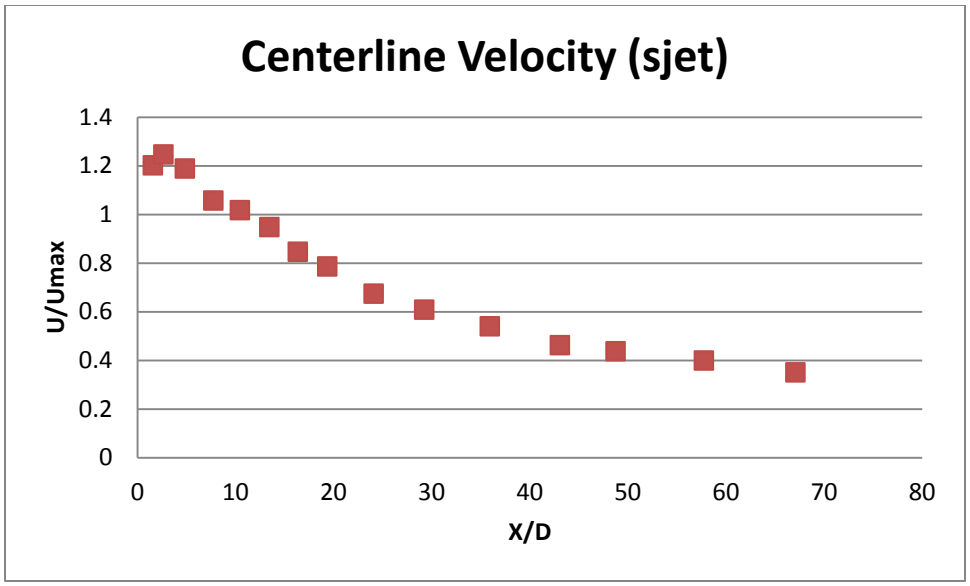

Figure 65. sjet Centerline Velocity

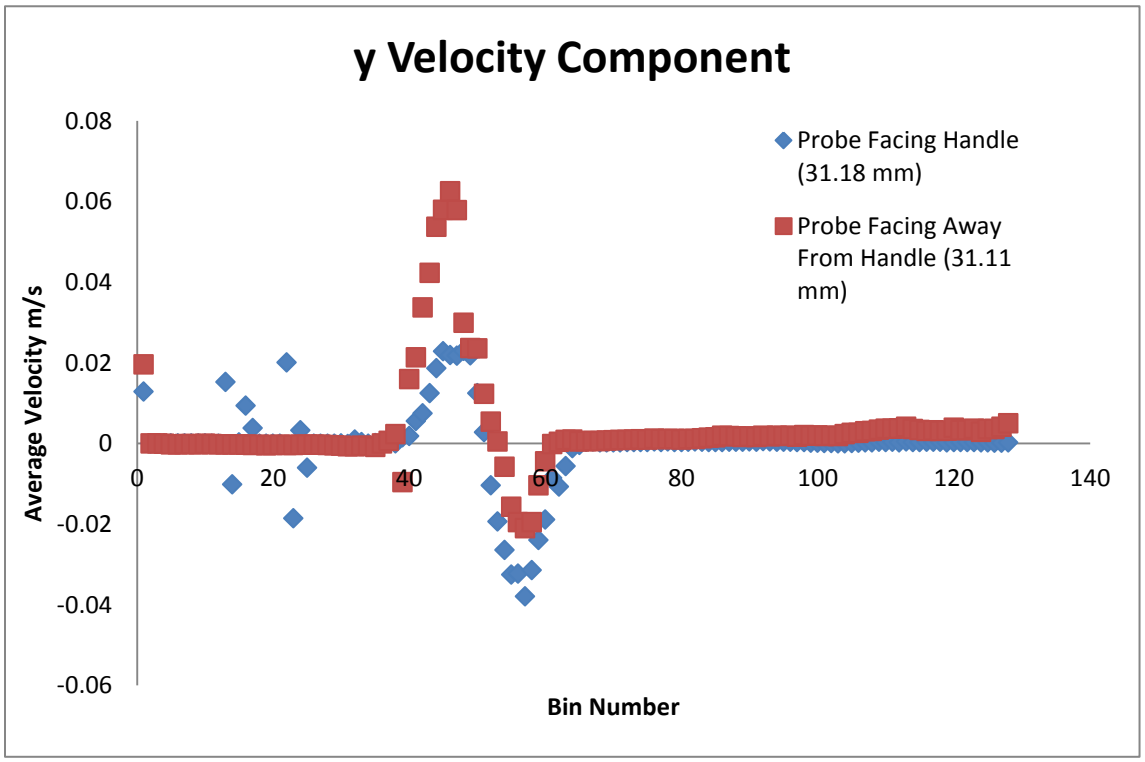

Figure 66. High Resolution y Velocity Component ~31 mm

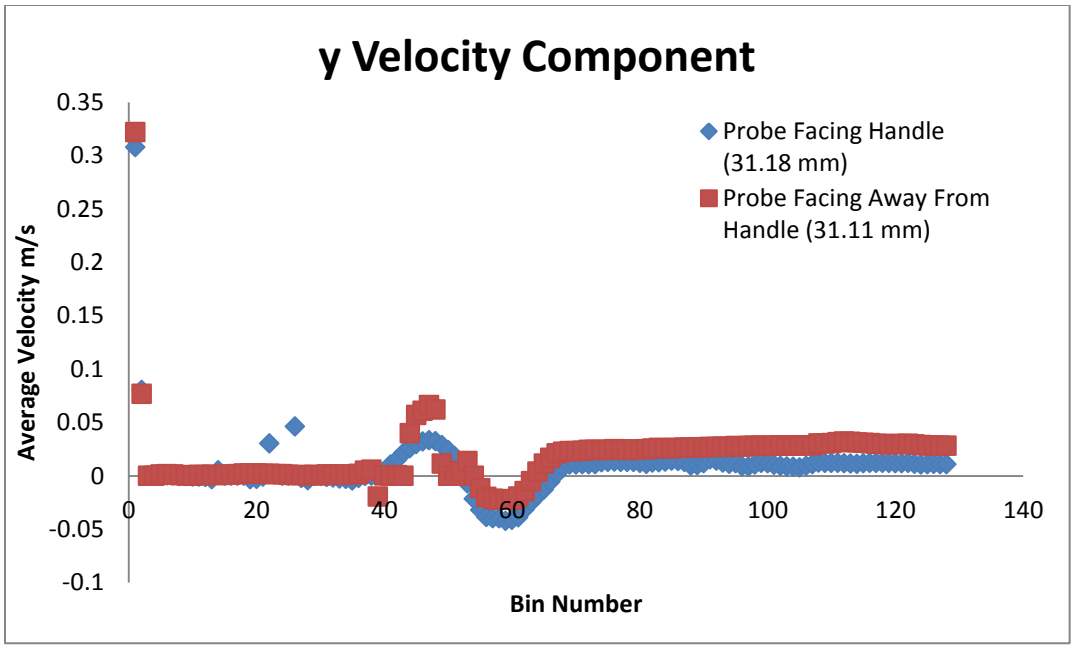

Figure 67. Medium Resolution y Velocity Component ~31 mm

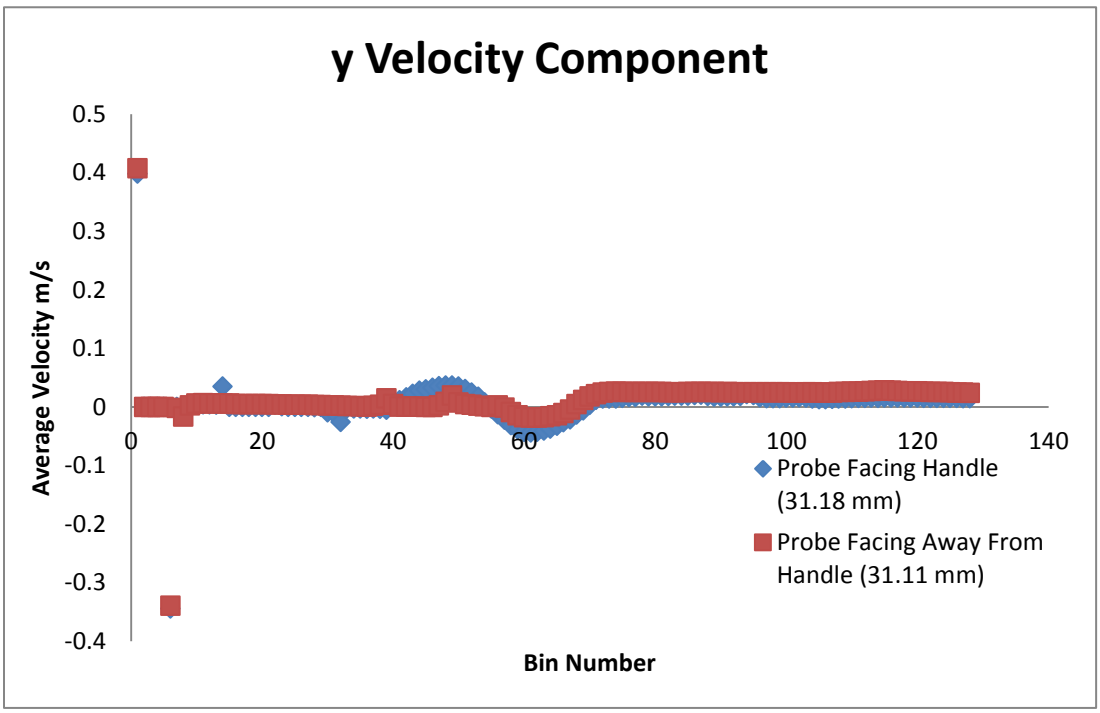

Figure 68. Low Resolution y Velocity Component ~31 mm

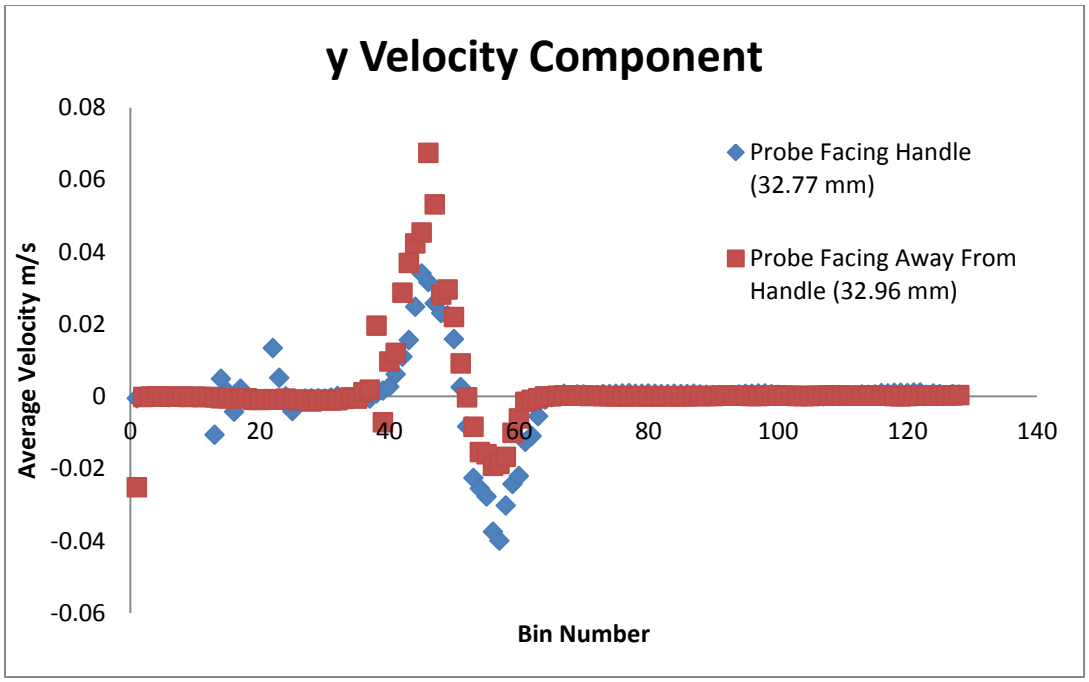

Figure 69. High Resolution y Velocity Component ~33 mm

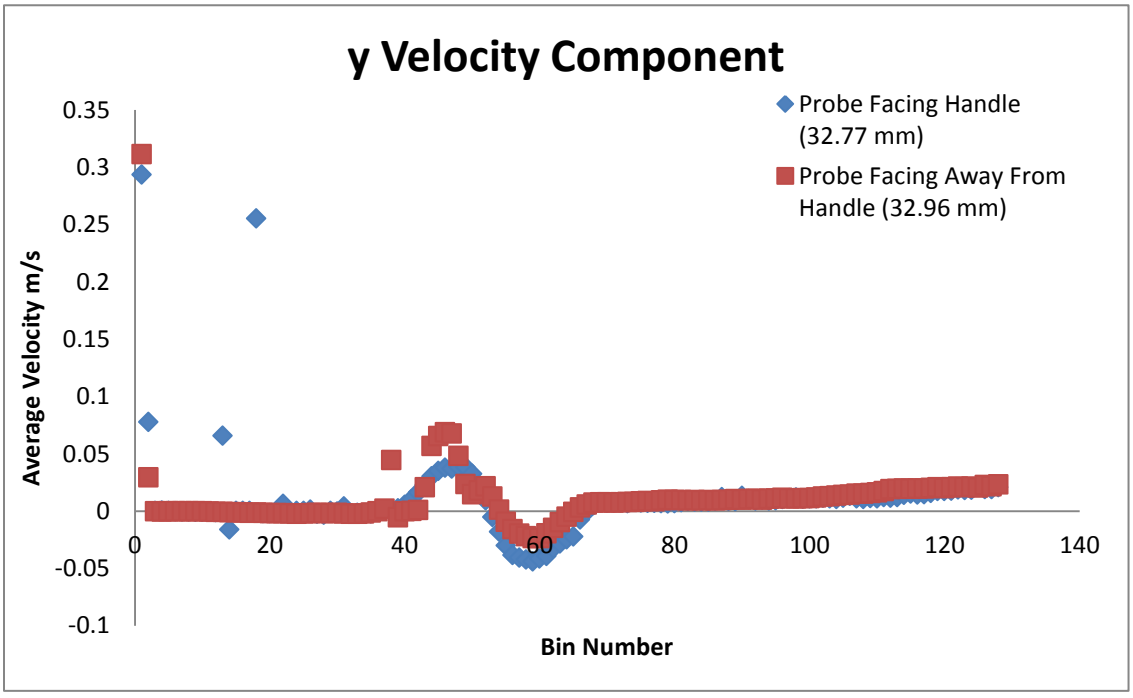

Figure 70. Medium Resolution y Velocity Component ~33 mm

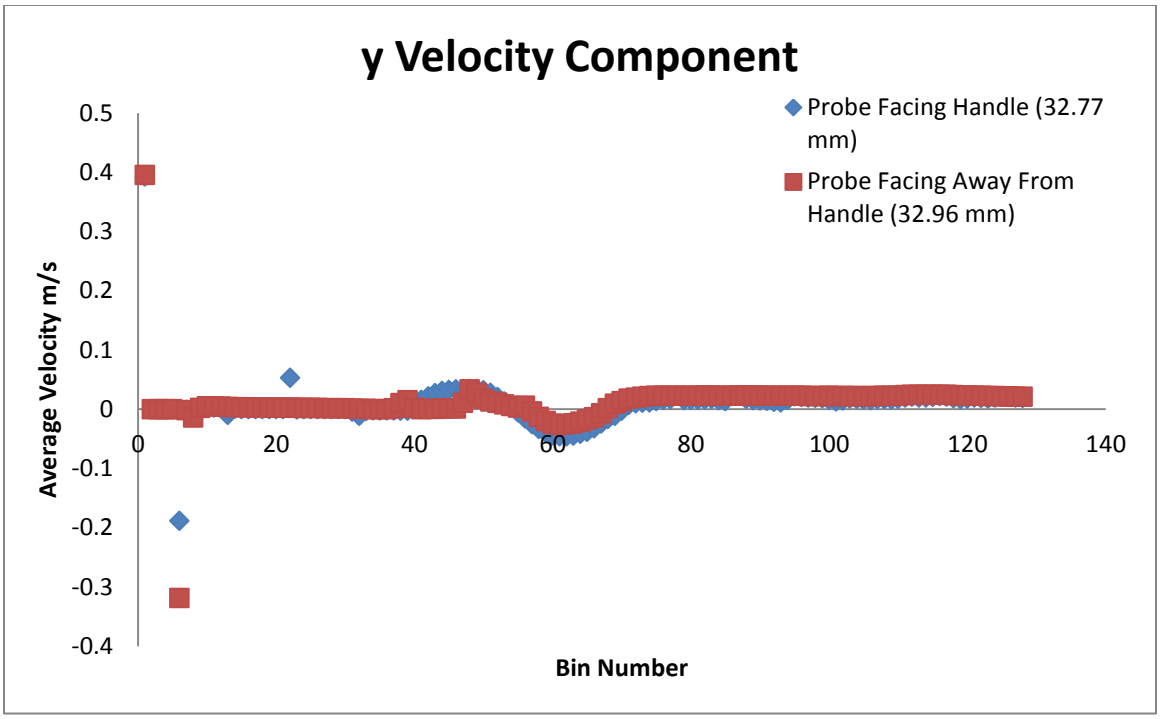

Figure 71. Low Resolution y Velocity Component ~33 mm

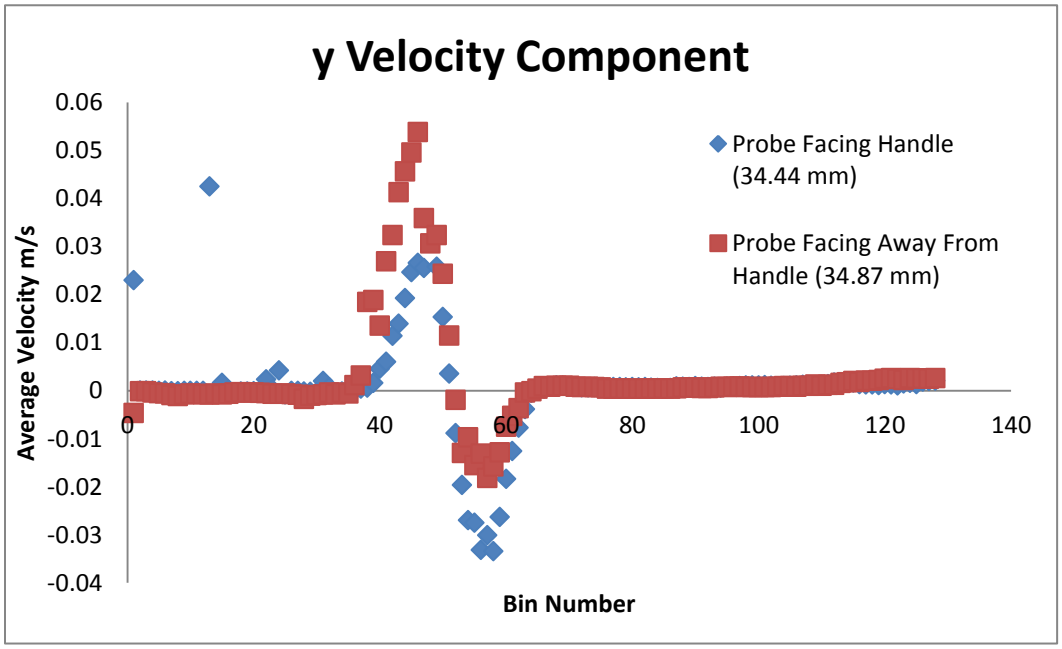

Figure 72. High Resolution y Velocity Component ~34 mm

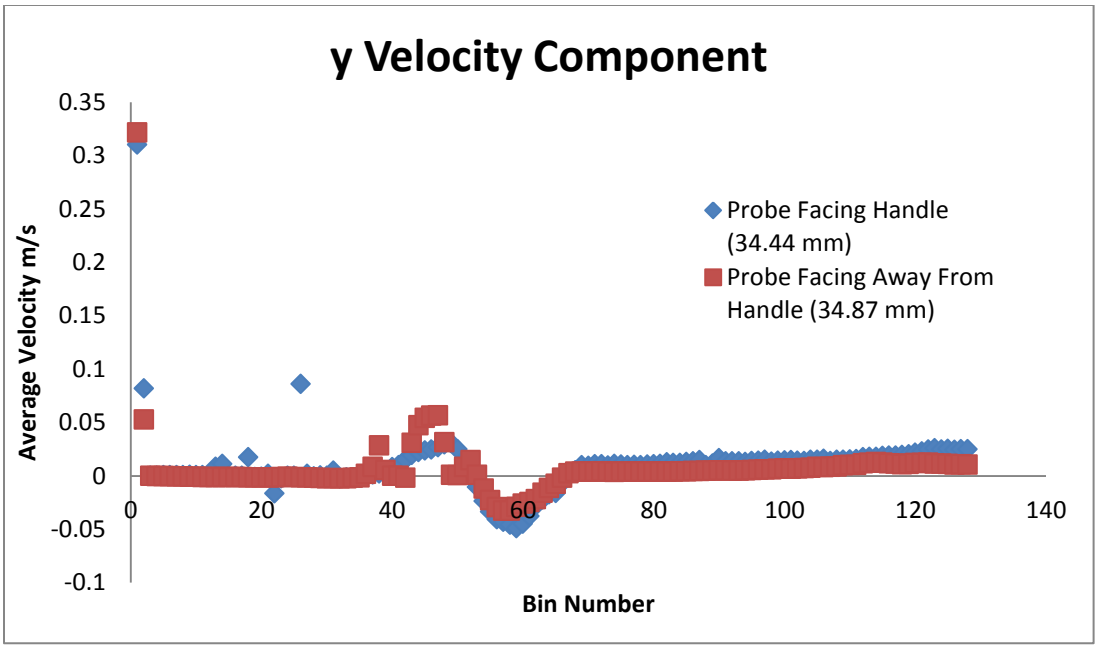

Figure 73. Medium Resolution y Velocity Component ~34 mm

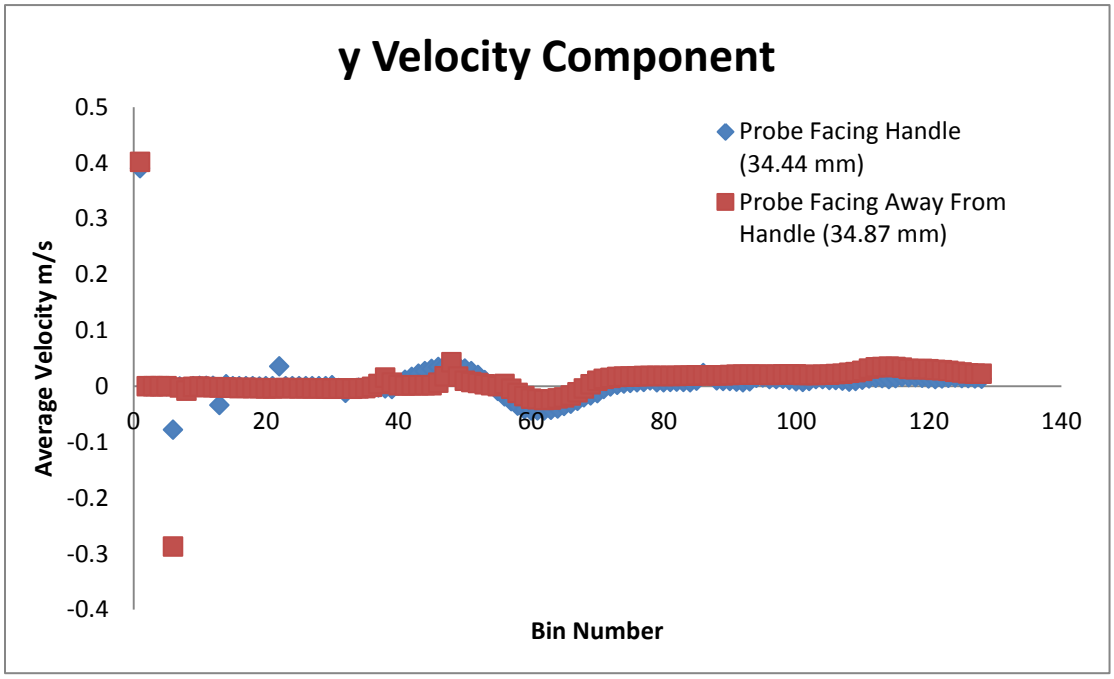

Figure 74. Low Resolution y Velocity Component ~34 mm

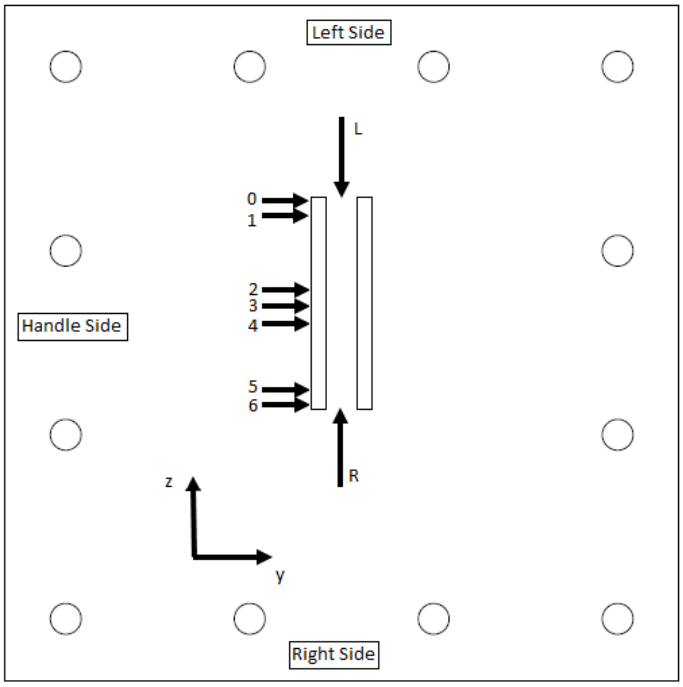

Figure 75. Dual Jet Graphical Description.

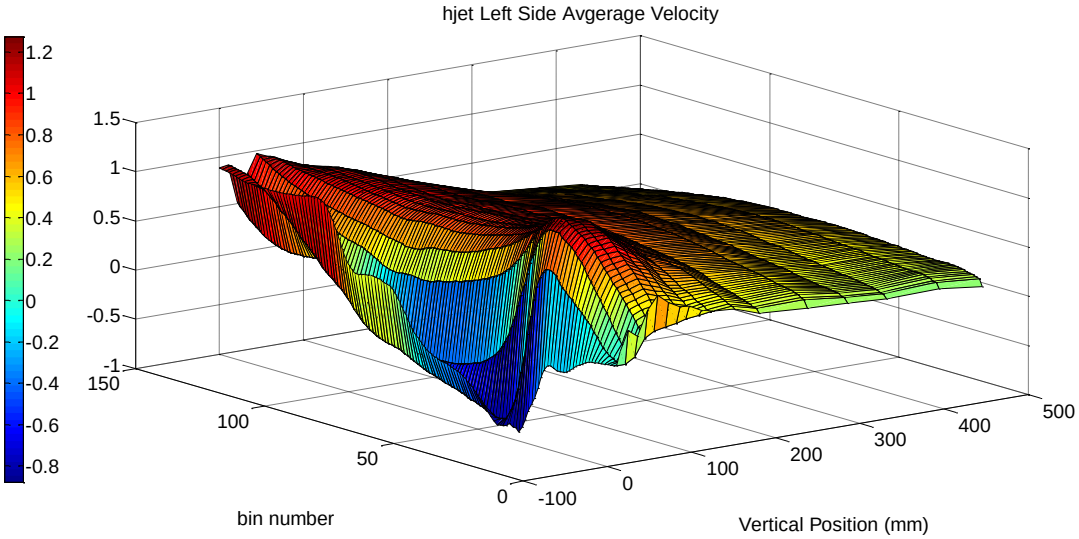

Figure 76. hjet Left Side Average Velocity.

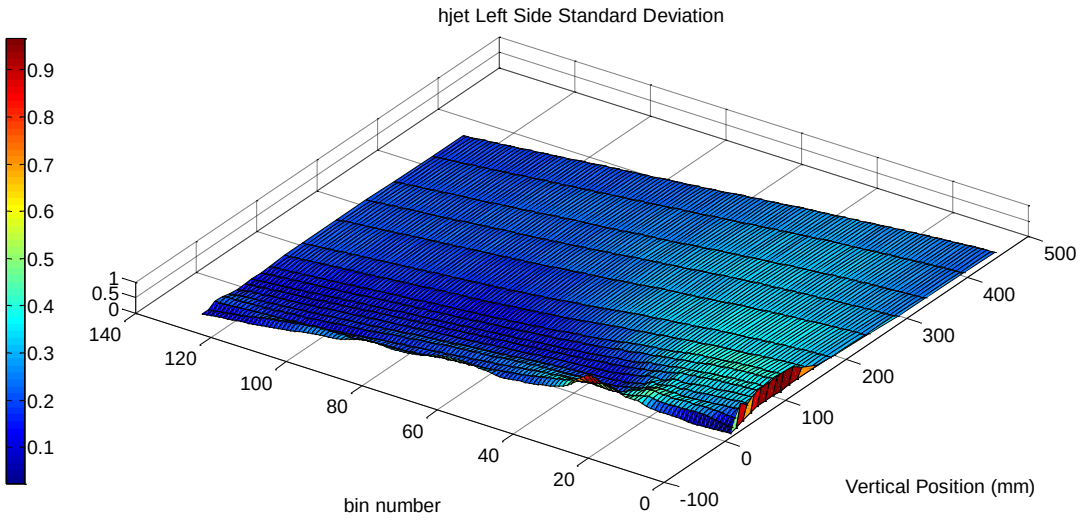

Figure 77. hjet Left Side Standard Deviation.

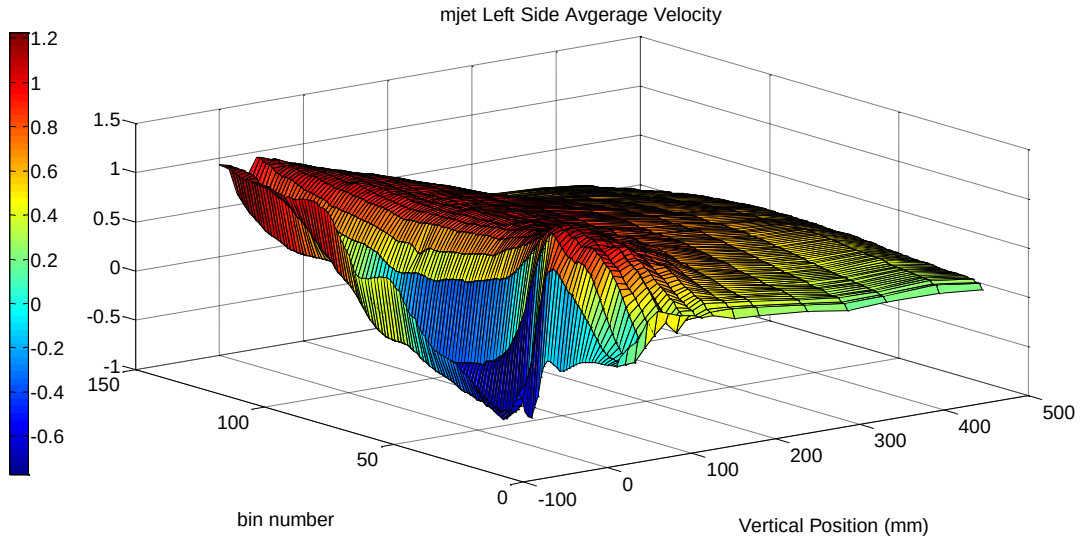

Figure 78. mjet Left Side Average Velocity.

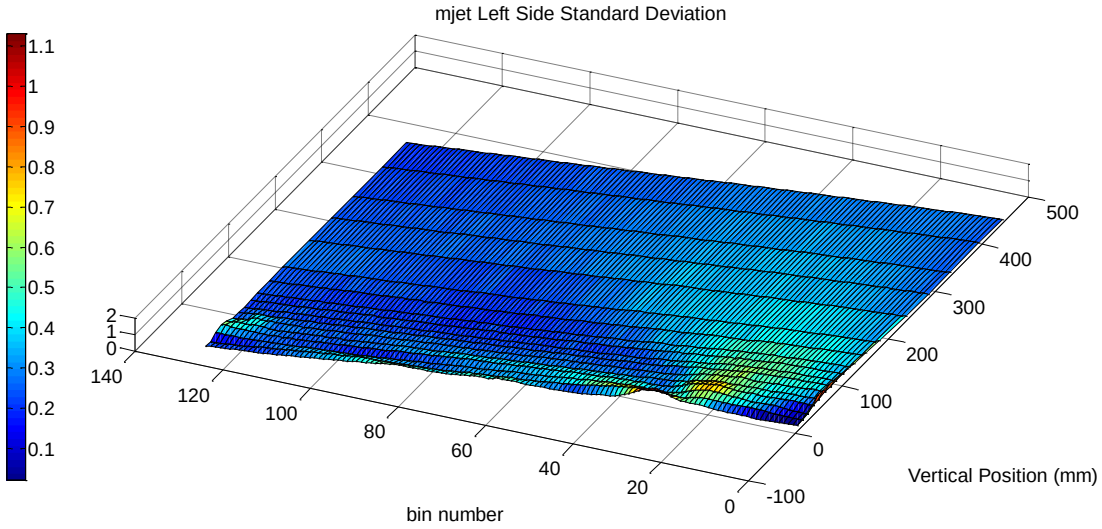

Figure 79. mjet Left Side Standard Deviation.

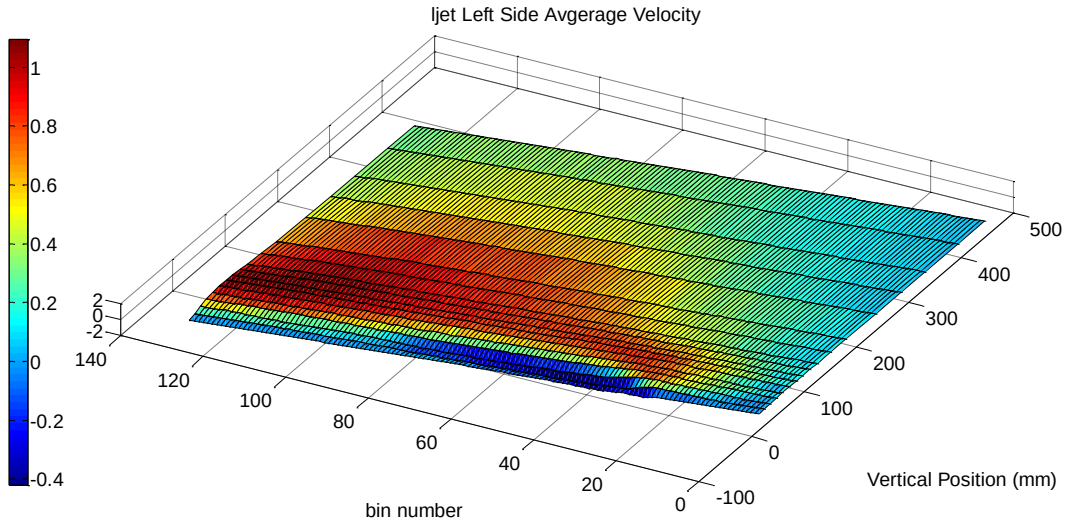

Figure 80. ljet Left Side Average Velocity.

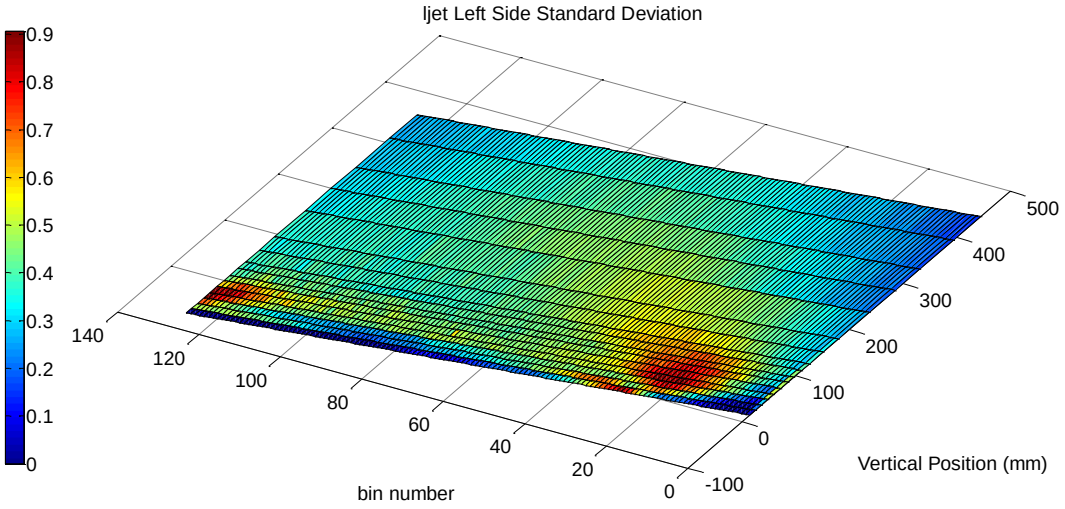

Figure 81. ljet Left Side Standard Deviation.

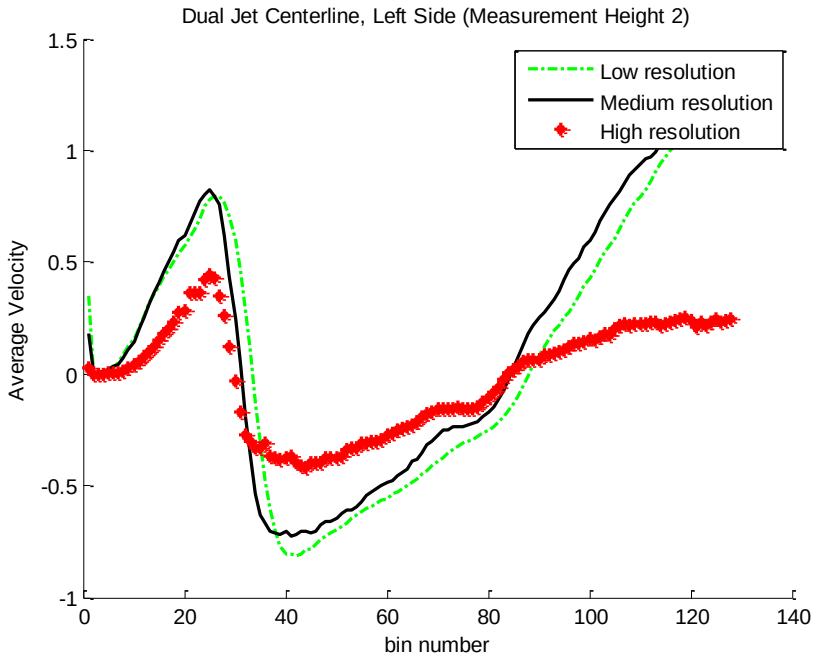

Figure 82. Dual Jet Centerline, Left Side (Height 2).

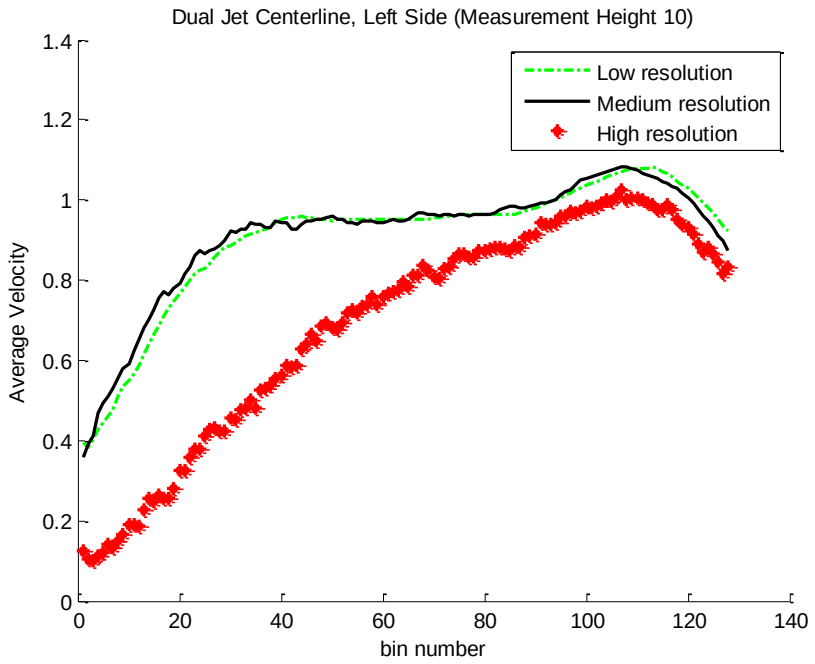

Figure 83. Dual Jet Centerline, Left Side (Height 10).

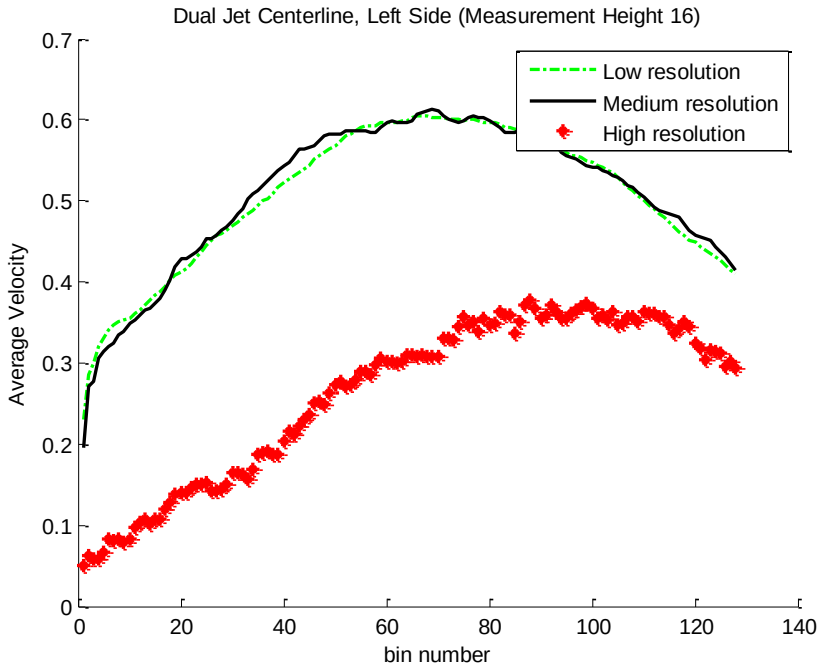

Figure 84. Dual Jet Centerline, Left Side (Height 16).

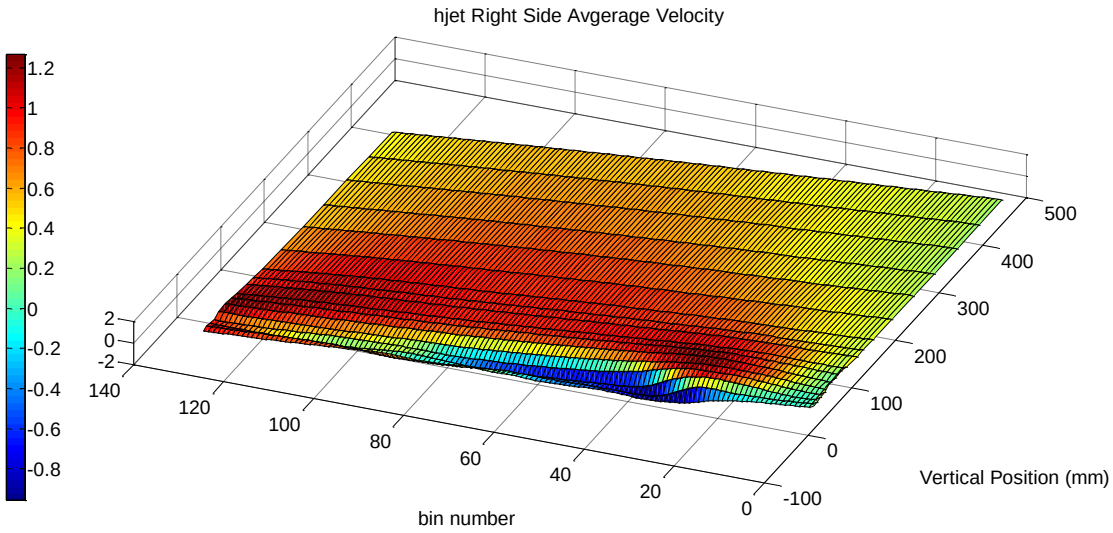

Figure 85. hjet Right Side Average Velocity.

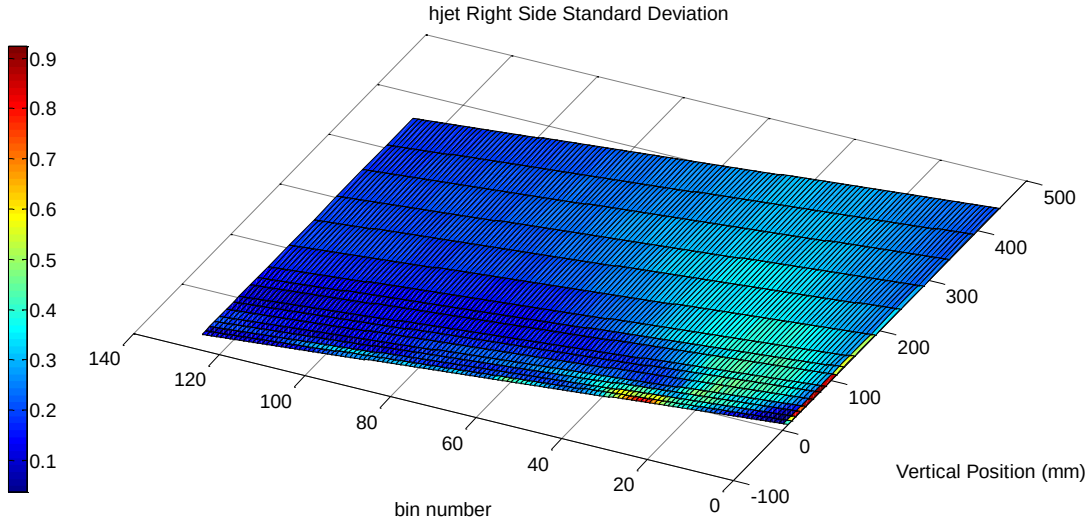

Figure 86. hjet Right Side Standard Deviation.

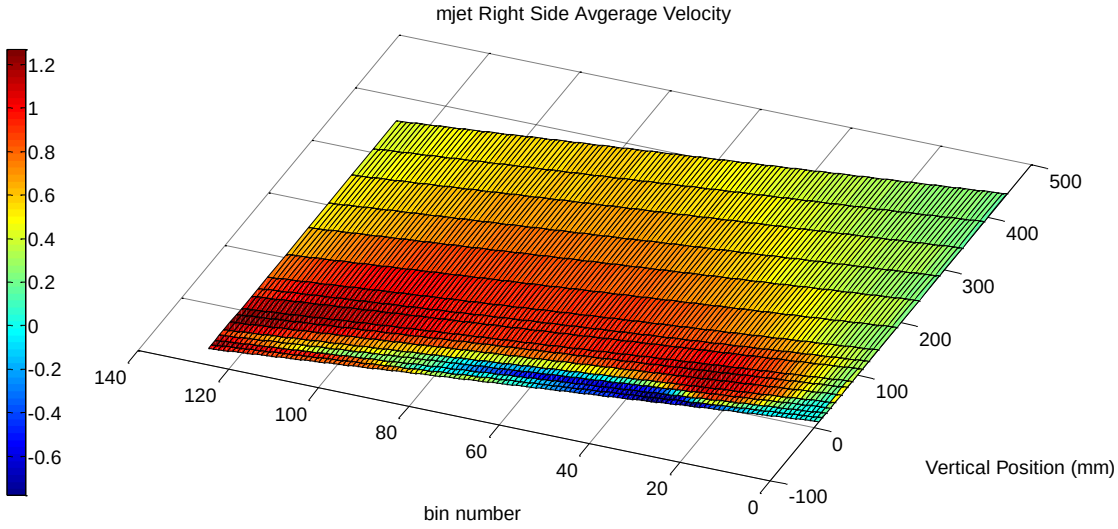

Figure 87. mjet Right Side Average Velocity.

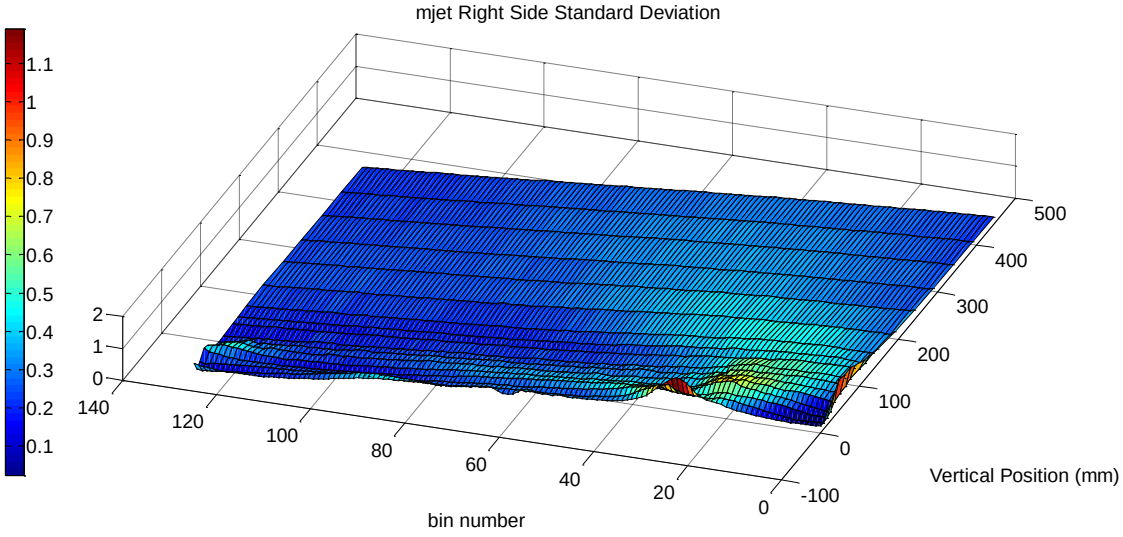

Figure 88. mjet Right Side Standard Deviation.

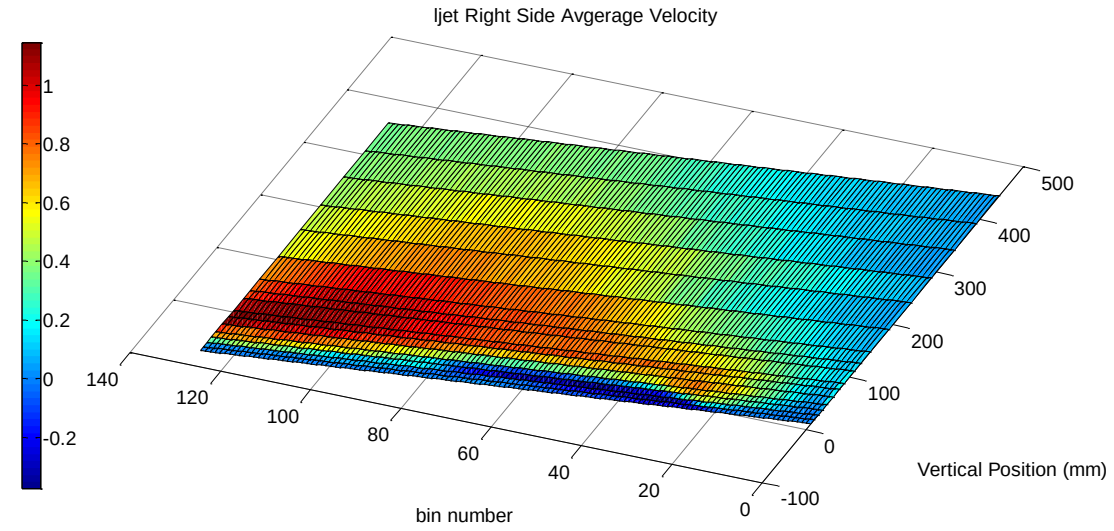

Figure 89. ljet Right Side Average Velocity.

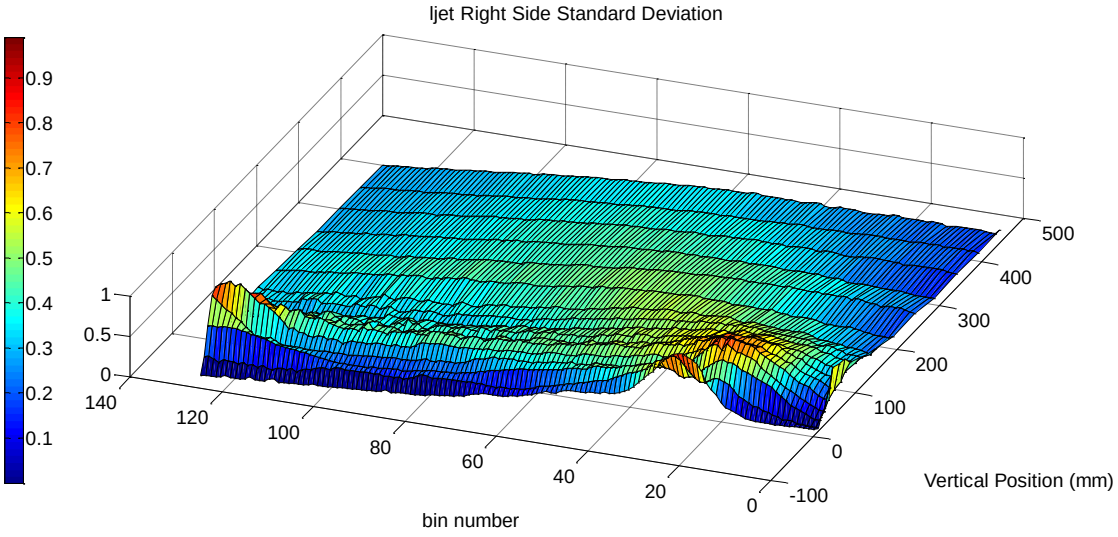

Figure 90. ljet Right Side Standard Deviation.

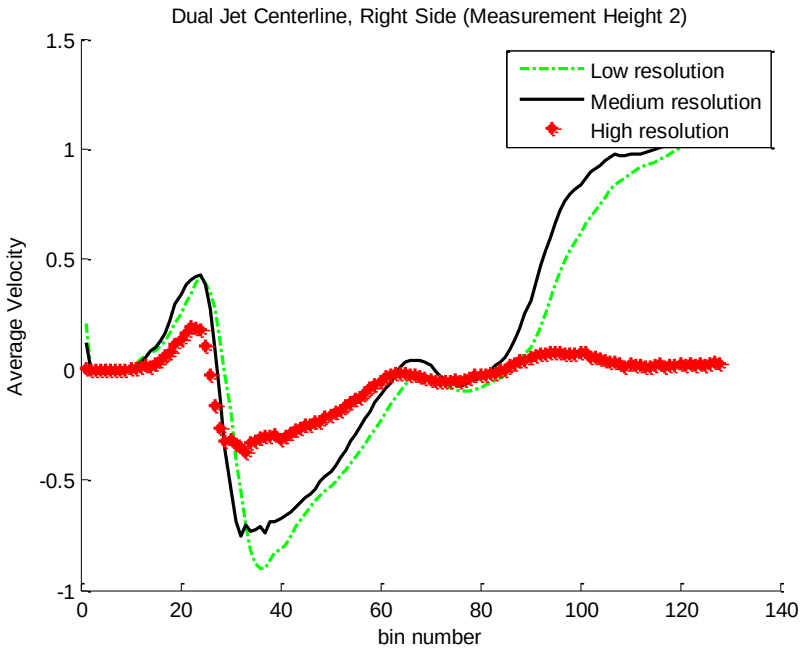

Figure 91. Dual Jet Centerline, Right Side (Height 2).

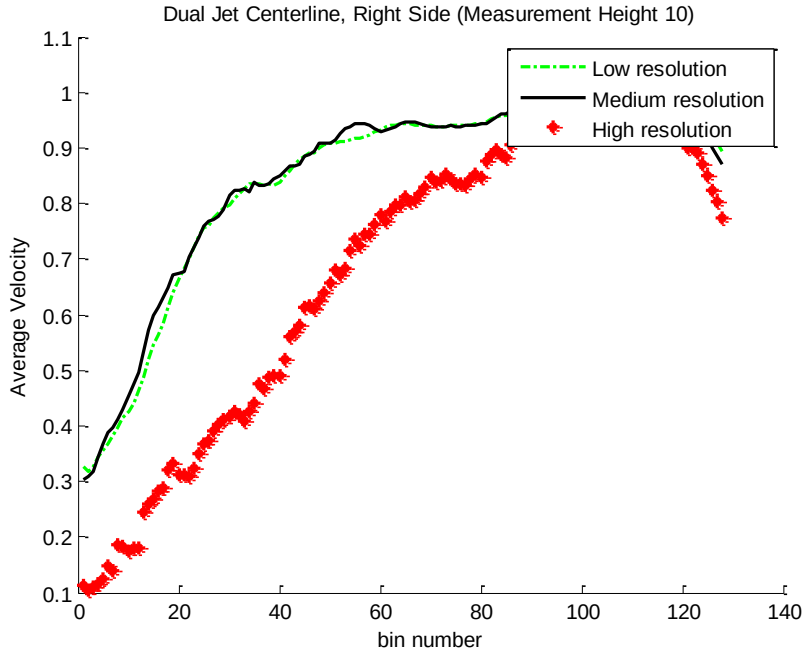

Figure 92. Dual Jet Centerline, Right Side (Height 10).

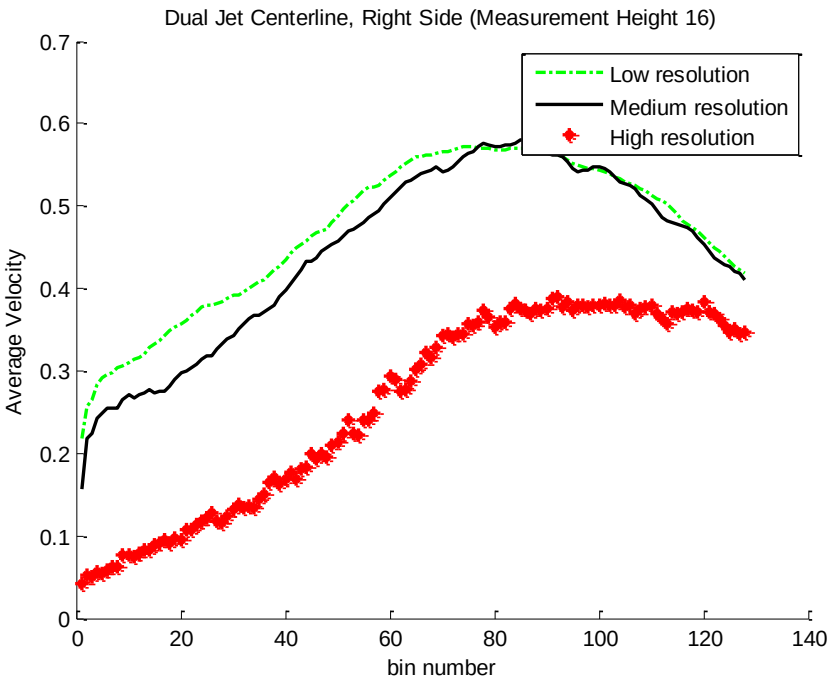

Figure 93. Dual Jet Centerline, Right Side (Height 16).

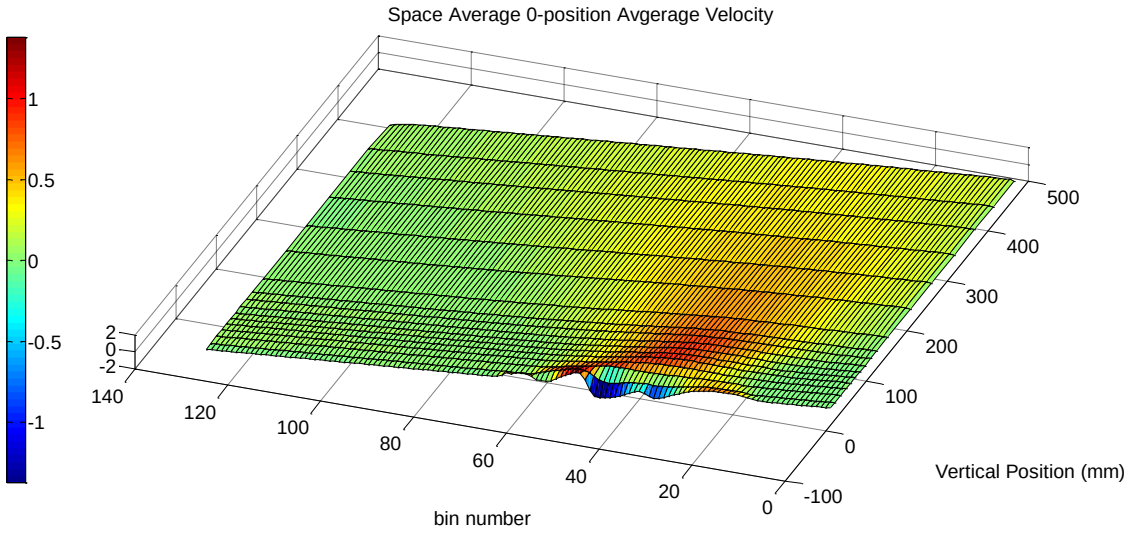

Figure 94. Space Average 0-position Average Velocity.

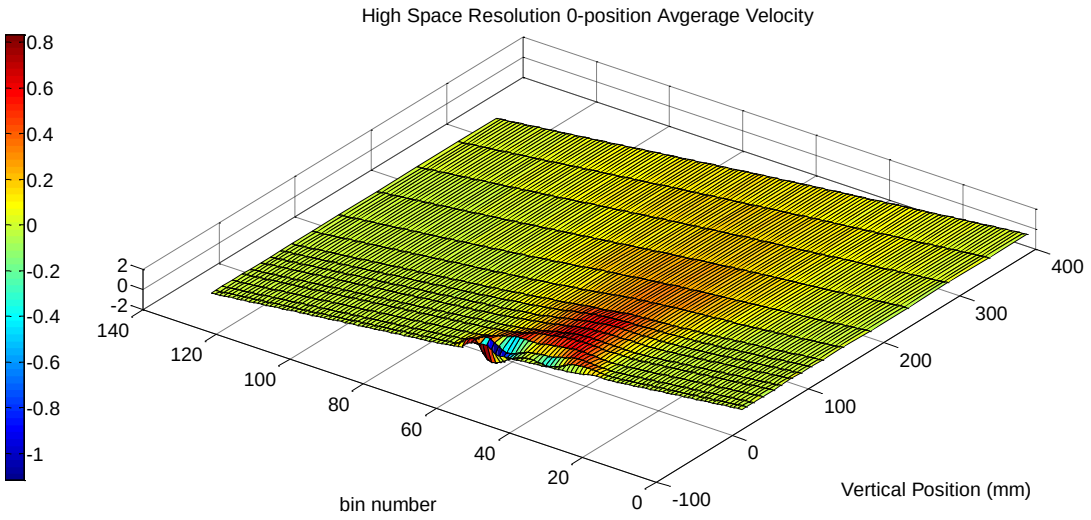

Figure 95. High Space Resolution 0-position Average Velocity.

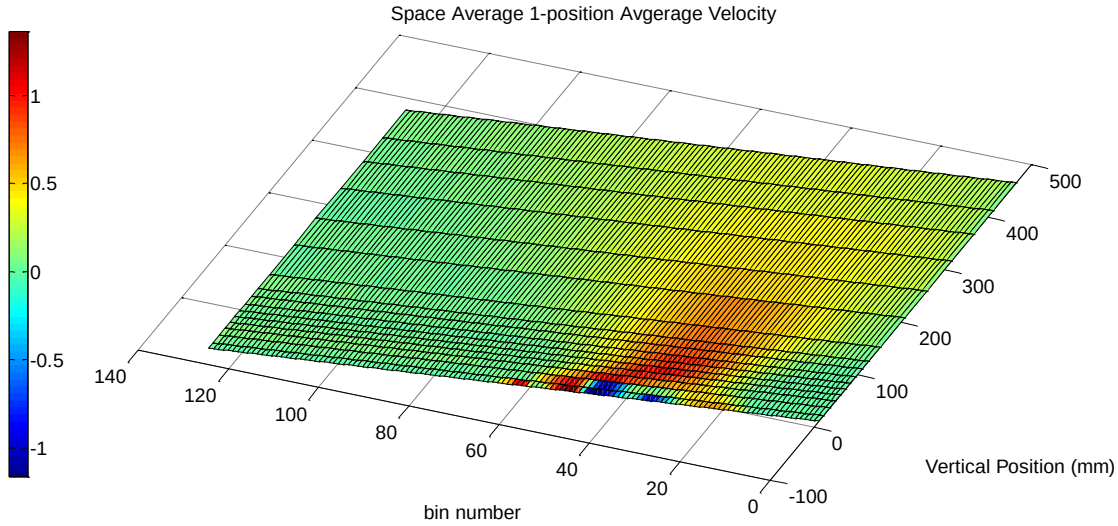

Figure 96. Space Average 1-position Average Velocity.

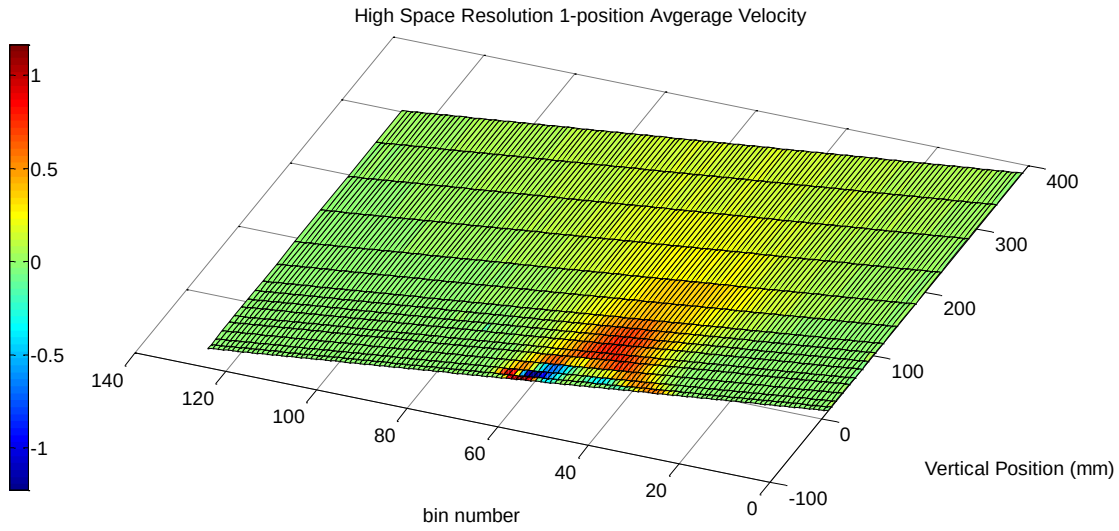

Figure 97. High Space Resolution 1-position Average Velocity.

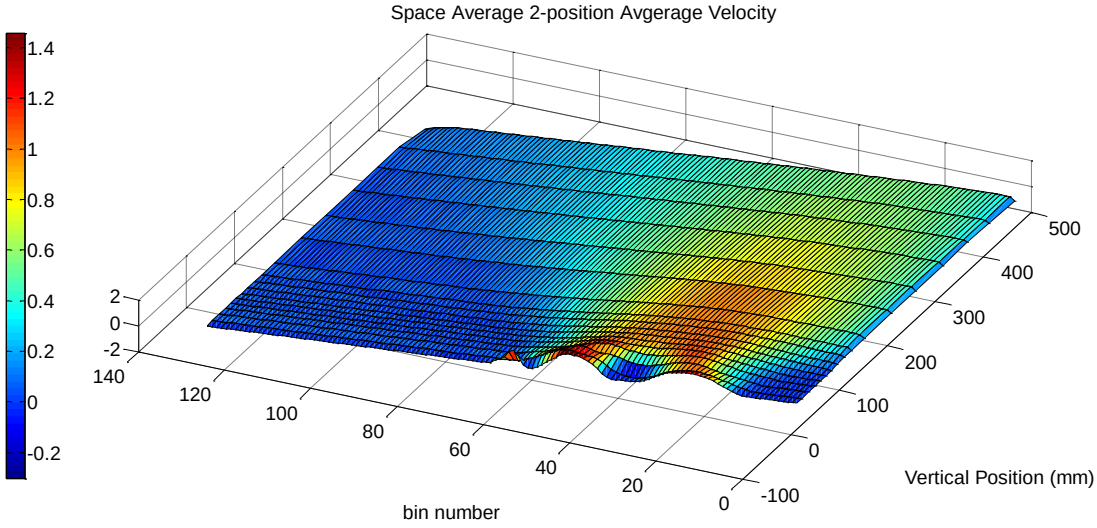

Figure 98. Space Average 2-position Average Velocity.

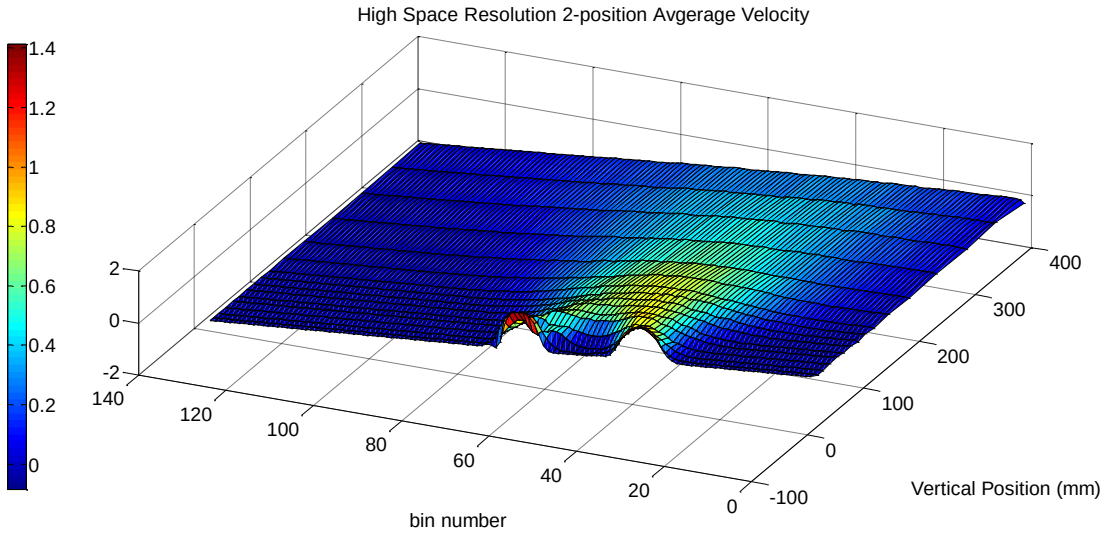

Figure 99. High Space Resolution 2-position Average Velocity.

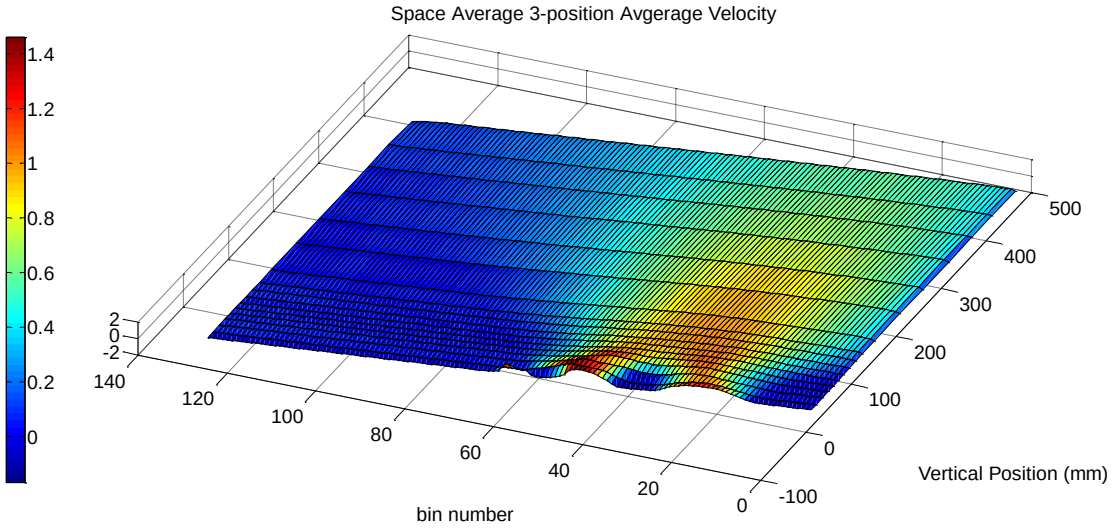

Figure 100. Space Average 3-position Average Velocity.

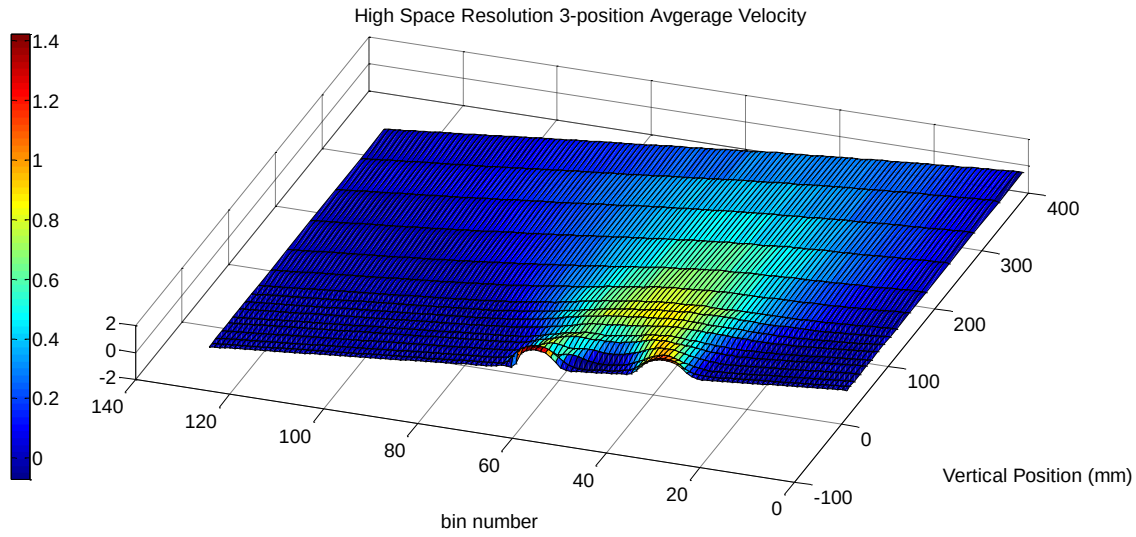

Figure 101. High Space Resolution 3-position Average Velocity.

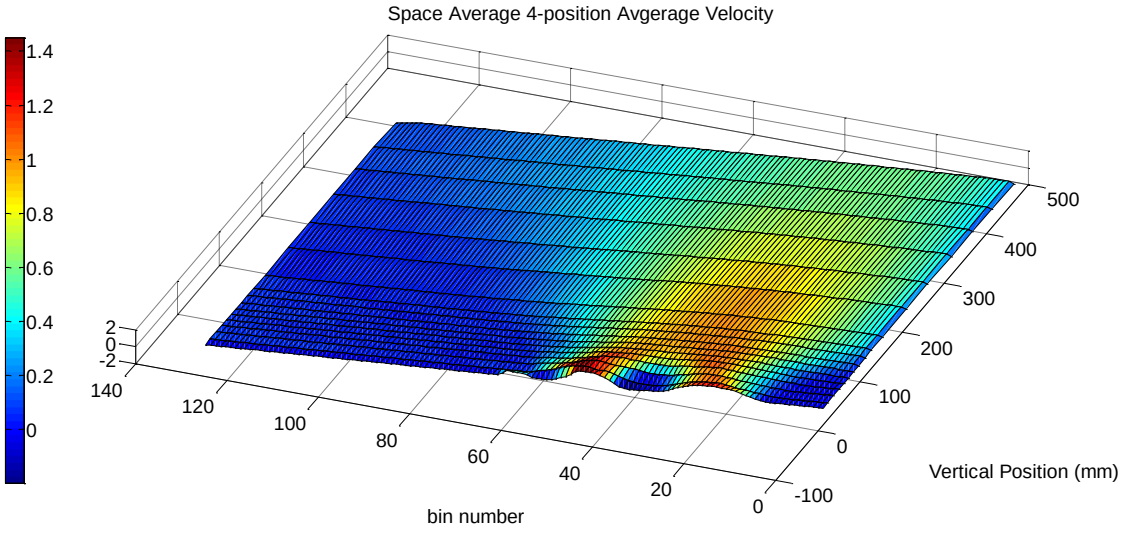

Figure 102. Space Average 4-position Average Velocity.

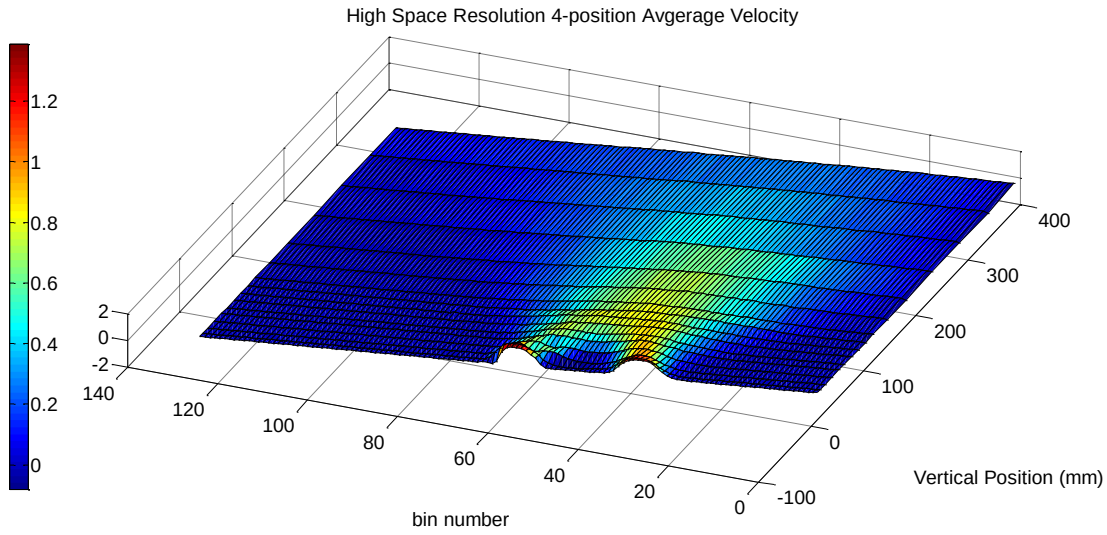

Figure 103. High Space Resolution 4-position Average Velocity.

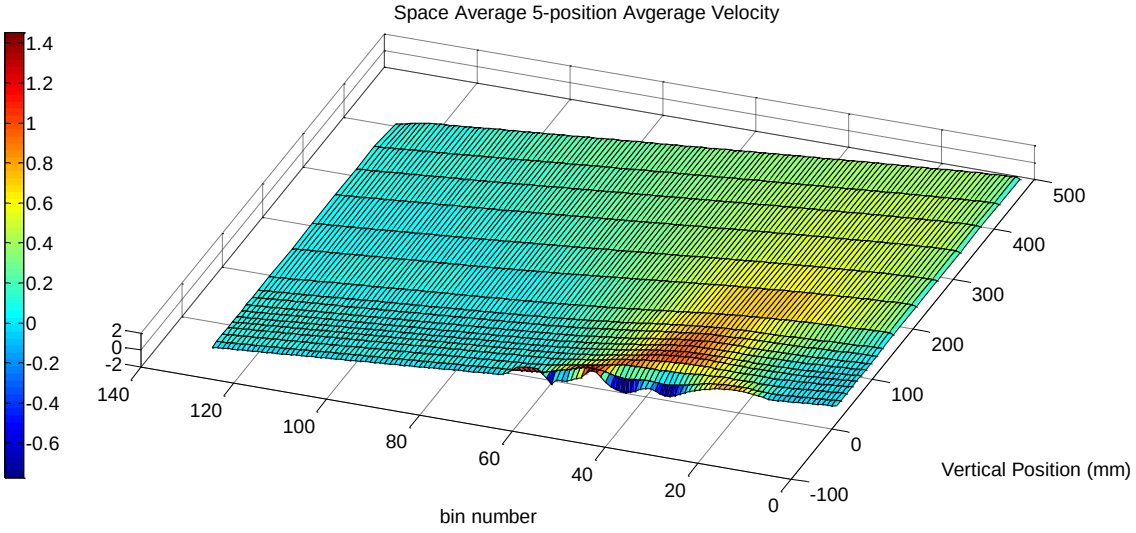

Figure 104. Space Average 5-position Average Velocity.

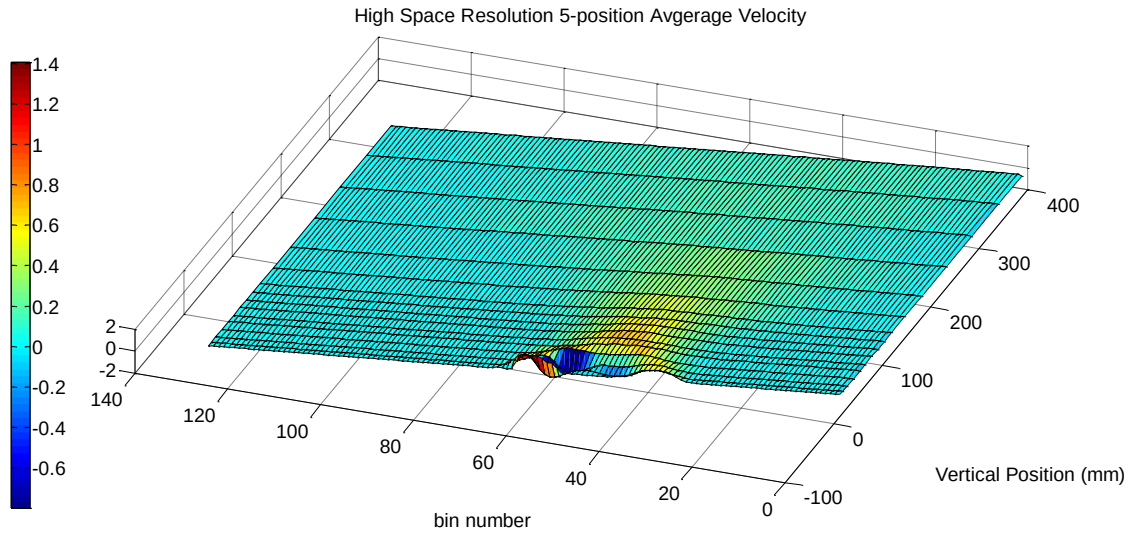

Figure 105. High Space Resolution 5-position Average Velocity.

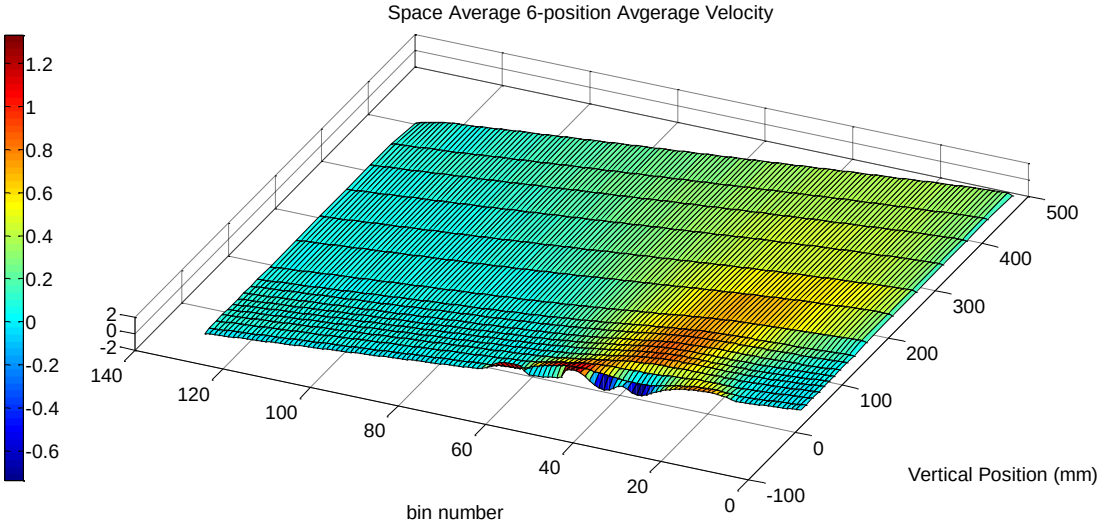

Figure 106. Space Average 6-position Average Velocity.

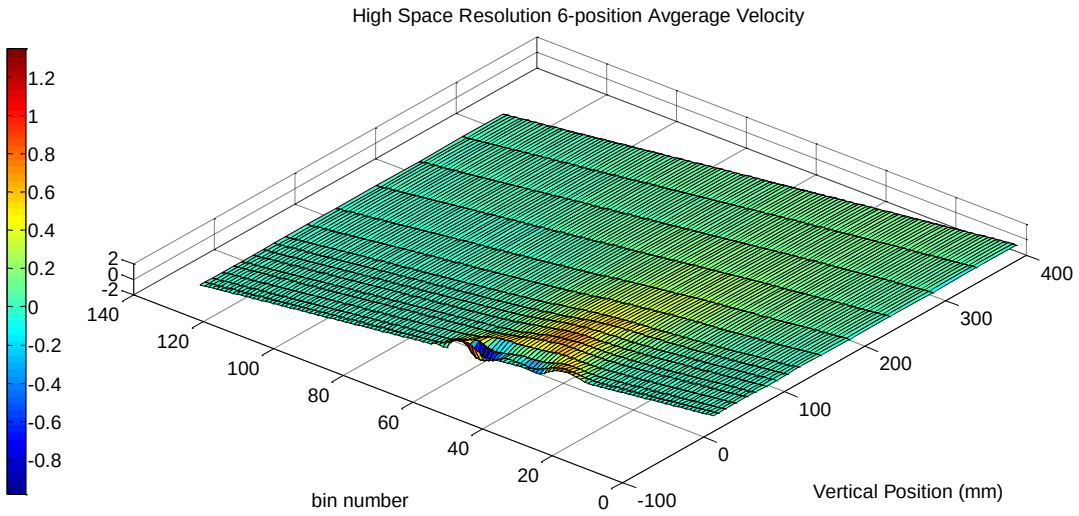

Figure 107. High Space Resolution 6-position Average Velocity.

APPENDIX B: UVP DATA TRANSLATION TO MATLAB (CODE)

```
%%%Code written by Lee Tschaepe 11/14/2011
clc; clear all; close all
%%%%%%%%%%%%%%%%%Import the data%%%%%%%%%%
Dire = dir;
File = cell(size(Dire));
keep = false(size(File));

for i = 1:length(Dire)
   if ~Dire(i).isdir
    tail = Dire(i).name(end-3:end);
    if strcmpi('.TXT',tail)
        File{i} = Dire(i).name;
        keep(i) = true;
    end
   end
end

File = File(keep);
count = 0;

cnt1 = 0;
cnt2 = 0;
cnt3 = 0;
for i=1:length(File)
    %High Reptition (32), High Cycles (4)
    if (File{i} (1)) == 'h'
        cnt1 = cnt1+1;
        Jet1{cnt1,1} = File{i};
    %Medium Reptition (96), High Cycles (16)
    elseif (File{i} (1)) == 'm'
        cnt2 = cnt2+1;
        Jet2{cnt2,1} = File{i};
    %Low Reptition (200), High Cycles (32)
    elseif (File{i} (1)) == 'l'
        cnt3 = cnt3+1;
        Jet3{cnt3,1} = File{i};
    end
end
%High Resolution
for i = 1:length(Jet1)
    XX = Jet1{i}(5:6);
    if isempty(strfind(num2str(0:9),XX(2)))
        XX = XX(1);
    end
    num1(i,1)= str2num(XX);
end
Val = num1;
[S Si] = sort(Val);
Jet1_sorted = Jet1(Si);
%Medium Resolution
for i = 1:length(Jet2)
    XX = Jet2{i}(5:6);
    if isempty(strfind(num2str(0:9),XX(2)))
        XX = XX(1);
```

```
    end
    num2(i,1)= str2num(XX);
end
Val = num2;
[S Si] = sort(Val);
Jet2_sorted = Jet2(Si);
%Low Resolution
for i = 1:length(Jet3)
    XX = Jet3{i}(5:6);
    if isempty(strfind(num2str(0:9),XX(2)))
        XX = XX(1);
    end
    num2(i,1)= str2num(XX);
end
Val = num2;
[S Si] = sort(Val);
Jet3_sorted = Jet3(Si);

for j = 1:length(Jet1_sorted)
    [A1] = dlmread(Jet1_sorted{j},',',19,1);
    for i=1:128
        y1(i,j) = ((-1/1000)*mean(A1(i,:)))';
        z1(i,j) = ((1/1000)*std(A1(i,:)))';
    end
    x=[1:128];
end

for j = 1:length(Jet2_sorted)
    [A2] = dlmread(Jet2_sorted{j},',',19,1);
    for i=1:128
        y2(i,j) = ((-1/1000)*mean(A2(i,:)))';
        z2(i,j) = ((1/1000)*std(A2(i,:)))';
    end
    x=[1:128];
end

for j = 1:length(Jet3_sorted)
    [A3] = dlmread(Jet3_sorted{j},',',19,1);
    for i=1:128
        y3(i,j) = ((-1/1000)*mean(A3(i,:)))';
        z3(i,j) = ((1/1000)*std(A3(i,:)))';
    end
    x=[1:128];
end
%Orientation of the data to represent the physical reality of the
%experiment.
start=5.0;
fin=99.1;
wind=0.74;
theta=70;
totalwin=wind*128;
space=128-1;
dif=fin-start;
gaps=(dif-totalwin)/(space);
```

```
%%%%The change of the first number away from zero corresponds to the
channels discarded.
x1=[0:127];
%%%%Vertpos1 corresponds to readings for cjet files.
vertpos1=[10.8600000000000,14.8900000000000,20.1300000000000,25.1600000
000000,36.2500000000000,47.7200000000000,58.8900000000000,67.4000000000
000,77.7700000000000,90.8500000000000,107.400000000000,120.630000000000
,137.080000000000,149.430000000000,164.430000000000,190.430000000000,22
3.430000000000,263.430000000000,298.430000000000,349.430000000000,395.4
30000000000,445.430000000000,491.430000000000,545.430000000000,600.4300
00000000];
y=x1';
% for j=1:length(vertpos1)
%         for i=1:length(x1)
%             %%%%This is the vertical position of each measurement.
%             x21(i,j)=vertpos1(j)-x1(i)*(wind+gaps)*sin(theta);
%             %%%%This is the horizontal position of each measurement
%             %y(i,1)=x1(i)*(wind+gaps)*cos(theta)+start*cos(theta);
%         end
% end
% figure(1)
% surf(x21,y,y1)
% title('Average Velocity High Resolution');
% xlabel('Vertical Position (mm)');
% ylabel('bin number');
% colorbar;
% figure(2)
% surf(x21,y,y2)
% title('Average Velocity Medium Resolution');
% xlabel('Vertical Position (mm)');
% ylabel('bin number');
% colorbar;
% figure(3)
% surf(x21,y,y3)
% title('Average Velocity low Resolution');
% xlabel('Vertical Position (mm)');
% ylabel('bin number');
% colorbar;
% figure(4)
% surf(x21,y,z1)
% title('Standard Deviation High Resolution');
% xlabel('Vertical Position (mm)');
% ylabel('bin number');
% colorbar;
% figure(5)
% surf(x21,y,z2)
% title('Standard Deviation Medium Resolution');
% xlabel('Vertical Position (mm)');
% ylabel('bin number');
% colorbar;
% figure(6)
% surf(x21,y,z3)
% title('Standard Deviation Low Resolution');
% xlabel('Vertical Position (mm)');
% ylabel('bin number');
```

```
% colorbar;
for i=1:9
    close all;
    plot(y1(:,i),'r','LineWidth',2)
    hold on
    plot(y2(:,i),'go','LineWidth',2)
    plot(y3(:,i),'k*','LineWidth',2)
    legend('High Resolution', 'Medium Resolution', 'Low Resolution');
    xlabel('bin number');
    ylabel('Average Velocity m/s');
    pause
end
```

VITA

Lee Paul Tschaepe was born in Gallatin, Tennessee. He attended the Georgia Institute of Technology and obtained a B.S.E. in Mechanical Engineering and a B.S.E. in Nuclear Engineering in 2007. Following the completion of his work at the Georgia Institute of Technology he enrolled in the Nuclear Engineering program at the University of Tennessee and obtained a Masters in Nuclear Engineering in 2009.